ISSN 2732–0189 (Online)
ISSN 1586–2070 (Print)

JOURNAL OF COMPUTATIONAL AND APPLIED MECHANICS

An Open Access International Journal

Published by the University of Miskolc

VOLUME 16, NUMBER 2 (2021)

MISKOLC UNIVERSITY PRESS

ISSN 2732–0189 (Online)
ISSN 1586–2070 (Print)

JOURNAL OF COMPUTATIONAL AND APPLIED MECHANICS

An Open Access International Journal

Published by the University of Miskolc

VOLUME 16 NUMBER 2 (2021)

MISKOLC UNIVERSITY PRESS

Journal of Computational and Applied Mechanics, Vol. 16, No. 2, (2021), pp. 73–74
DOI: 10.32973/jcam.2021.010

PREFACE

This issue of the Journal of Computational and Applied Mechanics includes several articles dedicated to Prof. Tibor Czibere on the occasion of his 90th birthday. Among contributions from his former colleagues and students are papers that carry on the work of Prof. Czibere.

Tibor Czibere was born in 1930 in Tapolca, a town near Lake Balaton. After graduating from secondary school in Keszthely he was admitted in 1949 to the newly established Faculty of Mechanical Engineering of the Technical University for Heavy Industry in Miskolc (now the University of Miskolc), earning his MSc in 1953 with the first class of graduates. Naturally, he passed with flying colors and was encouraged to follow an academic career. His first position was assistant lecturer at the Department of Mathematics at the Technical University for Heavy Industry, under the guidance of the Hungarian mathematician Prof. Samu Borbély. In 1956 he became a research engineer at the Ganz-MÁVAG Locomotive and Railway Carriage Manufacturers. His first task was the investigation of flow in the bladed space of torque converters, and he developed a method based on the method of hydrodynamic singularities for the analysis and design of flow in turbomachines. Even after returning to the university in 1963, Prof. Czibere continued to do research there on a part-time basis until 1988.

An early area of his research was nonlinear heat conduction problems, the field in which he wrote and defended his university doctor's thesis (1961). In 1960 he delivered a well-received lecture at the Tenth International Conference in Applied Mechanics in Stresa, Italy, on his method for the design of straight and radial cascades of airfoils, attracting the attention of the world-famous scientist of Hungarian origin, Theodore von Kármán. In 1962, he was awarded the Kossuth Prize in acknowledgment of his scientific contributions. In 1963 he defended his thesis entitled "A design method for straight cascade of highly cambered airfoils" for the PhD degree conferred by the Hungarian Academy of Sciences and four years later he defended his thesis for DSc (the highest academic degree, conferred also by the Hungarian Academy of Sciences) entitled "Solution of the two main problems of the hydrodynamic cascade theory by theory of potentials". He was appointed full professor in 1968, at the early age of 38. In 1976 Prof. Czibere became a corresponding member of the Hungarian Academy of Sciences, and in 1985 an ordinary member.

Apart from three months as a guest lecturer at the Technical University of Berlin-Charlottenburg (1963), Prof. Czibere gave several lecture series about his research at different institutions, including Turboinstitut in Ljubljana (1978, 1984); Technical University of Brno (1990); Technical University of Braunschweig (1994); and several times at the Otto von Guericke Technical University in Magdeburg. The Technical University of Brno awarded him its gold medal for the fruitful scientific cooperation between the two universities.

Prof. Czibere also held leadership roles in the faculty and the university. As Head of Department from 1963 to 1988 (Department of Machine Operation, later Department of Fluid and Heat Engineering) he modified the research and educational profiles of the department and encouraged research topics directly connected with industrial problems. He served as Dean of the Faculty of Mechanical Engineering from 1968 to 1974, a period when the structure of education underwent substantial changes, and Prof. Czibere contributed significantly to the introduction of the modular educational system. In recognition of his scientific contributions and his leadership qualities he was elected Rector of the University in 1978. As Rector he spearheaded the shift from a purely technical university to a multi-disciplinary institution, introducing the training of lawyers and economists. He supported the establishment of the Faculty of Law in 1981 and laid the groundwork for the later establishment of faculties of economics and humanities. During his eight years in this post, he worked closely with the leaders of the city of Miskolc, and this contribution was recognized by the prize 'Pro Urbe' (For the City).

In 1988, Prof. Czibere was asked to contribute his expertise in educational administration as the Minister of Culture and Education of Hungary, in the difficult period of transition from the socialist system. Ultimately, his concepts and those of the national leadership differed, and the following year he returned to teaching and research.

Prof. Czibere has always put a great deal of effort into educational endeavors. He developed the curriculum of courses such as Fluid Mechanics, Turbomachines, Continuum Mechanics of Fluids, and Heat Transfer. He wrote textbooks for most of the subjects he taught. An excellent lecturer, he prepared carefully and structured his lectures in a very logical way. Using mathematical means, he derives equations or formulae describing flow phenomena in a concise manner.

Prof. Czibere played an active role in establishing the PhD training at the university and supervised a total of twenty PhD dissertations; in addition, he was the supervisor of four scholars who have defended their DSc dissertations. Of course, the number of engineers and researchers directly and indirectly influenced by Prof. Czibere is much larger.

Upon reaching the age of 70, although Prof. Czibere retired, he continued his contributions as an Emeritus Professor. He taught subjects in the doctoral school; he examined students up until 2018 (aged 88!). He remains active also in research, working on developing a three-dimensional stochastic model of turbulence. Prof. Czibere has always been supported in his activities by his wife Gabriella. They have two children, both of whom went into technical fields. He is a proud grandfather and great-grandfather.

Awards recognizing Prof. Czibere's many and varied contributions are the Albert Szentgyörgyi Prize, 1996, for his influential scientific contributions; honorary citizenship of Miskolc, 2000; 'Doctor Honoris causa' of the University of Miskolc in 2000; and the national Széchenyi Award in 2006.

On behalf of his friends, colleagues and his former students, the editors are pleased to dedicate this issue to Prof. Czibere in honor of his 90th birthday.

Miskolc, November 23, 2021 László Baranyi and Balázs Tóth

Journal of Computational and Applied Mechanics, Vol. 16, No. 2, (2021), pp. 75–86
DOI: 10.32973/jcam.2021.005

METHODOLOGY OF MODEL DEVELOPMENT IN THE APPLIED SCIENCES

Barna Szabó
Washington University
One Brookings Drive, St. Louis, Missouri, 63130 USA
szabo@email.wustl.edu

Ivo Babuška
Oden Institute, The University of Texas at Austin,
201 E. 24th Street, Austin, Texas 78712 USA
babuska@ices.utexas.edu

[Received: April 19, 2021; Accepted: June 14, 2021]

Abstract. The formulation and validation of mathematical models in the applied sciences are largely consistent with the methodology of scientific research programmes (MSRP), however an essential modification is necessary: The domain of calibration has to be defined. The ranking and systematic improvement of mathematical models based on objective criteria are described and illustrated by an example. The methodology outlined in this paper provides a framework for the evolutionary development of a large class of mathematical models.

Mathematical Subject Classification: 03C30, 62M86, 65N75, 65Z05
Keywords: Formulation, validation, calibration, uncertainty quantification, simulation.

1. Introduction

The formulation and validation of mathematical models is fundamental to predictive computational science [1]. These activities fit into the framework of the Methodology of Scientific Research Programmes (MSRP) as outlined by Imre Lakatos [2], subject to an essential modification; the definition of the domain of calibration, which is addressed in this paper.

We view a mathematical model as a transformation of one set of data (the input $\mathbf{D}$) into another set (the quantities of interest $\mathbf{F}$). The transformation is based on some idea of physical reality $\mathbf{I}$ cast in mathematical form. This is indicated in short hand by the expression

$$(\mathbf{D},\mathbf{I}) \underset{\mathbf{p}}{\longrightarrow} \mathbf{F}, \qquad (\mathbf{D},\mathbf{p}) \in \mathbb{C} \tag{1.1}$$

where the right arrow represents all operations needed to transform $\mathbf{D}$ into $\mathbf{F}$. These operations involve a set of parameters $\mathbf{p}$ that represent physical properties and their statistical distributions. These parameters are determined by calibration which is discussed in Section 2.2. The restrictions imposed on $\mathbf{D}$ by the assumptions incorporated into the model, and the intervals on which the parameters were calibrated, define the domain of calibration $\mathbb{C}$. We shall assume that $\mathbf{F}$ is a smooth function of $\mathbf{D}$ and $\mathbf{p}$, that is, a small change in $(\mathbf{D},\mathbf{p})$ will result in a small change in $\mathbf{F}$. Consequently a calibrated model is a validated within the domain of calibration.

The domain of calibration is a fundamentally important attribute of a mathematical model: As long as $\mathbf{F}$ is a smooth function of $(\mathbf{D}, \mathbf{p})$, a condition usually satisfied in practice, just about any model, even pseudoscientific models, can be validated on a sufficiently small domain of calibration [3]. In chaotic systems, such as turbulent flow, depending on its definition, $\mathbf{F}$ may not be a smooth function of $(\mathbf{D}, \mathbf{p})$.

To highlight the importance of the concept of domain of calibration, consider Newtonian mechanics, arguably the greatest scientific achievement in history. For about 200 years, it was generally believed that Newton's three laws of motion and the law of universal gravitation were laws of nature. This was supported by the evidence that predictions based on Newton's laws were consistently confirmed by observations with almost perfect accuracy. However those observations involved only bodies that move at velocities much smaller than the speed of light. Therefore the domain of calibration of Newtonian mechanics was limited to velocities much smaller than the speed of light. The theory of relativity did not refute Newtonian mechanics but it did define its domain of calibration and downgraded its status from "law of nature" to that of a phenomenological model. Mathematical models that incorporate Newton's laws continue to be useful, as any civil engineer will testify. Newtonian mechanics has an amazingly large domain of calibration.

Arguably, all physical theories are phenomenological models. This was articulated by Hawking in [4]: *"I take the positivist viewpoint that a physical theory is just a mathematical model and that it is meaningless to ask whether it corresponds to reality. All that one can ask is that its predictions should be in agreement with observations."*

To this statement we append the explanatory note that we can reasonably ask the predictions to be in agreement with observation within the domain of calibration of the model only.

Popper expressed the same view in these words [5]: *"The empirical basis of objective science has nothing absolute about it. Science does not rest on solid bedrock. The whole towering structure, the often fantastic and audacious construction of scientific theories, is built over a swamp. Its foundations are pillars driven from above into the swamp - not down to any natural 'given', ground, but driven just as deeply as is necessary to support the structure. The reason why we stop driving the pillars deeper into the ground is not that we have reached solid rock. No, our decision is based on the hope that the pillars will support the structure."*

These observations are in line with the philosophical notion of model-dependent realism [6]: Mathematical models represent precisely formulated ideas of certain aspects of reality. They must not be confused with reality. Also, since more than one model can be formulated to simulate any aspect of reality, it is necessary to have metrics by which the relative merit of competing models is measured.

In this paper we illustrate the fundamentals of model development in the applied sciences through an example, the details of which have been documented in the technical literature in recent years.

2. The methodology of model development

We illustrate the methodology of model development with reference to a specific project, the details of which have been documented in the technical literature in references [7], [8], [9], [10] and [11]. The goal of that project was to develop and validate a mathematical model for estimating the probability of failure in critical mechanical and structural components subjected to cyclic loading in the high cycle regime. This problem arises in the management of the maintenance of high-value assets, such as helicopters: There is a strong incentive to minimize the number of unscheduled maintenance operations because it is much more economical to perform maintenance at regularly scheduled times than at the times when the presence of a flaw is detected.

In a scientific research programme, as the term was defined by Lakatos [2], there are generally accepted "hard core" theorems and assumptions that are not open to investigation. In addition, there are auxiliary hypotheses that may be altered or abandoned to conform with the available empirical evidence.

In the example discussed in this paper, our hard core assumptions will be the set of assumptions on which the linear theory of elasticity is based, augmented by the assumption that localized nonlinear effects can be correlated with the elastic stress field. The limitations imposed by the hard core assumptions are taken into consideration in the definition of the domain of calibration.

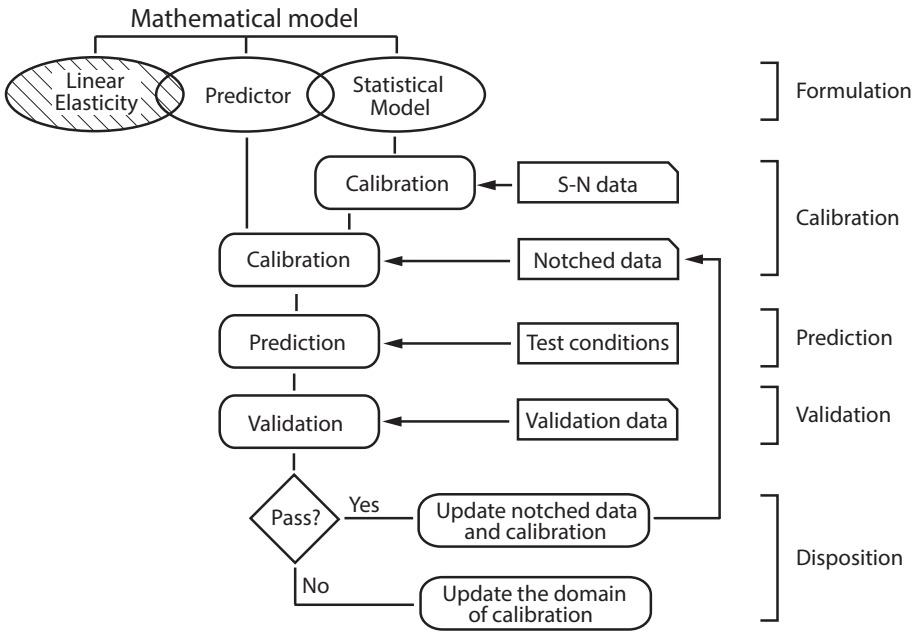

Figure 1. Schematic view of the model development process.

The auxiliary hypotheses are concerned with the prediction of failure events in metallic objects subjected to cyclic loading and the statistical dispersion associated with mechanical fatigue. The auxiliary hypotheses have their own domains of calibration which are generally much smaller than the domain of calibration of the hard core hypotheses.

Lakatos called the replacement or modification of auxiliary hypotheses "problem shifts". A research programme is said to be progressive if each problem shift improves the predictive performance of the model. In our case, which is typical of research programmes in the applied sciences, the research programme can only be progressive, that is, the predictive performance of a model is guaranteed to increase monotonically. This is because ideas that do not improve predictive performance are filtered out in the course of model development. This establishes the conditions for an evolutionary process in model development.

A schematic view of the model development process is shown in Figure 1. On the left side of the figure the steps taken in the particular model development project referenced in this paper are shown. The universal categories, common to all model development projects, are indicated on the right hand side.

2.1. **The mathematical model.** The mathematical model has three parts: The first part, in the terminology of MSRP, incorporates the hard core assumptions: The second and third parts incorporate the auxiliary hypotheses.

2.1.1. *The hard core assumptions.* It is assumed that damage initiation, a highly nonlinear and irreversible process, is confined to small subdomains that are surrounded by an elastic stress field. The nonlinear process is controlled by the stress field that satisfies the assumptions of the theory of linear elasticity.

The hard core assumptions are not subject to investigation. Rather, the domain of calibration is defined so as to ensure that the model is operated within the limitations imposed by these assumptions. In the present instance the domain of calibration is defined so that the size of the inelastic zone is limited.

2.1.2. *Auxiliary hypothesis 1: The predictor.* The predictor is a functional defined on the elastic stress field. Its role is to generalize the S-N data[1] to triaxial stress fields. It characterizes the conditions that drive the formation of cracks in the neighborhood of stress raisers. The definition of a predictor is subject to the restriction that it has to be a finite number which is independent of the choice of the coordinate system. This suggests that the predictor should be defined in terms of the stress invariants. Any number of predictors can be defined. We will consider the predictor defined in reference [7]. This predictor, denoted by G_α, depends on three parameters that have to be determined by calibration. Its definition is given in Appendix A.

[1]The name refers to the relationship between the stress S and the number of load cycles N at which failure occurred under constant-cycle loading at various mean stress levels.

2.1.3. *Auxiliary hypothesis 2: The statistical model.* The statistical model characterizes the random nature of failure caused my mechanical fatigue. Statistical models are calibrated on the basis of the available S-N data. Many plausible statistical models can be defined [12]. The statistical model used in the investigation discussed here has five parameters and belongs in the class of random fatigue limit models proposed by Pascual and Meeker [13]. Its definition is given in Appendix B.

2.2. **Calibration.** It is assumed that the material is elastic and isotropic, therefore its stress-strain relationship is characterized by two experimentally determined constants. These constants, the modulus of elasticity and Poisson's ratio, are random variables, however their dispersion is small in comparison with the dispersion of crack formation events therefore their statistical variation is neglected.

The predictor generalizes the S-N data, collected for notch-free specimens tested either under constant or mildly varying uniaxial stress conditions, to notched specimens where the stress gradient can be very large and the stress conditions are triaxial at the notch roots. A key assumption is that crack formation is completely determined by the surrounding elastic stress field, notwithstanding the fact it is a highly nonlinear process. It is reasonable to expect that this assumption will hold when the size of the plastic zone is sufficiently small in comparison with some measure of volume associated with the predictor. Therefore it is necessary to give a precise definition for the meaning of "sufficiently small" which then limits the domain of calibration of the predictor. This is one of the tasks of model development. Further discussion and details are available in [10].

The statistical model employed in the model development project represented by the flowchart in Figure 1 is a random fatigue limit model that has five parameters defined in Appendix B. Those parameters are determined by maximizing the likelihood function on the S-N data [12], [7].

As indicated in Figure 1, the statistical model is calibrated first and then the predictor is calibrated on the basis of fatigue data obtained for notched specimens. Once the calibration of the predictor is complete, it is possible to compare alternative predictors and evaluate their relative performance with reference to the calibration data. This was documented in [9]. The conclusion was that the predictor G_α performs substantially better than previously proposed predictors. This is evidenced by the facts that its domain of calibration is larger and the value of the likelihood function is greater.

2.2.1. *The domain of calibration.* The domain of calibration establishes limits on the admissible data $\mathbf{D}$ and defines intervals for the parameters $\mathbf{p}$. In the example discussed discussed here, $\mathbf{D}$ must be consistent with the assumptions of linear elasticity, that is, the strains are infinitesimal, the relationship between the stress and strain is linear, with the exception of small subdomains in the vicinity of stress raisers, the size of which is clearly defined. Examples are available in references [10], [11]. If the model was calibrated under special conditions (for example, under uniaxial loading only) then the domain of calibration imposes commensurate limitations on $\mathbf{D}$.

Restrictions on the parameters **p** are imposed by the availability of data used for calibration. For example, the five-parameter statistical model defined in reference [7], was calibrated on the basis of S-N data in the range of 10^4 to 10^7 cycles. This defines the domain of calibration for the statistical model. Similarly, the calibration of the predictor is limited by the interval of highly stressed volume for which calibration records for notched specimens are available [9].

An often overlooked limit on the statistical model is that calibration is based on events that have high probabilities of occurrence. Therefore prediction of events that have low probabilities of occurrence involves extrapolation beyond the domain of calibration. An important corollary is that the most important quantity of interest in engineering design, the factor of safety, cannot be validated. Therefore subjective decisions cannot be avoided in establishing factors of safety [8].

2.3. **Prediction.** Having formulated and calibrated a mathematical model, its predictive performance is tested against new data which are not in the domain of calibration. Predictions are made on the basis of information on the conditions under which new data will be observed. Ideally, the predictions should be made before the new data became available.

The value of new data outside of the domain of calibration is that the predictive performance of the model can be tested and the domain of the calibration set can be enlarged. The value of new data within the domain of calibration is that the dataset on which calibration was based is enriched and therefore confidence in the calibrated parameters is increased.

A typical validation statement is formulated as follows: The probability is (say, 90%) that the observation x will be in the interval $(x_L < x < x_U)$. In the case of the mechanical fatigue experiments considered here, the prediction is that, given a notched test article and the mean and amplitude of the applied cyclic load, the probability is 90% that the number of cycles N_f at which failure will occur will fall between the limits N_L and N_U. Another way of saying this is that in 9 out of 10 experiments N_f will lie in the interval (N_L, N_U) where N_L (resp. N_U) correspond to the 5% (resp. 95%) survival probability, given the loading conditions.

The probability of n successes in m trials is given by the binomial distribution:

$$Pr(m, n \,|\, \theta) = \frac{m!}{n!(m-n)!}\theta^n(1-\theta)^{m-n} \tag{2.1}$$

where θ is the ratio n/m as $m \to \infty$. In our example $\theta = 0.90$.

Remark 1. The selection of the 90% probability threshold was based on the following consideration: Validation is typically based on events that have high probability of occurrence. Calibration data are generally scarce for survival probabilities of less than 5% and greater than 95% and hence those probabilities fall outside of the domain of calibration of the statistical model.

2.4. **Validation.** The primary purpose of validation is to seek evidence that would justify rejecting a model. The secondary purpose is to develop information on the basis of which he domain of calibration is defined. The prediction considered here is

that out of 10 experiments there will be 9 failures in the predicted intervals, more precisely it was predicted that $\theta = 0.90$ in equation (2.1).

Suppose that 12 experiments were performed and 9 outcomes fell in the predicted interval. Would that justify rejecting the model? - Assuming that the model is correct ($\theta = 0.90$), according to equation (2.1) the probability of observing 9 successes in 12 trials would be 8.5%. In testing statistical hypotheses a null hypothesis is usually not rejected unless the probability observing an outcome, given that the hypothesis is true, is less than 5%. For example, if only 7 outcomes fell in the predicted interval out of 12 experiments then the probability of outcome, assuming that $\theta = 0.90$, would be less than 0.4% and we would not have confidence in the model. However it is difficult to justify any fixed value of probability below which a model would be rejected.

Models are typically rejected not because their validity was refuted by observation, but because a better model was found. By objectively ranking competing models, predictive performance is progressively improved over time. Model development projects are open-ended: No one can claim to have the final word. New ideas and new observations present opportunities for continued improvement. The management of the process of model development in industrial and research organizations is guided by the principles of simulation governance [14].

2.5. **Disposition.** If no reasons were found to reject a model then the validation data are merged with the calibration data and the calibrated parameters, as well as the domain of calibration, are updated.

Using the updated calibration records, the likelihood function is evaluated for the entire set of data. The value of the log likelihood function (LL) is a metric suitable for measuring the relative merit of alternative models. For a given set of data, the highest ranking model has the highest LL value and/or the largest domain of calibration.

New data within the domain of calibration presents an opportunity to update the calibrations. Predictions outside of the domain of calibration are either validated or fail to be validated. If validated then the calibration records are updated and the domain of calibration is suitably modified. If fail to be validated then a point outside of the domain of calibration is obtained which provides information about the size of the domain. A mathematical model is a validated model within its domain of calibration.

Remark 2. Model development projects are open-ended. The selection of a model from among a set of candidate models depends on the available data. Both the set of candidate models and the available data change over time, therefore any conclusion as to which model to use is likely to change over time. The exercise of command and control over numerical simulation, which include the formulation, ranking and updating of mathematical models and management of the relevant data is called simulation governance [14].

3. Ranking

Assume that two models M_1 and M_2 have the same number of statistical parameters and both passed validation tests with the same number of successes. We have to

decide which model is better and why. The answer is provided by the posterior ratio defined by

$$\varrho \stackrel{\text{def}}{=} \frac{Pr(M_1 \,|\, \mathbb{D})}{Pr(M_2 \,|\, \mathbb{D})} = \frac{Pr(\mathbb{D} \,|\, M_1) Pr(M_1)}{Pr(\mathbb{D} \,|\, M_2) Pr(M_2)} \tag{3.1}$$

where $\mathbb{D}$ represents the entire set of available data, that is, the data available for calibration and validation. The probabilities are obtained from the statistical model.

Usually it is assumed that $Pr(M_1) \approx Pr(M_2)$ in which case ϱ is approximately equal to the ratio of likelihoods, called the Bayes factor, which can be easily computed. If ϱ is much greater than one then we prefer model M_1, if it is much smaller than one then we prefer model M_2. If this ratio is between 3 and 1/3 then the two models are in a virtual tie. For additional discussion and examples we refer to [3].

In addition to considering the posterior ratio, we have to consider the size of the domain of calibration. How much weight should be assigned to the size of the domain of calibration depends on the scope of the intended application of the model. In other words, we choose the model that fits the available data best. In the philosophical literature the term "abduction" (inference to the best explanation) is used to refer to this approach.

Remark 3. If models M_1 and M_2 do not have the same number of statistical parameters then equation (3.1) has to be modified by a factor, called the Occam factor, which penalizes the model that has the larger number of parameters. See (for example) [15].

4. Philosophical positions

The question of how progress occurs in science is one of the central themes in the philosophy of science. The approach presented here is consistent with the philosophical idea called model-dependent realism [6]. In this view, aspects of reality are seen through mathematical models. Therefore progress in science means progress in formulating, calibrating, validating and updating mathematical models. It is essential therefore to have objective measures for ranking mathematical models according to their predictive performance, taking into account their domains of calibration.

Particularly relevant to our discussion was Lakatos' methodology of scientific research programmes. An opposing point of view, first articulated by Paul Feyerabend, is that it is not possible to establish meaningful methodological rules that govern scientific progress. In Feyerabend's view, "epistemological anarchy" exists. In his words; "anything goes" [16]. These are colourful ways of saying that complete creative freedom exists.

The conflict between these points of view is resolved if we distinguish between the methodologies in the applied and foundational sciences. Model development in the applied sciences fits into the framework of MSRP well because the focus is on the auxiliary hypotheses. The hard core assumptions are based on ideas, theorems and methods previously established in the foundational sciences. It is doubtful that a set of rules can be devised that will encompass the diverse lines of investigation at the forefront of research in physics where the focus is on the hard core itself.

Reference [17] provides a comprehensive overview of the state of model development in physics. In the applied sciences Lakatos' views, whereas at the forefront of physics Feyerabend's epistemological anarchy seem to provide the best description of how scientific models evolve.

5. Summary and conclusions

Mathematical models are transformations of one set of data into another, as indicated by equation (1.1). The transformation operators are based on clearly defined assumptions and depend on physical properties that have to be determined by calibration. The domain of calibration is defined by the intervals for which measurements of the physical properties are available, and the limitations imposed by the assumptions incorporated in the operators.

Consideration of the size of the domain of calibration is essential. Without such consideration no model could be rejected because just about any model can be calibrated on a sufficiently small domain.

Model development is always open-ended. This is because new data may become available and new models may be proposed at any time that will justify replacing or updating the currently adopted model.

The methodology outlined in this paper establishes a framework for the evolutionary development of mathematical models.

Acknowledgement. The authors thank Drs. Ricardo Actis and Börje Andersson for their helpful comments on the manuscript.

References

1. J. T. Oden, Babuška I., and D. Faghihi. "Predictive Computational Science: Computer Predictions in the Presence of Uncertainty." *Encyclopedia of Computational Mechanics*. Ed. by René de Borst Erwin Stein and Thomas J. R. Hughes. Vol. 1: Fundamentals. John Wiley & Sons Ltd., 2017. DOI: 10.1002/9781119176817.ecm2101.
2. I. Lakatos. "Falsification and the methodology of scientific research programmes." *Can theories be refuted?* Ed. by Sandra G. Harding. Dordrecht: Springer Netherlands, 1976, pp. 205–259. DOI: 10.1007/978-94-010-1863-0_14.
3. B. Szabó and Babuška I. *Finite Element Analysis: Method, Verification and Validation.* John Wiley & Sons Ltd., 2021.
4. S. Hawking and R. Penrose. *The Nature of Space and Time*. Princeton University Press, Princeton, New Jersey, 1998.
5. K. R. Popper. *The Two Fundamental Problems of the Theory of Knowledge*. Routledge, 2014.
6. S. Hawking and L. Mlodinow. *The Grand Design*. Bantam Books, New York, 2010.
7. B. Szabó, R. Actis, and D. Rusk. "Predictors of fatigue damage accumulation in the neighborhood of small notches." *International Journal of Fatigue,* **92**(1), (2016), pp. 52–60. DOI: 10.1016/j.ijfatigue.2016.06.017.

8. B. Szabó, R. Actis, and D. Rusk. "On the formulation and application of design rules." *Computers and Mathematics with Applications,* **74**(9), (2017), pp. 2191–2202. DOI: 10.1016/j.camwa.2017.06.040.
9. B. Szabó, R. Actis, and D. Rusk. "Validation of notch sensitivity factors." *Journal of Verification, Validation and Uncertainty Quantification,* **4**(1), (2019). 011004. DOI: 10.1115/1.4044236.
10. B. Szabó, R. Actis, and D. Rusk. "Validation of a predictor of fatigue failure in the high cycle range." *Computers and Mathematics with Applications,* **80**, (2020), pp. 2451–2461. DOI: 10.1016/j.camwa.2020.07.026.
11. B. Szabó, R. Actis, and D. Rusk. "Validation test of a predictor of fatigue failure under biaxial out-of-phase loading conditions." *Computer Methods in Applied Mechanics and Engineering,* **378**, (2021). 113718. DOI: 10.1016/j.cma.2021.113718.
12. I. Babuška, Z. Sawlan, M. Scavino, B. Szabó, and R. Tempone. "Bayesian inference and model comparison for metallic fatigue data." *Computer Methods in Applied Mechanics and Engineering,* **304**(1), (2016), pp. 171–196. DOI: 10.1016/j.cma.2016.02.013.
13. F. G. Pascual and W. Q. Meeker. "Estimating fatigue curves with the random fatigue-limit model." *Technometrics,* **41**(4), (1999), pp. 277–289. DOI: 10.2307/1271342.
14. B. Szabó and R. Actis. "Simulation governance: Technical requirements for mechanical design." *Computer Methods in Applied Mechanics and Engineering,* **249–252**(1), (2012), pp. 158–168. DOI: 10.1016/j.cma.2012.02.008.
15. D. S. Sivia. *Data Analysis. A Bayesian Tutorial.* 2nd ed. Oxford: Oxford University Press, 2006.
16. I. Lakatos and P. Feyerabend. *For and against Method: Including Lakatos's Lectures on Scientific Method and the Lakatos-Feyerabend Correspondence.* University of Chicago Press, 2016.
17. R. Penrose. *Fashion, Faith and Fantasy in the New Physics of the Universe.* Princeton: Princeton University Press, 1999.

Appendix A. The predictor

The predictor defined in reference [7] was used in the present investigation. This predictor, denoted by G_α, is based on the assumption that the onset of fatigue failure can be correlated with the averaged volume integral of a linear combination of two stress invariants. It is defined as follows:

$$G_\alpha(\sigma_{ij}, R) = \frac{1}{V_c}\int_{\Omega_c} (\alpha I_1 + (1-\alpha)\bar{\sigma})\, dV \left(\frac{1-R}{2}\right)^{1/2}, \quad 0 \le \alpha \le 1 \tag{A.1}$$

where σ_{ij} is the stress tensor field, $I_1 = \sigma_{kk}$ is the first stress invariant, $\bar{\sigma}$ is the von Mises stress, R is the cycle ratio, defined as the minimum normal stress divided by the maximum normal stress, and V_c is the volume of the domain of integration defined by

$$\Omega_c = \{\mathbf{x} \,|\, \sigma_1 > \beta\sigma_{\max} > 0\} \tag{A.2}$$

where σ_1 is the first principal stress and $\sigma_{\max} > 0$ is the maximum macroscopic stress. This is a generalization of the uniaxial stress to triaxial stress in the sense that G_α is defined for triaxial stress and, in the special case when constant uniaxial stress σ_1 is applied then it has the value of the equivalent stress σ_{eq}:

$$G_\alpha(\sigma_{ij}, R) = \sigma_{\text{eq}} \stackrel{\text{def}}{=} \sigma_1 \left(\frac{1-R}{2}\right)^{1/2}. \tag{A.3}$$

The parameter β depends on the material and a parameter that characterizes the stress gradient in the vicinity of stress raisers. In machine design this parameter is the notch radius. Since surface defects generally cannot be characterized by a single geometric parameter, we use the highly stressed volume V for that purpose. By definition,

$$V \stackrel{\text{def}}{=} \int_{\Omega_\varrho} y(\mathbf{x})\, dV \quad \text{where} \quad y = \begin{cases} 1 & \text{when } \sigma_1(\mathbf{x}) > \gamma\sigma_{\max} \\ 0 & \text{otherwise.} \end{cases} \tag{A.4}$$

The domain of integration Ω_ϱ is the neighborhood of a stress raiser. Denoting the location where σ_1 is maximum at a stress raiser by $\mathbf{x}_0$ we have $\Omega_\varrho = \{\mathbf{x} \,|\, |\mathbf{x}-\mathbf{x}_0| < \varrho\}$ where ϱ is chosen large enough to include all points where $\sigma_1(\mathbf{x}) > \gamma\sigma_{\max}$ and small enough to include only one stress raiser or one group of closely located stress raisers.

The three parameters of G_α are determined by calibration. Parameter α establishes a convex combination of the first stress invariant I_1 and the von Mises stress $\bar{\sigma}$, see equation(A.1). Parameter β defines the domain of integration which depends on the material properties and the stress field in the vicinity of stress raisers. The parameter γ is independent of the material properties. It defines the highly stressed volume V which depends on the stress distribution, and hence the type of loading, but is independent of the magnitude of the load. The predicted number of fatigue cycles is not sensitive to the choice of γ. In reference [7] $\gamma = 0.85$ was used.

Appendix B. The statistical model

The selection of a statistical models from among candidate models is discussed in [12]. Based on those results, we selected the random fatigue limit model proposed by Pascual and Meeker [13]. This model is based on the assumption that the random variable defined by $W = \log_{10} N$, where N is the number of cycles to failure, is normally distributed with mean $\mu(G_\alpha)$ and standard deviation s.

$$\mu(G_\alpha) = A_1 - A_2 \log_{10}(G_\alpha - A_3), \quad G_\alpha - A_3 > 0. \tag{B.1}$$

The parameter A_3, called the fatigue limit, is assumed to be a random variable. Specifically, $V \stackrel{\text{def}}{=} \log_{10} A_3$ is assumed to be normally distributed with mean μ_f and standard deviation s_f. Therefore the statistical model considered here has five parameters. The set of five parameters that maximize the likelihood function is denoted by $\boldsymbol{\theta}$.

We will assume that $V = \log_{10} A_3$ has normal distribution with mean μ_f and standard deviation s_f and write $A_3 = 10^v$. Therefore the random fatigue limit model

has five parameters: $\boldsymbol{\theta} \stackrel{\text{def}}{=} \{A_1\, A_2\, s\, \mu_f\, s_f\}$ and the probability density function of w, given G_α, v and $\boldsymbol{\theta}$ is

$$\phi(w \,|\, G_\alpha, v, \boldsymbol{\theta}) = \frac{\exp(-(w - \mu(G_\alpha, 10^v))^2/(2s^2))}{s\sqrt{2\pi}}. \tag{B.2}$$

The probability density of v, given G_α and $\boldsymbol{\theta}$, is:

$$f(v \,|\, G_\alpha, \boldsymbol{\theta}) = \frac{\exp(-(v - \mu_f)^2/(2s_f^2))}{s_f\sqrt{2\pi}}. \tag{B.3}$$

The marginal probability density of w is

$$\phi_M(w \,|\, G_\alpha, \boldsymbol{\theta}) = \int_{-\infty}^{\log_{10} G_\alpha} \phi(w \,|\, G_\alpha, v, \boldsymbol{\theta}) f(v \,|\, G_\alpha, \boldsymbol{\theta})\, dv \tag{B.4}$$

and the marginal cumulative distribution function is:

$$\begin{aligned} \Phi_M(w \,|\, G_\alpha, \boldsymbol{\theta}) &= \int_{-\infty}^{w} \phi_M(t \,|\, G_\alpha, \boldsymbol{\theta})\, dt \\ &= \frac{1}{2} \int_{-\infty}^{\log_{10} G_\alpha} \left(1 + \operatorname{erf}\left(\frac{w - \mu(G_\alpha, 10^v)}{s\sqrt{2}}\right)\right) f(v)\, dv. \end{aligned} \tag{B.5}$$

The functions ϕ_M and Φ_M have to be evaluated numerically.

Given a set of independent and identically distributed observations $(w_i,\, G_\alpha^{(i)})$, $(i = 1, 2, \ldots, n)$ the likelihood function is

$$L(\boldsymbol{\theta}) = \prod_{i=1}^{n} \left[\phi_M(w_i \,|\, G_\alpha^{(i)}, \boldsymbol{\theta}\right]^{1-\delta_i} \left[1 - \Phi_M(w_i \,|\, G_\alpha^{(i)}, \boldsymbol{\theta})\right]^{\delta_i} \tag{B.6}$$

where $\delta_i = 0$ (resp. $\delta_i = 1$) if the specimen failed (resp. did not fail) at $n_i = 10^{w_i}$ cycles.

The set of parameters $\boldsymbol{\theta}$ maximize $L(\boldsymbol{\theta})$, equivalently the log likelihood function $LL(\boldsymbol{\theta}) = \ln L(\boldsymbol{\theta})$, with respect to the S-N data.

Journal of Computational and Applied Mechanics, Vol. 16, No. 2, (2021), pp. 87–97
DOI: 10.32973/jcam.2021.006

A STEADY-STATE HEAT CONDUCTION PROBLEM OF A NONHOMOGENOUS CONICAL BODY

I. Ecsedi, A. Baksa
Institute of Applied Mechanics, University of Miskolc
3515 Miskolc-Egyetemváros, Hungary
istvan.ecsedi@uni-miskolc.hu attila.baksa@uni-miskolc.hu

[Received: April 14, 2021; Accepted: June 22, 2021]

Abstract. Numerous studies and textbooks deal with the steady-state thermal conduction of radially nonhomogeneous circular cylinder. In contrast, there are relatively few studies on the thermal conduction problems of conical solid bodies. This study is intended as a modest contribution to the solution of thermal conductance problems of nonhomogeneous conical bodies. A one-dimensional steady-state heat conduction in nonhomogeneous conical body is considered. The thermal conductivity of the hollow conical body in a suitable chosen spherical coordinate system depends on the polar angle but is independent of the radial coordinate and azimuthal angle coordinate. A functionally graded type of material inhomogeneity is considered. All results of the paper are based on Fourier's theory of heat conduction in solid bodies.

Mathematical Subject Classification: 80A20
Keywords: heat conduction, steady-state, conical body, nonhomogenous, functionally graded material

1. Introduction

Numerous studies and textbooks of heat transfer deal with the steady-state thermal conduction in radially nonhomogeneous circular cylinder [1–3]. A lot of papers consider the functionally graded material inhomogeneity of solid bodies. Functionally graded materials (FGMs) are new advanced heat resisting materials used in modern technologies [4, 5]. The basic concept is to mix the ceramic and metal such that the material properties continuously vary from one constituent material to other. The coefficients of governing equations for temperature distribution are coordinate dependent, as the thermal properties are function of position.

In an important paper by Porchaloempong et al. [6] a two-dimensional energy balance approach was used to model the temperature distribution in conduction heated conically shaped bodies. The numerical solution was based on finite differences. The cone was divided into small volume elements. The inner elements were concentric rings of rectangular cross sections while those at the side surfaces had trianglular cross sections. Energy balance equations for volume elements were solved explicitly. The conduction heat transfer model developed in this study can accurately predict the temperature distribution in a conically shaped container [6]. The paper [7] presents an

analytical solution for heat transfer in heterogeneous conical shells with temperature dependent conduction coefficients. The geometry of the shell is completely conically shaped. The heat transfer equation should be first transformed using the Kirchhoff transformation [7]. The obtained differential equation is solved by the Green function[7]. An exact analytical solution for anisotropic conductive heat transfer in composite conical shells is presented by Norouzi and Rahmani [8]. The shell has a full conical shape and the fibers are winded around the conical body. The exact solution of the temperature field is obtained via the separation of variables method. The developed analytical solution is validated by a numerical solution [8].

This study is intended as a modest contribution to the solution of the thermal conductance problem of a hollow conical body made of functionally graded material. The thermal conductivity in a suitable chosen spherical coordinate system depends on the polar angle but it is independent of the radial coordinate and azimuthal angle coordinate. Two types of the polar-nonhomogeneity are considered which are the power nonhomogeneity and the exponential nonhomogeneity [4, 5].

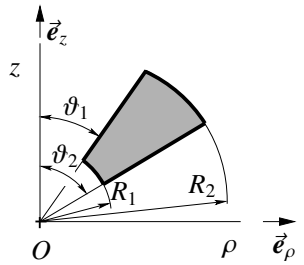

Figure 1. Meridian section of the conical body

Figure 1 shows the meridian section of the hollow conical body which is bordered by two conical and two spherical surfaces. The definition of the spherical coordinates r, φ, ϑ are given in Figure 2.

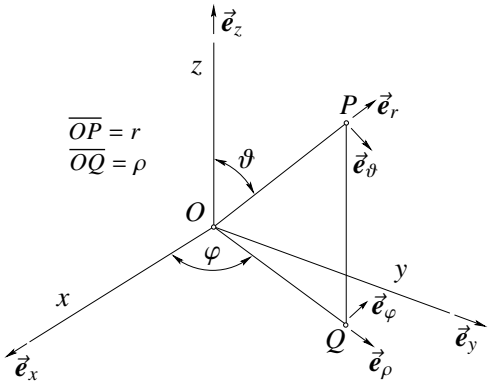

Figure 2. Spherical coordinate system

The space domain occupied by the conical body is denoted by B

$$B = \left\{ (r, \varphi, \vartheta) \middle| R_1 \leq r \leq R_2,\, 0 \leq \varphi \leq 2\pi,\, 0 \leq \vartheta_1 \leq \vartheta_2 \leq \pi \right\}. \tag{1.1}$$

The boundary conditions for the considered steady-state heat conduction are

$$\frac{\partial T}{\partial r} = 0 \qquad r = R_1 \quad 0 \leq \varphi \leq 2\pi \quad \vartheta_1 \leq \vartheta \leq \vartheta_2, \tag{1.2}$$

$$\frac{\partial T}{\partial r} = 0 \qquad r = R_2 \quad 0 \leq \varphi \leq 2\pi \quad \vartheta_1 \leq \vartheta \leq \vartheta_2, \tag{1.3}$$

$$-\frac{k(\vartheta)}{h_1}\frac{\partial T}{\partial \vartheta} + T = t_1 \qquad \vartheta = \vartheta_1 \quad 0 \leq \varphi \leq 2\pi \quad R_1 \leq r \leq R_2, \tag{1.4}$$

$$\frac{k(\vartheta)}{h_2}\frac{\partial T}{\partial \vartheta} + T = t_2 \qquad \vartheta = \vartheta_2 \quad 0 \leq \varphi \leq 2\pi \quad R_1 \leq r \leq R_2. \tag{1.5}$$

In equations (1.2)-(1.5) $T = T(r, \varphi, \vartheta)$ is the temperature field of the nonhomogeneous conical body, $k = k(\vartheta)$ is the thermal conductance, h_1 and h_2 are the heat transfer coefficients and h_i = constants $(i = 1, 2)$. The temperatures of surrounding medium at the inner and outer conical boundary surfaces are denoted by t_1 = constant, t_2 = constant, they are given. The boundary conditions (1.2) and (1.3) express that, the spherical surfaces at $r = R_1$ and $r = R_2$ are thermal insulated surfaces [1–3, 9].

In the present problem according to the Fourier's theory of heat conduction in a solid nonhomogeneous body we have

$$\boldsymbol{q} = -k(\vartheta)\nabla T \qquad \nabla = \frac{\partial}{\partial r}\boldsymbol{e}_r + \frac{1}{r\sin\vartheta}\frac{\partial}{\partial \varphi}\boldsymbol{e}_\varphi + \frac{1}{r}\frac{\partial}{\partial \vartheta}\boldsymbol{e}_\vartheta, \tag{1.6}$$

$$\nabla \cdot \boldsymbol{q} = 0 \qquad (r, \varphi, \vartheta) \in B. \tag{1.7}$$

The unit vectors of spherical coordinate system $Or\varphi\vartheta$ are $\boldsymbol{e}_r$, $\boldsymbol{e}_\varphi$ and $\boldsymbol{e}_\vartheta$ (Fig. 2), and in equations (1.7) and (1.8) the dot denotes the scalar product of two vectors. The heat flux vector is denoted by $\boldsymbol{q}$. The substitution of equation (1.6_1) into equation (1.8) gives [10]

$$\nabla \cdot (k(\vartheta)\nabla T) = k(\vartheta) \triangle T + \nabla k \cdot \nabla T = k(\vartheta)\left[\frac{1}{r^2}\frac{\partial}{\partial r}\left(r^2\frac{\partial T}{\partial r}\right) + \right.$$
$$\left. \frac{1}{r^2\sin\vartheta}\frac{\partial}{\partial \vartheta}\left(\sin\vartheta\frac{\partial T}{\partial \vartheta}\right) + \frac{1}{r^2\sin^2\vartheta}\frac{\partial^2 T}{\partial \varphi^2}\right] + \frac{1}{r^2}\frac{\partial k}{\partial \vartheta}\frac{\partial T}{\partial \vartheta} = 0 \qquad (r, \varphi, \vartheta) \in B. \tag{1.8}$$

We assume that $T = T(\vartheta)$, that is the temperature field depends on only the polar angle ϑ. This assumption leads to an ordinary differential equation for $T = T(\vartheta)$

$$\frac{k(\vartheta)}{\sin\vartheta}\frac{\mathrm{d}}{\mathrm{d}\vartheta}\left(\sin\vartheta\frac{\mathrm{d}T}{\mathrm{d}\vartheta}\right) + \frac{\mathrm{d}k}{\mathrm{d}\vartheta}\frac{\mathrm{d}T}{\mathrm{d}\vartheta} = 0, \qquad \vartheta_1 < \vartheta < \vartheta_2, \tag{1.9}$$

It is obvious that $T = T(\vartheta)$ satisfies the two-point boundary conditions

$$-\frac{k(\vartheta_1)}{h_1}\left(\frac{\mathrm{d}T}{\mathrm{d}\vartheta}\right)_{\vartheta=\vartheta_1} + T_1 = t_1, \qquad T_1 = T(\vartheta_1), \tag{1.10}$$

$$\frac{k(\vartheta_2)}{h_2}\left(\frac{\mathrm{d}T}{\mathrm{d}\vartheta}\right)_{\vartheta=\vartheta_2}+T_2=t_2,\qquad T_2=T(\vartheta_2). \tag{1.11}$$

2. Solution of the heat conduction boundary-value problem

The general solution of a second order ordinary differential equation (1.9) can be represented as [10]

$$T(\vartheta)=C_1\int\limits_{\vartheta_1}^{\vartheta}\frac{\mathrm{d}\omega}{k(\omega)\sin\omega}+C_2,\qquad \vartheta_1\le\vartheta\le\vartheta_2, \tag{2.1}$$

where C_1 and C_2 are arbitrary constants whose values can be determined by the use of boundary conditions (1.10) and (1.11). We give the expressions of the constants of integration in terms of $T_1=T(\vartheta_1)$ and $T_2=T(\vartheta_2)$

$$C_1=\frac{T_2-T_1}{\int\limits_{\vartheta_1}^{\vartheta_2}\frac{\mathrm{d}\vartheta}{k(\vartheta)\sin\vartheta}},\qquad C_2=T_1. \tag{2.2}$$

The temperature field in the polar-nonhomogeneous conical body in terms of T_1 and T_2 is as follows

$$T(\vartheta)=T_1+(T_2-T_1)\frac{\int\limits_{\vartheta_1}^{\vartheta}\frac{\mathrm{d}\omega}{k(\omega)\sin\omega}}{\int\limits_{\vartheta_1}^{\vartheta_2}\frac{\mathrm{d}\vartheta}{k(\vartheta)\sin\vartheta}},\qquad \vartheta_1\le\vartheta\le\vartheta_2, \tag{2.3}$$

and we have

$$k(\vartheta)\frac{\mathrm{d}T}{\mathrm{d}\vartheta}=\frac{T_2-T_1}{\int\limits_{\vartheta_1}^{\vartheta_2}\frac{\mathrm{d}\vartheta}{k(\vartheta)\sin\vartheta}}. \tag{2.4}$$

Formula (2.4) shows that $T=T(\vartheta)$ increases monotonically in $\vartheta_1\le\vartheta\le\vartheta_2$, if $T_2>T_1$ and $T=T(\vartheta)$ is monotonic decrease in $\vartheta_1<\vartheta<\vartheta_2$ if $T_1>T_2$.

Substitution of equations (2.3) and (2.4) into equation (1.10), (1.11) yields a system of linear equations for the unknown boundary temperature T_1 and T_2. The solution of this system of linear equations can be represented as

$$T_1=t_1\frac{1+a_2}{1+a_1+a_2}+t_2\frac{a_1}{1+a_1+a_2}, \tag{2.5}$$

$$T_2=t_1\frac{a_2}{1+a_1+a_2}+t_2\frac{1+a_1}{1+a_1+a_2}. \tag{2.6}$$

In equations (2.5) and (2.6)

$$a_1=\frac{1}{h_1\sin\vartheta_1\int\limits_{\vartheta_1}^{\vartheta_2}\frac{\mathrm{d}\vartheta}{k(\vartheta)\sin\vartheta}},\qquad a_2=\frac{1}{h_2\sin\vartheta_2\int\limits_{\vartheta_1}^{\vartheta_2}\frac{\mathrm{d}\vartheta}{k(\vartheta)\sin\vartheta}}. \tag{2.7}$$

It is evident, that

$$\lim_{h_i \to \infty} a_i = 0 \qquad (i = 1, 2), \tag{2.8}$$

then the Robin's type boundary conditions (1.10) and (1.11) are replaced by Dirichlet type boundary conditions that is

$$\text{for } \; h_i = \infty \qquad T(\vartheta_i) = t_i \quad (i = 1, 2). \tag{2.9}$$

3. Examples

3.1. **Homogeneous conical body.** For a homogeneous conical body $k = k_0 =$ constant. In this case

$$T(\vartheta) = T_1 + (T_2 - T_1) \frac{\ln \left| \dfrac{\tan \dfrac{\vartheta}{2}}{\tan \dfrac{\vartheta_1}{2}} \right|}{\ln \left| \dfrac{\tan \dfrac{\vartheta_2}{2}}{\tan \dfrac{\vartheta_1}{2}} \right|}. \tag{3.1}$$

and

$$a_i = \frac{k_0}{h_i \sin \vartheta_i \ln \left| \dfrac{\tan \dfrac{\vartheta_2}{2}}{\tan \dfrac{\vartheta_1}{2}} \right|} \qquad (i = 1, 2). \tag{3.2}$$

It is worth noticing that if $\delta = \vartheta_2 - \vartheta_1 << \vartheta_1$ and $\varepsilon = \vartheta - \vartheta_1$ then

$$\sin \vartheta = \sin(\vartheta_1 + \varepsilon) = \sin \vartheta_1 \cos \varepsilon + \cos \vartheta_1 \sin \varepsilon \approx \sin \vartheta_1 + \varepsilon \cos \vartheta_1, \tag{3.3}$$

$$\frac{1}{\sin \vartheta} \approx \frac{1}{\sin \vartheta_1 (1 + \varepsilon \dfrac{\cos \vartheta_1}{\sin \vartheta_1})} \approx \frac{1}{\sin \vartheta_1 \left[1 + (\vartheta - \vartheta_1) \dfrac{\cos \vartheta_1}{\sin \vartheta_1} \right]} \approx \frac{1}{\sin \vartheta} \left[1 - (\vartheta - \vartheta_1) \frac{\cos \vartheta_1}{\sin \vartheta_1} \right], \tag{3.4}$$

$$\int_{\vartheta_1}^{\vartheta} \frac{\mathrm{d}\vartheta}{\sin \vartheta} \approx \frac{1}{\sin \vartheta_1} (\vartheta - \vartheta_1). \tag{3.5}$$

Substitution of equation (3.5) into equation (2.3) gives an approximation formula for the temperature distribution across the thickness of thin-walled conical tube

$$T(\vartheta) = T_1 + (T_2 - T_1) \frac{\vartheta - \vartheta_1}{\vartheta_2 - \vartheta_1}. \tag{3.6}$$

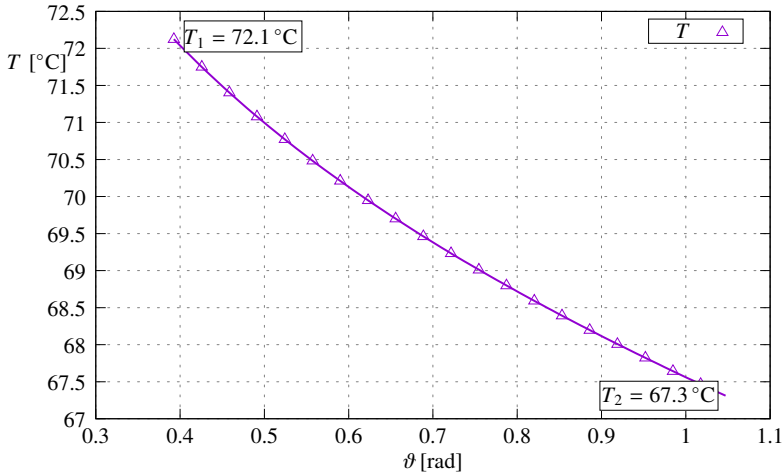

Figure 3. Illustration of temperature in a conical body as a function of ϑ

Figure 3 shows the temperature as a function of polar angle ϑ for the homogeneous conical body, if

$$t_1 = 298\,\mathrm{K} = 25\,^\circ\mathrm{C}, \quad t_2 = 393\,\mathrm{K} = 120\,^\circ\mathrm{C}, \quad \vartheta_1 = \frac{\pi}{8}, \quad \vartheta_2 = \frac{\pi}{3}, \quad R_1 = 0.4\,\mathrm{m},$$
$$R_2 = 2\,\mathrm{m}, \quad k_0 = 81.1\,\frac{\mathrm{W}}{\mathrm{Km}}, \quad h_1 = 20\,\frac{\mathrm{W}}{\mathrm{Km}^2}, \quad h_2 = 10\,\frac{\mathrm{W}}{\mathrm{Km}^2}.$$

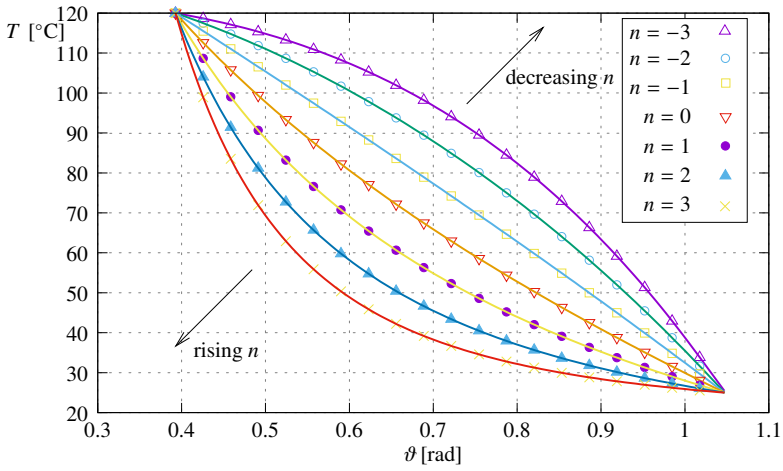

Figure 4. Temperature distribution in conical body for seven different values of power index n

3.2. **Power law nonhomogeneity.** In this case the thermal nonhomogeneity has the form

$$k(\vartheta) = k_0 \left(\frac{\vartheta}{\vartheta_1}\right)^n \qquad k_0 = \text{constants}, \quad \vartheta_1 \le \vartheta \le \vartheta_2, \tag{3.7}$$

where n is the power index. The applied thermal boundary conditions at $\vartheta = \vartheta_1$ and at $\vartheta = \vartheta_2$ are Dirichlet's type, the inner and outer boundary conical surfaces have prescribed temperatures. The plots of $T = T(\vartheta, n)$ for seven different values of power index n ($n = -3, -2, -1, 0, 1, 2, 3$) are shown in Figure 4, if

$$\vartheta_1 = \frac{\pi}{8}, \quad \vartheta_2 = \frac{\pi}{3}, \quad R_1 = 0.4\,\text{m}, \quad R_2 = 0.8\,\text{m}, \quad k_0 = 81.1\,\frac{\text{W}}{\text{Km}},.$$

3.3. **Exponential nonhomogeneity.** In this example the same data are used as in Examples 3.2 except $k = k(\vartheta)$. The polar-nonhomogeneity of the exponentially graded hollow conical body is

$$k(\vartheta) = k_0 \exp(\beta\vartheta) \qquad \vartheta_1 \le \vartheta \le \vartheta_2. \tag{3.8}$$

In equation (3.8) β is a material property [4, 5]. The plots of the function $T = T(\vartheta, \beta)$ against ϑ for seven different values of graded parameter β are shown in Figure 5 ($\beta = -4.0, -2.5, -1.0, 0.0, 1.0, 2.5, 4.0$) .

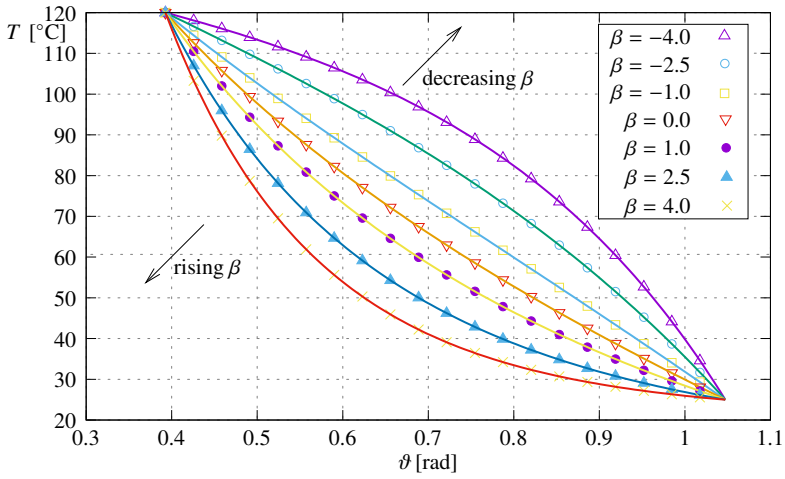

Figure 5. Temperature distribution in conical hollow body for seven different values of power index β

4. Overall heat transfer coefficient.

The overall heat transfer coefficient in steady state heat conduction problem is an important structural property of a solid body in which the heat is flowing between the two separated parts of its boundary surfaces. From the higher temperature boundary part of the body to the lower temperature boundary part of the body the process of

heat flow is characterized by the overall heat transfer coefficient according to equation (4.1)

$$Q = \Lambda(T_2 - T_1), \qquad T_2 > T_1, \tag{4.1}$$

where Q is the heat flow in unit time, T_1 and T_2 are given temperatures and Λ is the overall heat transfer coefficient.

In the present problem, the heat flow between the conical surfaces ∂B_1 and ∂B_2

$$\partial B_1 = \{(r, \varphi, \vartheta) \,|\, R_1 \le r \le R_2,\ 0 \le \varphi \le 2\pi,\ \vartheta = \vartheta_1\}, \tag{4.2}$$

$$\partial B_2 = \{(r, \varphi, \vartheta) \,|\, R_1 \le r \le R_2,\ 0 \le \varphi \le 2\pi,\ \vartheta = \vartheta_2\}, \tag{4.3}$$

can be obtained from the equation (4.4)

$$Q = -\int\limits_{\partial B_1} \frac{k(\vartheta)}{r} \frac{\mathrm{d}T}{\mathrm{d}\vartheta}\, \mathrm{d}A. \tag{4.4}$$

The area element of the boundary surface segment ∂B_1 is

$$\mathrm{d}A = 2\pi r \sin\vartheta_1\, \mathrm{d}r. \tag{4.5}$$

Substitution of equation (2.3) and equation (4.5) into the formula of heat flow Q (4.4) gives

$$Q = (T_2 - T_1) \frac{2\pi(R_2 - R_1)}{\int\limits_{\vartheta_2}^{\vartheta_1} \dfrac{\mathrm{d}\vartheta}{k(\vartheta)\sin\vartheta}}. \tag{4.6}$$

From equations (4.1) and (4.6) it follows that

$$\Lambda = \frac{\int\limits_{\vartheta_1}^{\vartheta_2} \dfrac{\mathrm{d}\vartheta}{k(\vartheta)\sin\vartheta}}{2\pi(R_2 - R_1)}. \tag{4.7}$$

The effect of nonhomogeneity on the overall heat transfer coefficient will be analysed for two types of polar nonhomogeneity. In both cases, the following data are used:

$$\vartheta_1 = \frac{\pi}{8}, \quad \vartheta_2 = \frac{\pi}{3}, \quad R_1 = 0.4\,\mathrm{m}, \quad R_2 = 2\,\mathrm{m}, \quad k_0 = 81.1\,\frac{\mathrm{W}}{\mathrm{Km}}. \tag{4.8}$$

4.1. **Power nonhomogeneity.** In this case

$$k(\vartheta) = k_0 \left(\frac{\vartheta}{\vartheta_1}\right)^n \qquad -4 \le n \le 4. \tag{4.9}$$

The plot of the function $\Lambda = \Lambda(n)$ against n is presented in Figure 6. The relation between $\Lambda(-4)$ and $\Lambda(4)$ can be considered a kind of degree of the power nonhomogeneity

$$\frac{\Lambda(-4)}{\Lambda(4)} = 54.9186. \tag{4.10}$$

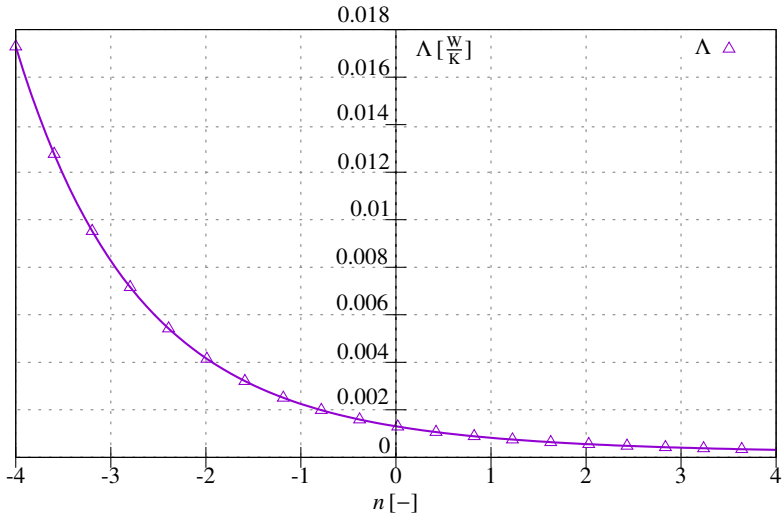

Figure 6. The overall heat transfer coefficient as a function of power index n of inhomogeneity

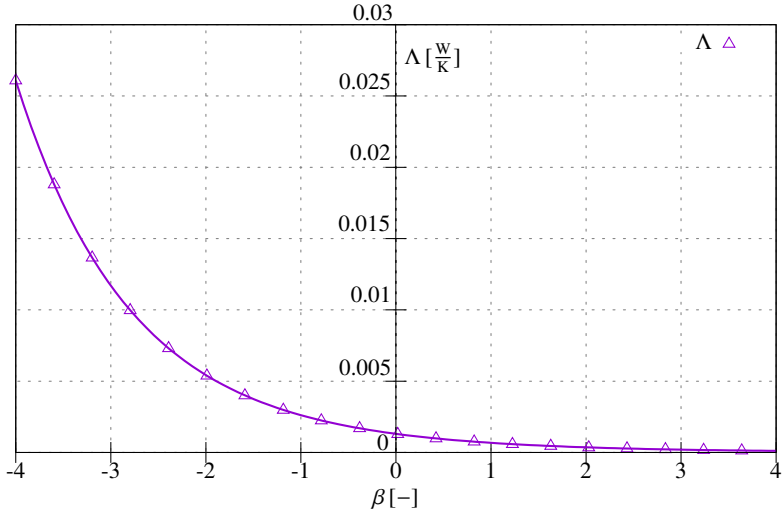

Figure 7. The overall heat transfer coefficient as a function of inhomogeneity parameter β

4.2. **Exponentially nonhomogeneity.** The exponentially nonhomogeneity of the polar-nonhomogeneous hollow conical body is described by equation (4.11)

$$k(\vartheta) = k_0 \exp(\beta\vartheta) \qquad -4 \leq \beta \leq 4. \tag{4.11}$$

The plot of the function $\Lambda = \Lambda(\beta)$ is shown in Figure 7 for $-4 \leq \beta \leq 4$. The kind of degree of exponentially nonhomogeneity can be characterized by the ratio of $\Lambda(-4)$

to $\Lambda(4)$. In the present problem

$$\frac{\Lambda(-4)}{\Lambda(4)} = 230.97. \tag{4.12}$$

5. Conclusions

A one-dimensional steady-state heat conduction problem of a nonhomogenous hollow conical body is solved. The considered conical body is bordered by two conical surfaces and two spherical surfaces. The thermal conductance depends on the polar angle in a suitably chosen spherical coordinate system. Two-types of the polar-nonhomogeneity are considered. Firstly, the power nonhomogeneity is analyzed and secondly the exponentially nonhomogeneity is considered. For both cases the overall heat transfer coefficient is computed. The presented analytical solution of the temperature field can be used in the solution of stationary thermoelastic problems, when the temperature field separates from the elastic field. In this case the elastic and the temperature fields are uncoupled. Another possible application of the numerical results of this paper is to verify the accuracy of the usual numerical methods such as FEM, finite-difference method, boundary element method, etc.

References

1. H. S. Carslaw and J. C. Jaeger. *Conduction of Heat in Solids*. London, Oxford, 1947.
2. M. N. Ozisik. *Boundary Value Problmes of Heat Conduction*. Scranton, Ps., International Textbook, 1968.
3. S. Whitaker. *Foundamental Principles of Heat Transfer*. Pergamon Press Inc., New York, 2013.
4. S. Suresh and A. Mortensen. *Fundamentals of Functionally Graded Materials*. IOM Communications, New Yersy, 2003.
5. Y. Miyamoto, W. A. Kaysser, and B. H. Robin. *Functionally Grade Materials: Deisgn, Proessing and Applications*. Boston, UK Kluwer Academic Publishers, 1999.
6. P. Pornchaloempong, M. O. Balaban, K. V. Chan, and A. A. Teixera. "Numerical solution of conduction heating in conical shape bodies." *Journal of Food Process Engineering,* **25**, (2003), pp. 539–555. DOI: 10.1111/j.1745-4530.2003.tb00650.x.
7. B. E. Manesh, M. M. Shahmardoan, and M. Norouzi. "Analytical solution of heat transfer in heterogeneous composite coniceal shells with temperature dependent coefficients." *Amirkabir Journal of Mechanical Engineering* **52**9, (2020), pp. 639–642. DOI: 10.22060/mej.2019.15168.6050.
8. M. Norowzi and H. Rahmani. "On exact solution for anisotropic heat conduction in composite conical shells." *International Journal of Thermal Stresses* **94**, (2015), pp. 110–125. DOI: 10.1016/j.ijthermalsci.2015.02.018.

9. B. Sunddén. *Introduction to Heat Transfer*. WIT Press, Southampton, Boston, 2012.
10. G.A. Korn and T.M. Korn. *Mathematical Handbook for Scientists and Engineergs*. New York: D von Nostrand, 1961.

Journal of Computational and Applied Mechanics, Vol. 16, No. 2, (2021), pp. 99–128
DOI: 10.32973/jcam.2021.007

VIBRATION OF AN AXIALLY LOADED HETEROGENEOUS PINNED-PINNED BEAM WITH AN INTERMEDIATE ROLLER SUPPORT

L. Kiss, G. Szeidl and M. Abderrazek
Institute of Applied Mechanics, University of Miskolc
3515 Miskolc-Egyetemváros, Hungary
mechkiss@uni-miskolc.hu,gyorgy.szeidl@uni-miskolc.hu
abderrazekmessoudi1995@gmail.com

[Received: September 19, 2021; Accepted: November 3, 2021]

Dedicated to Professor Tibor Czibere on the occasion of his 90th birthday

Abstract. The present paper is devoted to the issue of what effect the axial load (compressive or tensile) has on the eigenfrequencies of a heterogeneous pinned-pinned beam with an intermediate roller support (called a PrsP beam). This problem is a three point boundary value problem (eigenvalue problem) associated with homogeneous boundary conditions. If the Green functions of the three point boundary value problem (BVP) are known the eigenvalue problem that provide the eigenfrequencies for the beam loaded axially can be transformed into an eigenvalue problem governed by a homogeneous Fredholm integral equation. The later eigenvalue problems can be reduced to an algebraic eigenvalue problem which then can be solved numerically by using an effective solution algorithm which is based on the boundary element method.

Mathematical Subject Classification: 34B27, 45c05, 74K10
Keywords: Heterogeneous beam, axially loaded, three point boundary value problem, vibration, Green's function, Fredholm integral equation

1. Introduction

Beams are quite often used as various structural elements because of their favorable load-bearing capabilities. Various such problems have been solved [1–3]. Nowadays, nonhomogeneous (heterogeneous or inhomogeneous) curved beams are also becoming more and more common. The benefits of such structural members can be the reduced weight and the higher strength. A class of inhomogeneity, namely, cross-sectional inhomogeneity means that the material parameters, like the Young modulus, are functions of the cross-sectional coordinates.

As for vibrations of beams, there are some recent results that must be mentioned. Bizzi et al. give an analytical solution to the mode-shape equation of Timoshenko beams vibrating under gravity loading in [4]. Ondra and Titurus [5] study systems of beams with tendon loading. The effect of the number and location of the attachment points is investigated on the vibrations of these systems is investigated. Bozyigit et al. [6] aim to find the effectiveness of the Adomian decomposition method and the differential transformation method on the vibrations of axially loaded Timoshenko beams. Mirzabeigy and Madoliat [7] focus on the vibrations of axially loaded beams resting on variable elastic foundation while Wu and Chang [8] tackle the vibrations of

axially loaded multi-step Timoshenko beams carrying multiple concentrated elements. The continuous mass transfer matrix is used in the later article to find solutions.

At the same time, it seems that, meanwhile the Green function is commonly used for various straight beam problems. Lueschen et al [9] consider Timoshenko and Euler-Bernoulli beams - the Green function is given in closed-form for vibration problems. Foda and Abduljabbar [10] deal with the dynamic response of an Euler-Bernoulli beam finding the response of the beam to a moving mass. Kukla and Zamojska make some efforts in [11] to tackle the vibrations of an axially loaded tapered beam. The beam can consist of an arbitrary number of segments so the model can serve as approximation for continuously varying cross-sections. Failla and Santini [12] solve the bending problem of discontinuous beams - there are constraints along the beam axis and flexural stiffness jumps. An efficient algorithm is developed based on the Green function.

Based on the above literature research, in this article, it is our main objective to clarify what effect the axial force has on the eigenfrequencies of a pinned-pined beam with an intermediate roller support. The material is linearly elastic, isotropic. However, the elastic coefficients can change over the cross-section – this material behavior is called cross-sectional inhomogeneity. The governing equations of the corresponding equilibrium problem constitute a three-point boundary value problem. Its solution can be given in a closed form provided that the Green function is known. By utilizing the definition of the Green function we calculate the elements which make possible to calculate it. With the Green function the three-point eigenvalue problem that provides eigenfrequencies as a function of the axial force is replaced by a homogeneous Fredholm integral equation in which the Green function is the kernel. Then the eigenvalue problem governed by the homogeneous Fredholm integral equation is reduced to an algebraic eigenvalue problem by using the boundary element technique.

The paper is organized in five sections. Section 2 presents the differential equation of the problem and the corresponding boundary and continuity conditions in a dimensionless formulation. Section 3 provides the definition of the Green function for three-point boundary value problems. It is worth mentioning that the definition is a constructive one since it makes the calculation of the Green functions possible for the cases of compressive and tensile forces possible. The calculations are detailed in Section 4. The numerical results are presented in Section 5. The last section contains the conclusions.

2. Differential equations

2.1. **Governing equations.** The pinned-pinned beam with an intermediate roller support (PrsP beam) is shown in Figure 1. The axial force N ($N > 0$) is compressive in this Figure. The beam has a uniform cross section throughout its length. The E-weighted centerline [13] (called centerline for short) of the beam coincides with the axis $\hat{x}$ of the coordinate system $\hat{x}, \hat{y}, \hat{z}$. Its origin is at the left end of the centerline. It is assumed that the coordinate plane $\hat{x}\hat{z}$ is a symmetry plane of the beam. It is also assumed that the modulus of elasticity E satisfies the relation $E(\hat{y}, \hat{z}) = E(-\hat{y}, \hat{z})$ over

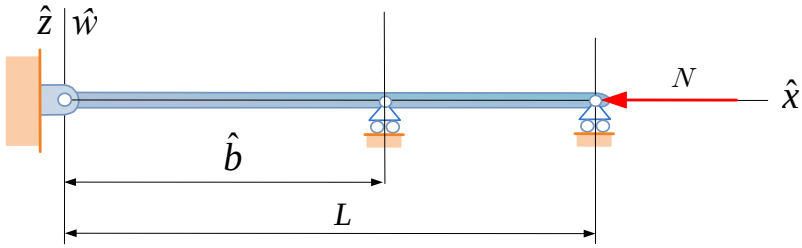

Figure 1.

the cross section A, which means that (a) it is an even function of $\hat{y}$ and (b) it is independent of the coordinate $\hat{x}$. In this case we speak about cross sectional heterogeneity.

We remark that the E-weighted first moment $Q_{\hat{y}}$ of the cross section is zero in this coordinate system [13]:

$$Q_{\hat{y}} = \int_A \hat{y} E(\hat{y}, \hat{z}) \, \mathrm{d}A = 0$$

The length of the beam is L, the position of the middle support is given by $\hat{b}$.

Equilibrium problems of Euler-Bernoulli beams with cross sectional heterogeneity are governed by the ordinary differential equation:

$$\frac{\mathrm{d}^4 \hat{w}}{\mathrm{d}\hat{x}^4} \pm \hat{\mathcal{N}} \frac{\mathrm{d}^2 \hat{w}}{\mathrm{d}\hat{x}^2} = \frac{\hat{f}_z}{I_{ey}}, \qquad \hat{\mathcal{N}} = \frac{N}{I_{ey}} \tag{2.1}$$

where the sign of $\hat{\mathcal{N}}$ is (positive)[negative] if the axial force is (comressive)[tensile], $\hat{w}(x)$ is the vertical displacement of the material points on the centerline, $\hat{f}_z(\hat{x})$ is the intensity of the distributed load acting on the centerline and I_{ey} is defined by the equation

$$I_{ey} = \int_A E(\hat{y}, \hat{z}) z^2 \, \mathrm{d}A \,, \tag{2.2}$$

where A is the area of the cross section. If E is constant the beam is homogeneous and

$$I_{ey} = IE, \qquad I = \int_A z^2 \, \mathrm{d}A \tag{2.3}$$

in which I is the moment of inertia. It is noted that the effect of the material composition on I_{ey} is demonstrated through examples in [14].

In what follows we shall use dimensionless variables defined by the following relations

$$\begin{aligned} x = \hat{x}/L, \qquad & \xi = \hat{\xi}/L, \qquad & w = \hat{w}/L, \\ y = \frac{\mathrm{d}\hat{w}}{\mathrm{d}\hat{x}} = \frac{\mathrm{d}w}{\mathrm{d}x}, \qquad & b = \hat{b}/\ell \,, \qquad & \ell = \left.\frac{\hat{x}}{L}\right|_{\hat{x}=L} = 1 \,, \end{aligned} \tag{2.4}$$

where $\hat{\xi}$ is also a coordinate on the axis x introduced here for our later considerations. Applying dimensionless quantities to equation (2.1) we have

$$\frac{\mathrm{d}^4 w}{\mathrm{d}x^4} \pm \mathcal{N}\frac{\mathrm{d}^2 w}{\mathrm{d}x^2} = f_z\,, \qquad \mathcal{N} = L^2\hat{\mathcal{N}} = \frac{L^2 N}{I_{ey}} \qquad f_z = \frac{L^3 \hat{f}_z}{I_{ey}} \tag{2.5}$$

Table 1.

Boundary conditions	
$w(0) = 0\,,\ w^{(2)}(0) = 0$	$w(\ell) = 0\,,\ w^{(2)}(\ell) = 0$
Continuity conditions	
$w(b-0) = 0\,,$	$w(b+0) = 0$
$w^{(1)}(b-0) = w^{(1)}(b+0)$	
$w^{(2)}(b-0) = w^{(2)}(b+0)$	

Equation (2.5) is associated with the boundary and continuity conditions presented in Table 1.

We remark that the general solution of the homogeneous differential equation

$$w^{(4)} \pm \mathcal{N} w^{(2)} = 0\,, \qquad w^{(n)} = \begin{cases} w & \text{if } n = 0 \\ \dfrac{\mathrm{d}^n w}{\mathrm{d}x^n} & \text{if } n = 1, 2, \ldots \end{cases} \tag{2.6a}$$

is very simple, i.e.,

$$w = \sum_{\ell=1}^{4} a_\ell w_\ell(x) = a_1 + a_2 x + a_3 \cos px + a_4 \sin px, \qquad p = \sqrt{\mathcal{N}} \tag{2.6b}$$

if the sign of $\mathcal{N}$ is positive – $a_1, \ldots, a_4$ are undetermined integration constants – and

$$w = \sum_{\ell=1}^{4} a_\ell w_\ell(x) = a_1 + a_2 x + a_3 \cosh px + a_4 \sinh px, \qquad p = \sqrt{\mathcal{N}}. \tag{2.6c}$$

if the sign of $\mathcal{N}$ is negative. Note that $a_1, \ldots, a_4$ are different integration constants in equations (2.6b) and (2.6c).

If we know the Green function $G(x, \xi)$ for the boundary value problem determined by ODE (2.5) and the boundary and continuity conditions presented in Table 1 the solution for the dimensionless deflection $w(x)$ due to the dimensionless load $f_z(\xi)$ is given by the following integral:

$$w(x) = \int_0^\ell G(x, \xi) f_z(\xi)\, \mathrm{d}\xi \tag{2.7}$$

The definition of the Green function we need is presented in Section 3.

3. Green function for three-point boundary value problems

3.1. **Definition.** We shall consider the in-homogeneous ordinary differential equation

$$L[y(x)] = r(x)\,, \tag{3.1}$$

where the differential operator of order $2k$ is defined by the following equation

$$L[y(x)] = \sum_{n=0}^{2k} p_n(x) y^{(n)}(x) \tag{3.2}$$

in which k is a natural number, the functions $p_n(x)$ and $r(x)$ are continuous and $p_{2k}(x) \neq 0$ if $x \in [0, \ell]$ ($\ell > 0$). Moreover let b be an inner point in the interval $[0, \ell]$: $b = \ell_1$, $\ell - b = \ell_2$ and $\ell_1 + \ell_2 = \ell$.

We assume that the inhomogeneous differential equation (3.1) is associated with homogeneous boundary and continuity conditions given by the following equations:

$$\begin{aligned} U_{0r}[y] &= \sum_{n=0}^{2k} \alpha_{nrI} y_I^{(n-1)}(0) = 0, \qquad r = 1, 2, \ldots, k \\ U_{br}[y] &= \sum_{n=0}^{2k} \beta_{nrI} y_I^{(n-1)}(b) - \sum_{n=0}^{2k} \beta_{nrII} y_{II}^{(n-1)}(b) = 0, \qquad r = 1, 2, ..., 2k \\ U_{\ell r}[y] &= \sum_{n=0}^{2k} \gamma_{nrII} y_{II}^{(n-1)}(\ell) = 0, \qquad r = 1, 2, \ldots, k \end{aligned} \tag{3.3}$$

The Latin subscripts I and II refer successively to the intervals $[0, b]$ and $[b, \ell]$: y_I and y_{II} are the solutions to the differential equation in the interval I and II while α_{nrI}, β_{nrI}, β_{nrII} and γ_{nrII} are arbitrary constants.

In accordance with equation (2.7) solution of the three-point boundary value problem (3.1), (3.2) and (3.3) is sought in the following form:

$$y(x) = \int_0^\ell G(x, \xi) r(\xi) \mathrm{d}\xi, \tag{3.4}$$

where the function $G(x, \xi)$ is the Green function defined by the following formulas and properties [15]:
Formulas:

$$G(x, \xi) = \begin{cases} G_{1I}(x, \xi) & \text{if } x, \xi \in [0, b], \\ G_{2I}(x, \xi) & \text{if } x \in [b, \ell] \text{ and } \xi \in [0, b], \\ G_{1II}(x, \xi) & \text{if } x \in [0, b] \text{ and } \xi \in [b, \ell], \\ G_{2II}(x, \xi) & \text{if } x, \xi \in [b, \ell]. \end{cases} \tag{3.5}$$

Properties:
1. The function $G_{1I}(x, \xi)$ is a continuous function of x and ξ if $0 \leq x \leq \xi \leq b$ and $0 \leq \xi \leq x \leq b$. In addition it is $2k$ times differentiable with respect to x and the derivatives

$$\frac{\partial^n G_{1I}(x, \xi)}{\partial x^n} = G_{1I}(x, \xi)^{(n)}(x, \xi)\,, \qquad n = 1, 2, \ldots, 2k \tag{3.6}$$

are also continuous functions of x and ξ in the triangles $0 \le x \le \xi \le b$ and $0 \le \xi \le x \le b$.

2. Let ξ be fixed in $[0, b]$. The function $G_{1I}(x, \xi)$ and its derivatives

$$G_{1I}^{(n)}(x, \xi) = \frac{\partial^n G_{1I}(x, \xi)}{\partial x^n}, \qquad n = 1, 2, \ldots, 2k-2 \tag{3.7}$$

should be continuous for $x = \xi$:

$$\lim_{\varepsilon \to 0} \left[G_{1I}^{(n)}(\xi + \varepsilon, \xi) - G_{1I}^{(n)}(\xi - \varepsilon, \xi) \right] = \\ = \left[G_{1I}^{(n)}(\xi + 0, \xi) - G_{1I}^{(n)}(\xi - 0, \xi) \right] = 0 \quad n = 0, 1, 2, \ldots 2k-2 \tag{3.8a}$$

The derivative $G_{1I}^{(2k-1)}(x, \xi)$ should, however, have a jump if $x = \xi$:

$$\lim_{\varepsilon \to 0} \left[G_{1I}^{(2k-1)}(\xi + \varepsilon, \xi) - G_{1I}^{(2k-1)}(\xi - \varepsilon, \xi) \right] = \\ = \left[G_{1I}^{(2k-1)}(\xi + 0, \xi) - G_{1I}^{(2k-1)}(\xi - 0, \xi) \right] = \frac{1}{p_{2k}(\xi)} \quad . \tag{3.8b}$$

In contrast to this, $G_{2I}(x, \xi)$ and its derivatives

$$G_{2I}^{(n)}(x, \xi) = \frac{\partial^n G_{2I}(x, \xi)}{\partial x^n}, \qquad n = 1, 2, \ldots, 2k \tag{3.9}$$

are all continuous functions for any x in $[b, \ell]$.

3. Let ξ be fixed in $[b, \ell]$. The function $G_{1II}(x, \xi)$ and its derivatives

$$G_{1II}^{(n)}(x, \xi) = \frac{\partial^n G_{1II}(x, \xi)}{\partial x^n}, \qquad n = 1, 2, \ldots, 2k \tag{3.10}$$

are all continuous functions for any x in $[0, b]$.

4. Though the function $G_{2II}(x, \xi)$ and its derivatives

$$G_{2II}^{(n)}(x, \xi) = \frac{\partial^n G_{2II}(x, \xi)}{\partial x^n}, \qquad n = 1, 2, \ldots, 2k-2 \tag{3.11}$$

are also continuous for $x = \xi$:

$$\lim_{\varepsilon \to 0} \left[G_{2II}^{(n)}(\xi + \varepsilon, \xi) - G_{2II}^{(n)}(\xi - \varepsilon, \xi) \right] = \\ = \left[G_{2II}^{(n)}(\xi + 0, \xi) - G_{2II}^{(n)}(\xi - 0, \xi) \right] = 0 \quad n = 0, 1, 2, \ldots 2k-2 \tag{3.12a}$$

the derivative $G_{2II}^{(2k-1)}(x, \xi)$ should, however, have a jump if $x = \xi$:

$$\lim_{\varepsilon \to 0} \left[G_{2II}^{(2k-1)}(\xi + \varepsilon, \xi) - G_{21I}^{(2k-1)}(\xi - \varepsilon, \xi) \right] = \\ = \left[G_{2II}^{(2k-1)}(\xi + 0, \xi) - G_{2II}^{(2k-1)}(\xi - 0, \xi) \right] = \frac{1}{p_{2k}(\xi)} \quad . \tag{3.12b}$$

5. Let α be an arbitrary but finite non-zero constant. For a fixed $\xi \in [0,\ell]$ the product $G(x,\xi)\alpha$ as a function of x ($x \neq \xi$) should satisfy the homogeneous differential equation

$$M\left[G(x,\xi)\alpha\right] = 0\,.$$

6. The product $G(x,\xi)\alpha$ as a function of x should satisfy both the boundary conditions and the continuity conditions

$$\begin{gathered} U_{0r}[G] = \sum_{n=1}^{2k} \alpha_{nrI}\, G^{(n-1)}(0) = 0\,, \quad r = 1,\ldots,k \\ U_{br}[G] = \sum_{n=1}^{2k} \Big(\beta_{nrI}\, G^{(n-1)}(b-0) - \beta_{nrII}\, G^{(n-1)}(b+0)\Big) = 0\,, \quad r = 1,\ldots,2k \\ U_{\ell r}[G] = \sum_{n=1}^{2k} \gamma_{nrII}\, G^{(n-1)}(\ell) = 0\,, \quad r = 1,\ldots,k \end{gathered} \tag{3.13}$$

The above continuity conditions should be satisfied by the function pairs $G_{1I}(x,\xi)$, $G_{2I}(x,\xi)$ and $G_{1II}(x,\xi)$, $G_{2II}(x,\xi)$ as well.

Remark 1. It can be proved by utilizing the previous definition that integral (3.4) satisfies differential equation and boundary conditions (3.3) [15].

Remark 2. If the boundary value problem defined by (3.1) and (3.3) is self adjoint then the Green function is symmetric [15]:

$$G(x,\xi) = G(\xi,x) \tag{3.14}$$

It can be checked with ease utilizing the corresponding definition presented in [15] that the three-point boundary value problem defined by differential equation (2.6a) and the boundary and continuity condition given in Table 1 is self-adjoint.

3.2. **Calculation of the Green functions.**

3.2.1. *Introductory remarks.* Let us denote the linearly independent particular solutions of the homogeneous ordinary differential equation

$$L[y(x)] = 0 \tag{3.15}$$

by

$$y_1(x)\,, y_2(x)\,, y_3(x)\,, \ldots, y_{2k}(x)\,. \tag{3.16}$$

Since the general solution is a linear combination of the particular solutions it can be given in the following form:

$$y(x) = \sum_{n=1}^{2k} \mathcal{A}_n\, y_n(x) \tag{3.17}$$

where the coefficients $\mathcal{A}_n$ are arbitrary integration constants. The Green function should satisfy the homogeneous differential equation (3.15). Therefore it follows that it can be given as a linear combination of the particular solutions $y_n(x)$, i.e., by equation (3.17). It is a further problem how to find the coefficients $\mathcal{A}_n$. Subsections 3.3 and 3.4 deal with this issue.

3.3. **Calculation of the Green function if $\xi \in [0, b]$.** It is obvious that the integration constants $\mathcal{A}_n$ should be different in the two triangular domains $0 \le x \le \xi \le b$

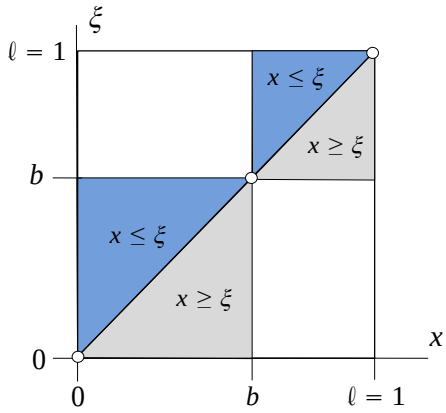

Figure 2.

and $0 \le \xi \le x \le b$. For this reason we shall apply the following assumptions:

(a)

$$G_{1I}(x,\xi) = \sum_{\ell=1}^{2k} \left(a_{\ell I}(\xi) + b_{\ell I}(\xi)\right) y_\ell(x)\,, \qquad x \le \xi\,;$$
$$G_{1I}(x,\xi) = \sum_{\ell=1}^{2k} \left(a_{\ell I}(\xi) - b_{\ell I}(\xi)\right) y_\ell(x)\,, \qquad x \ge \xi \qquad x \in [0,b] \tag{3.18}$$

and

(b)

$$G_{2I}(x,\xi) = \sum_{\ell=1}^{2k} c_{\ell I}(\xi) y_\ell(x)\,, \qquad x \in [b,\ell] \tag{3.19}$$

where the coefficients $a_{\ell I}(\xi)$, $b_{\ell I}(\xi)$ and $c_{\ell I}(\xi)$ are, in fact, unknown functions.

Note that the above representation for $G_{1I}(x,\xi)$ and $G_{2I}(x,\xi)$ ensures the fulfillment of Property 5 of the definition.

Continuity conditions (3.8a) yield the following equations

$$\sum_{\ell=1}^{2k} b_{\ell I}(\xi)\, y_\ell^{(n)}(\xi) = 0\,, \qquad n = 0,1,2,\ldots 2k-2 \tag{3.20a}$$

As regards the discontinuity condition (3.8b) we get

$$\frac{1}{p_{2k}(\xi)} = \left[G^{(2k-1)}(\xi+0,\xi) - G^{(2k-1)}(\xi-0,\xi)\right] = -2\sum_{\ell=1}^{k} b_{\ell I}(\xi)\, y_\ell^{(2k-1)}(\xi)\,.$$

Hence

$$\sum_{\ell=1}^{2k} b_{\ell I}(\xi)\, y_\ell^{(2k-1)}(\xi) = -\frac{1}{2p_{2k}(\xi)}\,. \tag{3.20b}$$

Fulfillment of equations (3.20a) and (3.20b) ensures the fulfillment of Properties 1, 2 and 4 of the definition.

Continuity and discontinuity conditions (3.8) result in the inhomogeneous linear system of equations (3.20) for the unknowns $b_\ell(\xi)$ ($\ell = 1, 2, \ldots, 2k$). Its determinant assumes the following form:

$$\begin{vmatrix} y_1(\xi) & y_2(\xi) & \ldots & y_k(\xi) \\ y_1^{(1)}(\xi) & y_2^{(1)}(\xi) & \ldots & y_k^{(1)}(\xi) \\ \ldots\ldots & \ldots\ldots & \ldots\ldots & \ldots\ldots \\ y_1^{(2k-1)}(\xi) & y_2^{(2k-1)}(\xi) & \ldots & y_{2k}^{(2k-1)}(\xi) \end{vmatrix}. \tag{3.21}$$

This determinant is the Wronskian[1] [16] of differential equation (3.15) which is not zero since the particular solutions $y_\ell(x)$ are linearly independent. This means that we can always find a unique solution for the coefficients $b_{\ell I}(\xi)$ in representation (3.18) of the Green function.

Utilizing the boundary and continuity conditions (3.13) the following equations can be obtained for the unknown coefficients $a_{\ell I}(\xi)$ and $c_{\ell I}(\xi)$:

$$U_{0r}[G] = \sum_{n=1}^{2k} \alpha_{nrI} \sum_{\ell=1}^{2k} \left(a_{\ell I}(\xi) + b_{\ell I}(\xi)\right) z_\ell(0)^{(n-1)} = 0 \qquad r = 1, 2, \ldots, k \tag{3.22a}$$

$$U_{br}[G] = \sum_{n=1}^{2k} \left(\beta_{nrI} \sum_{\ell=1}^{2k} \left(a_{\ell I}(\xi) - b_{\ell I}(\xi)\right) z_\ell(b)^{(n-1)} - \right.$$
$$\left. -\beta_{nrII} \sum_{\ell=1}^{2k} c_{\ell I}(\xi) z_\ell(b)^{(n-1)} \right) = 0\,, \qquad r = 1, 2, \ldots, 2k \tag{3.22b}$$

$$U_{cr}[G] = \sum_{n=1}^{2k} \gamma_{nrII} \sum_{\ell=1}^{2k} c_{\ell I}(\xi) z_\ell(c)^{(n-1)} = 0\,, \qquad r = 1, 2, \ldots, k \tag{3.22c}$$

or

$$\begin{aligned} \sum_{\ell=1}^{2k} a_{\ell I} U_{ar}[z_\ell] &= -\sum_{\ell=1}^{2k} b_{\ell I} U_{ar}[z_\ell] && r = 1, 2, \ldots, k \\ \sum_{\ell=1}^{2k} a_{\ell I} U_{brI}[z_\ell] - \sum_{\ell=1}^{2k} c_{\ell I} U_{brII}[z_\ell] &= \sum_{\ell=1}^{2k} b_{\ell I} U_{brI}[z_\ell] && r = 1, 2, \ldots, 2k \\ \sum_{\ell=1}^{2k} c_{\ell I} U_{cr}[z_\ell] &= 0 && r = 1, 2, \ldots, k \end{aligned} \tag{3.23}$$

[1] Józef Hoene-Wroński (1776-1853)

Solutions for $a_{\ell I}(\xi)$ and $c_{\ell I}(\xi)$ exist if and only if the determinant of the linear equation system (3.23) is different from zero. The linear independence of the boundary and continuity conditions assures in general that the equation system (3.23) is solvable.

Fulfillment of equations (3.23) ensures the fulfillment of Property 6 of the definition.

3.4. **Calculation of the Green function if $\xi \in [b, \ell = 1]$.** Now we shall assume that:

(a)

$$\begin{aligned} G_{1I}(x,\xi) &= \sum_{\ell=1}^{2k} \left(a_{\ell II}(\xi) + b_{\ell II}(\xi)\right) y_\ell(x)\,, \qquad x \le \xi\,; \\ & \qquad\qquad\qquad\qquad\qquad\qquad x \in [b, \ell = 1] \\ G_{1I}(x,\xi) &= \sum_{\ell=1}^{2k} \left(a_{\ell II}(\xi) - b_{\ell II}(\xi)\right) y_\ell(x)\,, \qquad x \ge \xi \end{aligned} \tag{3.24}$$

and

(b)

$$G_{2I}(x,\xi) = \sum_{\ell=1}^{2k} c_{\ell I}(\xi) y_\ell(x)\,, \qquad x \in [0, b] \tag{3.25}$$

where the coefficients $a_{\ell II}(\xi)$, $b_{\ell II}(\xi)$ and $c_{\ell II}(\xi)$ are again unknown functions.

Note that the above representation for $G_{1II}(x,\xi)$ and $G_{2II}(x,\xi)$ ensures the fulfillment of Property 5 of the definition.

Continuity conditions (3.12a) lead to the following equations:

$$\sum_{\ell=1}^{2k} b_{\ell II}(\xi)\, y_\ell^{(n)}(\xi) = 0\,, \qquad n = 0, 1, 2, \dots 2k-2 \tag{3.26a}$$

As regards discontinuity condition (3.12b) we obtain

$$\frac{1}{p_{2k}(\xi)} = \Big[G^{(2k-1)}(\xi+0,\xi) - G^{(2k-1)}(\xi-0,\xi)\Big] = -2\sum_{\ell=1}^{k} b_{\ell II}(\xi)\, y_\ell^{(2k-1)}(\xi)\,.$$

Hence

$$\sum_{\ell=1}^{2k} b_{\ell II}(\xi)\, y_\ell^{(2k-1)}(\xi) = -\frac{1}{2p_{2k}(\xi)}\,. \tag{3.26b}$$

Continuity and discontinuity conditions (3.12) yield the inhomogeneous linear system of equations (3.26) for the unknowns $b_{\ell II}(\xi)$ ($\ell = 1, 2, \dots, 2k$). Since these equation are formally the same as equations (3.20) it follows that their determinant is again the Wronskian (3.21) and this fact guarantees their solvability. It also follows that $b_{\ell II} = b_{\ell I}$.

Note that fulfillment of equations (3.26a) and (3.26b) ensures the fulfillment of Properties 1, 3 and 4 of the definition.

Utilizing now the boundary and continuity conditions (3.13) leads to the following linear equations for the unknown coefficients $a_{\ell II}(\xi)$ and $c_{\ell II}(\xi)$:

$$U_{0r}[G] = \sum_{n=1}^{2k} \alpha_{nrI} \sum_{\ell=1}^{2k} c_{\ell II}(\xi) z_\ell(a)^{(n-1)} = 0 \qquad r = 1, 2, \ldots, k \tag{3.27a}$$

$$U_{br}[G] = \sum_{n=1}^{2k} \left(\beta_{nrI} \sum_{\ell=1}^{2k} c_{\ell II}(\xi) z_\ell(b)^{(n-1)} - \right.$$
$$\left. -\beta_{nrII} \sum_{\ell=1}^{2k} \left(a_{\ell II}(\xi) + b_{\ell II}(\xi)\right) z_\ell(b)^{(n-1)} \right) = 0\,, \quad r = 1, 2, \ldots, 2k \tag{3.27b}$$

$$U_{\ell r}[G] = \sum_{n=1}^{2k} \gamma_{nrII} \sum_{\ell=1}^{2k} \left(a_{\ell II}(\xi) - b_{\ell II}(\xi)\right) z_\ell(c)^{(n-1)} = 0\,, \qquad r = 1, 2, \ldots, k \tag{3.27c}$$

or

$$\sum_{\ell=1}^{2k} a_{\ell II} U_{0r}[z_\ell] = 0 \qquad r = 1, 2, \ldots, k \tag{3.28a}$$

$$\sum_{\ell=1}^{2k} a_{\ell II} U_{brI}[z_\ell] - \sum_{\ell=1}^{2k} b_{\ell II} U_{brII}[z_\ell] = \sum_{\ell=1}^{2k} c_{\ell II} U_{brII}[z_\ell] \qquad r = 1, 2, \ldots, 2k \tag{3.28b}$$

$$\sum_{\ell=1}^{2k} b_{\ell II} U_{\ell r}[z_\ell] = \sum_{\ell=1}^{2k} c_{\ell II} U_{\ell r}[z_\ell] \qquad r = 1, 2, \ldots, k \tag{3.28c}$$

The linear equation system (3.27) is solvable for $a_{\ell II}(\xi)$ and $b_{\ell II}(\xi)$ if its determinant is different from zero. Since the boundary and continuity conditions are linearly independent equation system (3.27) is, in general, solvable.

If the determinants of the equation systems (3.23) and (3.28) are different from zero then there Green function exits which satisfies the properties of the definition given in Section 3.1.

Fulfillment of equations (3.28) ensures the fulfillment of Property 6 of the definition.

4. Calculation of the Green function for PrsP beams

4.1. **PrsP beams subjected to a compressive force.** If the axial force is compression it follows from equation (2.5) (or (2.6a)) that equilibrium problems of PrsP beams are governed by the differential equation

$$L[w(x)] = w^{(4)} + \mathcal{N} w^{(2)} = f_z \tag{4.1}$$

associated with the boundary and continuity conditions in Table 1.

4.1.1. *Green function if* $\xi \in [0, b]$. In the sequel we shall follow the line of thought presented in Subsection 3.3. Recalling that the general solution of the homogeneous differential equation $L[w(x)] = 0$ is given by (2.6b) the continuity and discontinuity conditions (3.20) result in the following equation system for $b_{\ell I}$:

$$\begin{bmatrix} 1 & \xi & \cos p\xi & \sin p\xi \\ 0 & 1 & -p\sin p\xi & p\cos p\xi \\ 0 & 0 & -p^2\cos p\xi & -p^2\sin p\xi \\ 0 & 0 & p^3\sin p\xi & -p^3\cos p\xi \end{bmatrix} \begin{bmatrix} b_1 \\ b_2 \\ b_3 \\ b_4 \end{bmatrix} = \begin{bmatrix} 0 \\ 0 \\ 0 \\ -\frac{1}{2} \end{bmatrix}, \tag{4.2}$$

REMARK 3. It has been taken into account here that $w(x)$ corresponds to $y(x)$, $k = 2$ and $p_{2k} = 1$.

Solution of this equation system assumes the following form:

$$\begin{bmatrix} b_{1I} \\ b_{2I} \\ b_{3I} \\ b_{4I} \end{bmatrix} = \frac{1}{2p^3} \begin{bmatrix} p\xi \\ -p \\ -\sin p\xi \\ \cos p\xi \end{bmatrix}. \tag{4.3}$$

We proceed with the boundary and continuity conditions (3.23). Recalling the boundary and continuity conditions in Table 1 and Remark 3. we obtain the following equation system:

(a) Boundary conditions at $x = 0$:

$$a_{1I}w_1(0) + a_{2I}w_2(0) + a_{3I}w_3(0) + a_{4I}w_4(0) = \\ = -b_{1I}w_1(0) - b_{2I}w_2(0) - b_{3I}w_3(0) - b_{4I}w_4(0)\,, \tag{4.4a}$$

$$a_{1I}w_1^{(2)}(0) + a_{2I}w_{2I}^{(2)}(0) + a_{3I}w_3^{(2)}(0) + a_{4I}w_4^{(2)}(0) = \\ = -b_{1I}w_1^{(2)}(0) - b_{2I}w_2^{(2)}(0) - b_{3I}w_3^{(2)}(0) - b_{4I}w_4^{(2)}(0)\,. \tag{4.4b}$$

(b) Continuity conditions at $x = b$:

$$a_{1I}w_1(b) + a_{2I}w_2(b) + a_{3I}w_3(b) + a_{4I}w_4(b) = \\ = b_{1I}w_1(b) + b_{2I}w_2(b) + b_{3I}w_3(b) + b_{4I}w_4(b)\,, \tag{4.5a}$$

$$c_{1I}w_1(b) + c_{2I}w_2(b) + c_{3I}w_3(b) + c_{4I}w_4(b) = 0\,, \tag{4.5b}$$

$$a_{1I}w_1^{(1)}(b) + a_{2I}w_{2I}^{(1)}(b) + a_{3I}w_3^{(1)}(b) + a_{4I}w_4^{(1)}(b) - \\ - c_{1I}w_1^{(1)}(b) - c_{2I}w_2^{(1)}(b) - c_{3I}w_3^{(1)}(b) - c_{4I}w_4^{(1)}(b) = \\ = b_{1I}w_1^{(1)}(b) + b_{2I}w_2^{(1)}(b) + b_{3I}w_3^{(1)}(b) + b_{4I}w_4^{(1)}(b)\,, \tag{4.5c}$$

$$a_{1I}w_1^{(2)}(b) + a_{2I}w_{2I}^{(2)}(b) + a_{3I}w_3^{(2)}(b) + a_{4I}w_4^{(2)}(b) - \\ - c_{1I}w_1^{(2)}(b) - c_{2I}w_2^{(2)}(b) - c_{3I}w_3^{(2)}(b) - c_{4I}w_4^{(2)}(b) = \\ = b_{1I}w_1^{(2)}(b) + b_{2I}w_2^{(2)}(b) + b_{3I}w_3^{(2)}(b) + b_{4I}w_4^{(2)}(b)\,. \tag{4.5d}$$

(c) Boundary conditions at $x = \ell$:

$$c_{1I}w_1(\ell) + c_{2I}w_2(\ell) + c_{3I}w_3(\ell) + c_{4I}w_4(\ell) = 0\,, \tag{4.6a}$$

$$c_{1I}w_1^{(2)}(\ell) + c_{2I}w_2^{(2)}(\ell) + c_{3I}w_3^{(2)}(\ell) + c_{4I}w_4^{(2)}(\ell) = 0\,. \tag{4.6b}$$

Using (2.6b) boundary conditions (4.4) at $x = 0$ yield

$$a_{1I} + a_{3I} = -b_{1I} - b_{3I}\,, \qquad a_{3I} = -b_{3I}\,.$$

Hence

$$a_{1I} = -b_{1I} = -\frac{1}{2p^2}\xi\,, \tag{4.7a}$$

$$a_{3I} = \frac{\sin p\xi}{2p^3}\,. \tag{4.7b}$$

As regards continuity conditions (4.5) at $x = b$ and boundary conditions (4.6) at $x = \ell$ substituting (2.6b) yields

$$\begin{bmatrix} b & \sin pb & 0 & 0 & 0 & 0 \\ 0 & 0 & 1 & b & \cos pb & \sin pb \\ 1 & p\cos pb & 0 & -1 & p\sin pb & -p\cos pb \\ 0 & -\sin pb & 0 & 0 & \cos pb & \sin pb \\ 0 & 0 & 1 & \ell & \cos p\ell & \sin p\ell \\ 0 & 0 & 0 & 0 & \cos p\ell & \sin p\ell \end{bmatrix} \begin{bmatrix} a_{2I} \\ a_{4I} \\ c_{1I} \\ c_{2I} \\ c_{3I} \\ c_{4i} \end{bmatrix} =$$

$$= \frac{1}{2p^3} \begin{bmatrix} 2p\xi - pb - \sin p\xi\cos pb - \sin p\,(\xi - b) \\ 0 \\ -p + 2p\sin p\xi\sin pb + p\cos p\xi\cos pb \\ 2\sin p\xi\cos pb - \cos p\xi\sin pb \\ 0 \\ 0 \end{bmatrix}$$

from where

$$\begin{aligned} a_{2I} = \\ = \frac{1}{2p^3\mathcal{D}_c}\,[&(p\,(\ell - b)\sin p\ell - \sin bp\sin p\,(\ell - b))\,(2p\xi - bp - \sin p\,(\xi - b) - \sin p\xi\cos bp) + \\ &- (\ell - b)\,(\sin bp\sin p\,(\ell - b))\,(-p + 2p\sin p\xi\sin bp + p\cos p\xi\cos bp) + \\ &+ (p\,(\ell - b)\sin bp\cos\,(p\ell - bp) - \sin bp\sin\,(p\ell - bp))\,(2\sin p\xi\cos bp - \cos p\xi\sin bp)]\,, \end{aligned} \tag{4.7c}$$

$$\begin{aligned} a_{4I} = \\ = \frac{1}{2p^3\mathcal{D}_c}\,[&- (\cos p\xi\sin pb - 2\sin p\xi\cos pb)\,(b\sin p\,(\ell - b) - pb\,(\ell - b)\cos p\,(\ell - b)) - \\ &+ (\ell - b)\,(\sin p\,(\ell - b))\,(\sin p\,(\xi - b) - 2p\xi + pb + \sin p\xi\cos pb) - \\ &- b\,(\ell - b)\sin p\,(\ell - b)\,(p - 2p\sin p\xi\sin pb - p\cos p\xi\cos pb)]\,, \end{aligned} \tag{4.7d}$$

$$c_{1I} = \frac{1}{2p^3\mathcal{D}_c}\left[-\ell\left(\sin p\left(\ell-b\right)\sin pb\right)\left(\sin p\left(\xi-b\right)-2p\xi+pb+\sin p\xi\cos pb\right)-\right.$$
$$+\ell\left(\sin p\left(\ell-b\right)\right)\left(pb\cos pb-\sin pb\right)\left(\cos p\xi\sin pb-2\sin p\xi\cos pb\right)+$$
$$\left.+b\ell\left(\sin p\left(\ell-b\right)\sin pb\right)\left(p-2p\sin p\xi\sin pb-p\cos p\xi\cos pb\right)\right], \quad (4.7e)$$

$$c_{2I} = \frac{1}{2p^3\mathcal{D}_c}\left[\left(\sin p\left(\ell-b\right)\sin pb\right)\left(\sin p\left(\xi-b\right)-2p\xi+pb+\sin p\xi\cos pb\right)+\right.$$
$$+\left(\sin p\left(\ell-b\right)\right)\left(\sin pb-pb\cos pb\right)\left(\cos p\xi\sin pb-2\sin p\xi\cos pb\right)+$$
$$\left.+b\left(\sin pb\sin p\left(\ell-b\right)\right)\left(p\cos p\xi\cos pb-p+2p\sin p\xi\sin pb\right)\right], \quad (4.7f)$$

$$c_{3I} = \frac{1}{2p^3\mathcal{D}_c}\left[\left(\ell-b\right)\left(\sin p\ell\sin pb\right)\left(\sin p\left(\xi-b\right)-2p\xi+pb+\sin p\xi\cos pb\right)-\right.$$
$$\left(\ell-b\right)\left(\sin p\ell\right)\left(\sin pb-pb\cos bp\right)\left(\cos p\xi\sin pb-2\sin p\xi\cos pb\right)+$$
$$\left.+b\left(\ell-b\right)\left(\sin pb\sin p\ell\right)\left(p\cos p\xi\cos pb-p+2p\sin p\xi\sin pb\right)\right], \quad (4.7g)$$

$$c_{4I} = \frac{1}{2p^3\mathcal{D}_c}\left[-\left(\ell-b\right)\cos p\ell\sin pb\left(\sin p\left(\xi-b\right)-2p\xi+pb+\sin p\xi\cos bp\right)+\right.$$
$$+\left(\ell-b\right)\cos p\ell\left(\sin pb-pb\cos pb\right)\left(\cos p\xi\sin pb-2\sin p\xi\cos pb\right)-$$
$$\left.-b\left(\ell-b\right)\left(\cos p\ell\sin pb\right)\left(p\cos p\xi\cos pb-p+2p\sin p\xi\sin pb\right)\right], \quad (4.7h)$$

in which

$$\mathcal{D}_c = pb\left(\ell-b\right)\sin p\ell-\ell\left(\sin pb\right)\sin p(\ell-b)\,. \quad (4.8)$$

With $a_{\ell I}$, $b_{\ell I}$ and $c_{\ell I}$

$$G(x,\xi) = \begin{cases} G_{1I}(x,\xi) = \sum_{\ell=1}^{4}\left(a_{\ell I}(\xi)\pm b_{\ell I}(\xi)\right)w_\ell(x) & \text{if } x\in[0,\ell]\,, \\ G_{2I}(x,\xi) = \sum_{\ell=1}^{4} c_{\ell I}(\xi)w_\ell(x) & \text{if } x\in[b,\ell]\,. \end{cases} \quad (4.9)$$

is the Green function if $\xi\in[0,b]$. The sign is positive if $x<\xi$ and negative if $x>\xi$.

4.1.2. *Green function if* $\xi\in[b,\ell]$. The equation system for $b_{\ell II}$ coincides with equation system (4.2). Hence $b_{\ell II}=b_{\ell I}$ and the solutions are given by equation (4.3).

The boundary conditions in Table 1 for $x=0$ yield:

$$c_{1II} = c_{3II} = 0\,.$$

The continuity conditions at $x=b$ and the boundary conditions at $x=\ell$ lead to the following equation system – details of the calculation are all omitted:

$$\begin{bmatrix} 0 & 0 & 0 & 0 & b & \sin pb \\ 1 & b & \cos pb & \sin pb & 0 & 0 \\ 0 & 1 & -p\sin pb & p\cos pb & -1 & -p\cos pb \\ 0 & 0 & -\cos pb & -\sin pb & 0 & \sin pb \\ 1 & \ell & \cos p\ell & \sin p\ell & 0 & 0 \\ 0 & 0 & -\cos p\ell & -\sin p\ell & 0 & 0 \end{bmatrix} \begin{bmatrix} a_{1II} \\ a_{2II} \\ a_{3II} \\ a_{4I} \\ c_{2II} \\ c_{4II} \end{bmatrix} =$$

$$= \frac{1}{2p^3} \begin{bmatrix} 0 \\ -p\xi + pb + \sin p\,(\xi - b) \\ p - p\cos p\,(\xi - b) \\ -\sin p\,(\xi - b) \\ p\xi - p\ell - \sin p\,(\xi - \ell) \\ \sin p\,(\xi - \ell) \end{bmatrix}.$$

The solutions needed for calculating the Green function are gathered here:

$$\begin{aligned} a_{1II} = \frac{1}{2p^3\mathcal{D}_c} \big[& (bp\ell \sin p\ell - \ell \sin p\,(\ell - b) \sin pb)\,(\sin p\,(\xi - b) - p\xi + pb) + \\ & + (\sin p\,(\ell - \xi))\left(pb^2 \sin p\ell - pb\ell \sin bp\right) - pb^2\,(\sin p\ell)\,(\sin p\,(\ell - \xi) - p\ell + p\xi) + \\ & + \ell\,(\sin p\,(\xi - b) \sin p\,(\ell - b))\,(\sin pb - pb\cos pb) + \\ & + b\ell\,(\sin p\,(\ell - b) \sin pb)\,(p - p\cos p\,(\xi - b))\big], \end{aligned} \tag{4.10a}$$

$$\begin{aligned} a_{2II} = \frac{1}{2p^3\mathcal{D}_c} \big[& \sin p\,(\ell - \xi)\,(\sin p\,(\ell - b) \sin pb - pb\,(\sin p\ell - \sin pb)) + \\ & + (\sin p\,(\ell - b) \sin pb - pb \sin p\ell)\,(\sin p\,(\xi - b) - p\xi + pb) + \\ & + (\sin p\,(\ell - b) \sin pb - pb \sin p\ell)\,(\sin p\,(\xi - \ell) - p\xi + p\ell) - \\ & - (\sin p\,(\xi - b) \sin p\,(\ell - b))\,(\sin pb - pb\cos pb) - \\ & - b\,(\sin p\,(\ell - b) \sin pb)\,(p - p\cos p\,(\xi - b))\big], \end{aligned} \tag{4.10b}$$

$$\begin{aligned} a_{3II} = \frac{1}{2p^3\mathcal{D}_c} \big[& -b\,(\sin p\ell \sin pb)\,(\sin p\,(\xi - b) - p\xi + pb) - \\ & - (\sin p\,(\ell - \xi) \sin pb)\,(b \sin p\ell - \ell \sin pb) + \\ & + b\,(\sin p\ell \sin pb)\,(\sin p\,(\ell - \xi) + p\xi - p\ell) - \\ & - (\sin p\,(\xi - b) \sin p\ell)\,(\sin pb - pb\cos pb)\,(\ell - b) - \\ & - b\,(\ell - b)\,(\sin p\ell \sin pb)\,(p - p\cos p\,(\xi - b))\big], \end{aligned} \tag{4.10c}$$

$$\begin{aligned} a_{4II} = \frac{1}{2p^3\mathcal{D}_c} \big[& \sin p\,(\ell - \xi)\,((\sin pb)\,(b\cos p\ell - \ell\cos pb) + pb\,(\ell - b)) + \\ & + b\,(\cos p\ell \sin pb)\,(\sin p\,(\xi - b) - p\xi + pb) + \\ & + b\,(\cos p\ell \sin pb)\,(\sin p\,(\xi - \ell) - p\xi + p\ell) + \\ & + (\sin p\,(\xi - b)\cos p\ell)\,(\sin pb - pb\cos pb)\,(\ell - b) + \\ & + b\,(\ell - b)\,(\cos p\ell \sin pb)\,(p - p\cos p\,(\xi - b))\big], \end{aligned} \tag{4.10d}$$

$$c_{1II} = 0\,, \tag{4.10e}$$

$$\begin{aligned} c_{2II} = \frac{1}{2p^3\mathcal{D}_c} \big[& -(\sin p\,(\xi - \ell))\,(\sin p\,(\ell - b) \sin pb - p\,(\ell - b) \sin pb) + \\ & - \sin p\,(\xi - b)\,(\sin p\,(\ell - b) \sin pb - p\,(\ell - b)\cos p\,(\ell - b) \sin bp) - \\ & + (\sin p\,(\ell - b) \sin pb)\,(\sin p\,(\xi - \ell) - p\xi + p\ell) + \end{aligned}$$

$$+ (\sin p\,(\ell - b) \sin pb)\,(\sin p\,(\xi - b) - p\xi + pb) + \\ + (\ell - b)\,(\sin p\,(\ell - b) \sin pb)\,(p - p \cos p\,(\xi - b))]\,, \quad (4.10f)$$

$$c_{3II} = 0\,, \quad (4.10g)$$

$$c_{4II} = \frac{1}{2p^3 \mathcal{D}_c} [-b\,(\sin p\,(\ell - b))\,(\sin p\,(\xi - b) - p\xi + pb) + \\ + \sin p\,(\xi - b)\,(b \sin p\,(\ell - b) - pb\,(\ell - b) \cos p\,(\ell - b)) + \\ + (\sin p\,(\xi - \ell))\,(b \sin p\,(\ell - b) - pb\,(\ell - b)) - \\ - b\,(\sin p\,(\ell - b))\,(\sin p\,(\xi - \ell) - p\xi + p\ell) - \\ - b\,(\ell - b)\,(\sin p\,(\ell - b))\,(p - p \cos p\,(\xi - b))]\,. \quad (4.10h)$$

With $a_{\ell II}$, $b_{\ell II}$ and $c_{\ell II}$

$$G(x,\xi) = \begin{cases} G_{1II}(x,\xi) = \sum_{\ell=1}^{4} c_{\ell I}(\xi) w_\ell(x) & \text{if } x \in [0,b]\,, \\ G_{2II}(x,\xi) = \sum_{\ell=1}^{4} \left(a_{\ell II}(\xi) \pm b_{\ell II}(\xi)\right) w_\ell(x) & \text{if } x \in [b,\ell]\,. \end{cases} \quad (4.11)$$

is the Green function if $\xi \in [b,\ell]$. The sign is positive if $x < \xi$ and negative if $x > \xi$.

The Green function given by equations (4.9) and (4.11) satisfies the symmetry condition $G(x,\xi) = G(\xi,x),\ x,\xi \in [0,\ell]$. Fulfillment of the symmetry condition was checked numerically for a number of point pairs x,ξ.

4.2. **PrsP beams subjected to a tensile force.** If the axial force is tensile equation according to equation (2.5) (or (2.6a)) equilibrium problems of PrsP beams are governed by the differential equation

$$L[w(x)] = w^{(4)} - \mathcal{N} w^{(2)} = f_z \quad (4.12)$$

for which the boundary and continuity conditions are presented in Table 1.

4.2.1. *Green function if* $\xi \in [0,b]$. In the present subsection we shall apply the solution steps detailed in Subsection 4.1.1. Recalling that the general solution of the homogeneous differential equation $L[w(x)] = 0$ is given by (2.6c) the continuity and discontinuity conditions (3.20) lead to the following equation system for $b_{\ell I}$:

$$\begin{bmatrix} 1 & \xi & \cosh p\xi & \sinh p\xi \\ 0 & 1 & p \sinh p\xi & p \cosh p\xi \\ 0 & 0 & p^2 \cosh p\xi & p^2 \sinh p\xi \\ 0 & 0 & p^3 \sinh p\xi & p^3 \cosh p\xi \end{bmatrix} \begin{bmatrix} b_1 \\ b_2 \\ b_3 \\ b_4 \end{bmatrix} = \begin{bmatrix} 0 \\ 0 \\ 0 \\ -\frac{1}{2} \end{bmatrix}, \quad (4.13)$$

from where

$$\begin{bmatrix} b_{1I} \\ b_{2I} \\ b_{3I} \\ b_{4I} \end{bmatrix} = \frac{1}{2p^3} \begin{bmatrix} -p\xi \\ p \\ \sinh p\xi \\ -\cosh p\xi \end{bmatrix}. \quad (4.14)$$

Remark 4. It has been taken again into account in the calculations that $w(x)$ corresponds to $y(x)$, $k = 2$ and $p_{2k} = 1$.

We proceed with boundary and continuity conditions (3.23). Recalling the boundary and continuity conditions in Table 1 and Remark 4. the equation system we obtain is formally the same as the equation system given by (4.4), (4.5) and (4.6) – the solution for w is, however, different – see (2.6c). After substituting it we have

$$a_{1I} = -b_{1I} = \frac{1}{2p^3} p\xi\,,$$
$$a_{3I} = -b_{3I} = -\frac{1}{2p^3}\sinh p\xi$$

and

$$\begin{bmatrix} b & \sinh pb & 0 & 0 & 0 & 0 \\ 0 & 0 & 1 & b & \cosh pb & \sinh pb \\ 1 & p\cosh pb & 0 & -1 & -p\sinh pb & -p\cosh pb \\ 0 & \sinh pb & 0 & 0 & -\cosh pb & -\sinh pb \\ 0 & 0 & 1 & \ell & \cosh p\ell & \sinh p\ell \\ 0 & 0 & 0 & 0 & \cosh p\ell & \sinh p\ell \end{bmatrix} \begin{bmatrix} a_{2I} \\ a_{4I} \\ c_{1I} \\ c_{2I} \\ c_{3I} \\ c_{4i} \end{bmatrix} =$$
$$= \frac{1}{2p^3} \begin{bmatrix} -2p\xi + pb + \sinh(p\xi - bp) + \sinh p\xi \cosh pb \\ 0 \\ p + 2p\sinh p\xi \sinh pb - p\cosh p\xi \cosh pb \\ 2\sinh p\xi \cos pb - \cosh p\xi \sinh pb \\ 0 \\ 0 \end{bmatrix}$$

from where

$$a_{2I} = \frac{1}{2p^3\mathcal{D}_t} \times$$
$$[(p(\ell - b)\sinh p\ell - \sinh pb \sinh p(\ell - b))(pb - 2p\xi + \sinh p(\xi - b) + \sinh p\xi \cosh pb) -$$
$$-(\ell - b)\sinh pb \sinh p(\ell - b)(p + 2p\sinh p\xi \sinh pb - p\cosh p\xi \cosh pb) -$$
$$-(p(\ell - b)\sinh pb \cosh p(\ell - b) - \sinh pb \sinh p(\ell - b)) \times$$
$$(2\sinh p\xi \cos pb - \cosh p\xi \sinh pb)]\,, \quad (4.15a)$$

$$a_{4I} =$$
$$= \frac{1}{2p^3\mathcal{D}_t} [-(\cosh p\xi \sinh pb - 2\sinh p\xi \cos pb)(b\sinh p(\ell - b) + pb(\ell - b)\cosh p(\ell - b)) +$$
$$-(\ell - b)(\sinh p(\ell - b))(\sinh p(\xi - b) - 2p\xi + pb + \sinh p\xi \cosh pb) +$$
$$+b(\ell - b)(\sinh p(\ell - b))(p + 2p\sinh p\xi \sinh pb - p\cosh p\xi \cosh pb)]\,, \quad (4.15b)$$

$$c_{1I} = \frac{1}{2p^3\mathcal{D}_t} [\ell(\sinh p(\ell - b)\sinh pb)(\sinh p(\xi - b) - 2p\xi + pb + \sinh p\xi \cosh pb) -$$
$$-\ell(\sinh p(\ell - b))(pb\cosh pb - \sinh pb)(\cosh p\xi \sinh pb - 2\sinh p\xi \cos pb) +$$
$$-b\ell(\sinh p(\ell - b)\sinh pb)(p + 2p\sinh p\xi \sinh pb - p\cosh p\xi \cosh pb)]\,, \quad (4.15c)$$

$$c_{2I} = \frac{1}{2p^3\mathcal{D}_t}\left[-\left(\sinh p\left(\ell-b\right)\sinh pb\right)\left(\sinh p\left(\xi-b\right)-2p\xi+pb+\sinh p\xi\cosh pb\right)+\right.$$
$$-\sinh p\left(\ell-b\right)\left(\sinh pb-pb\cosh pb\right)\left(\cosh p\xi\sinh pb-2\sinh p\xi\cos pb\right)-$$
$$\left.-b\left(\sinh pb\sinh p\left(\ell-b\right)\right)\left(p\cosh p\xi\cosh pb-p-2p\sinh p\xi\sinh pb\right)\right], \quad (4.15d)$$

$$c_{3I} = \frac{1}{2p^3\mathcal{D}_t}\left[-\left(\ell-b\right)\left(\sinh p\ell\sinh pb\right)\left(\sinh p\left(\xi-b\right)-2p\xi+pb+\sinh p\xi\cosh pb\right)+\right.$$
$$-\left(\ell-b\right)\left(\sinh p\ell\right)\left(\sinh pb-pb\cosh pb\right)\left(\cosh p\xi\sinh pb-2\sinh p\xi\cos pb\right)$$
$$\left.-b\left(\ell-b\right)\left(\sinh pb\sinh p\ell\right)\left(p\cosh p\xi\cosh pb-p-2p\sinh p\xi\sinh pb\right)\right], \quad (4.15e)$$

$$c_{4I} = \frac{1}{2p^3\mathcal{D}}\left[\left(\ell-b\right)\left(\cosh p\ell\sinh pb\right)\left(\sinh p\left(\xi-b\right)-2p\xi+pb+\sinh p\xi\cosh pb\right)+\right.$$
$$+\left(\ell-b\right)\cosh p\ell\left(\sinh pb-pb\cosh pb\right)\left(\cosh p\xi\sinh pb-2\sinh p\xi\cos pb\right)+$$
$$\left.+b\left(\ell-b\right)\left(\cosh p\ell\sinh pb\right)\left(p\cosh p\xi\cosh pb-p-2p\sinh p\xi\sinh pb\right)\right] \quad (4.15f)$$

in which

$$\mathcal{D}_t = bp\left(\ell-b\right)\sinh p\ell-\ell\sinh bp\sinh p\left(\ell-b\right). \quad (4.16)$$

With $a_{\ell I}$, $b_{\ell I}$ and $c_{\ell I}$ derived above for the case of the tensile axial force equation (4.9) can be used to find the Green function if $\xi\in[0,b]$.

4.2.2. *Green function if* $\xi\in[b,\ell]$. The equation system for $b_{\ell II}$ coincides formally with equation system (4.13). Consequently, $b_{\ell II}=b_{\ell I}$ and the solutions are given by equation (4.14).

The boundary conditions in Table 1 for $x=0$ yield:

$$c_{1II}=c_{3II}=0$$

The continuity conditions at $x=b$ and the boundary conditions at $x=\ell$ lead to the following equation system – details of the calculation are all omitted:

$$\begin{bmatrix} 0 & 0 & 0 & 0 & b & \sinh pb \\ 1 & b & \cosh pb & \sinh pb & 0 & 0 \\ 0 & 1 & p\sinh pb & p\cosh pb & -1 & -p\cosh pb \\ 0 & 0 & \cosh pb & \sinh pb & 0 & -\sinh pb \\ 1 & \ell & \cosh p\ell & \sinh p\ell & 0 & 0 \\ 0 & 0 & \cosh p\ell & \sinh p\ell & 0 & 0 \end{bmatrix}\begin{bmatrix} a_{1II} \\ a_{2II} \\ a_{3II} \\ a_{4I} \\ c_{2II} \\ c_{4II} \end{bmatrix} =$$
$$= \frac{1}{2p^3}\begin{bmatrix} 0 \\ p\xi-pb-\sinh p\left(\xi-b\right) \\ -p+p\cosh p\left(\xi-b\right) \\ -\sinh p\left(\xi-b\right) \\ -p\xi+p\ell+\sinh p\left(\xi-\ell\right) \\ \sinh p\left(\xi-\ell\right) \end{bmatrix}$$

The solutions obtained for $a_{1II},\ldots,a_{4II}$ and $c_{1II},\ldots,c_{4II}$ and needed for calculating the Green function are presented here:

$$a_{1II} = \frac{1}{2p^3\mathcal{D}_t}\left[(pb\ell\sinh p\ell - \ell\sinh pb\sinh p(\ell-b))(-\sinh p(\xi-b) + p\xi - pb) + \right.$$
$$+ (\sinh p(\xi-\ell))\left(pb^2\sinh p\ell - pb\ell\sinh pb\right) - pb^2(\sinh p\ell)(\sinh p(\xi-\ell) + p\ell - p\xi) -$$
$$- \ell(\sinh p(\xi-b)\sinh p(\ell-b))(\sinh pb - pb\cosh pb) -$$
$$\left. -b\ell(\sinh p(\ell-b)\sinh pb)(p - p\cosh p(\xi-b))\right], \quad (4.17a)$$

$$a_{2II} = \frac{1}{2p^3\mathcal{D}}\left[-\sinh p(\ell-\xi)(\sinh p(\ell-b)\sinh pb + pb(-\sinh p\ell + \sinh pb)) + \right.$$
$$+ (\sinh p(\ell-b)\sinh pb - pb\sinh p\ell)(-\sinh p(\xi-b) + p\xi - pb) -$$
$$- (\sinh p(\ell-b)\sinh pb - pb\sinh p\ell)(\sinh p(\xi-\ell) + p\ell - p\xi) +$$
$$+ (\sinh p(\xi-b)\sinh p(\ell-b))(\sinh pb - pb\cosh pb) +$$
$$\left. +b(\sinh pb\sinh p(\ell-b))(p - p\cosh p(\xi-b))\right], \quad (4.17b)$$

$$a_{3II} = \frac{1}{2p^3\mathcal{D}_t}\left[b(\sinh p\ell\sinh pb)(\sinh p(\xi-b) - p\xi + pb) - \right.$$
$$- (\sinh p(\ell-\xi)\sinh pb)(b\sinh p\ell - \ell\sinh pb) -$$
$$- b(\sinh p\ell\sinh pb)(\sinh p(\ell-\xi) + p\xi - p\ell) -$$
$$- (\sinh p(\xi-b)\sinh p\ell)(\sinh pb - pb\cosh pb)(\ell-b) -$$
$$\left. -b(\ell-b)(\sinh p\ell\sinh pb)(p - p\cosh p(\xi-b))\right], \quad (4.17c)$$

$$a_{4II} = \frac{1}{2p^3\mathcal{D}_t}\left[-\sinh p(\ell-\xi)((\sinh pb)(b\cosh p\ell - \ell\cosh pb) + pb(\ell-b)) - \right.$$
$$- b(\cosh p\ell\sinh pb)(\sinh p(\xi-b) - p\xi + pb) -$$
$$- b(\cosh p\ell\sinh pb)(\sinh p(\xi-\ell) - p\xi + p\ell) -$$
$$- (\sinh p(\xi-b)\cosh p\ell)(\sinh pb - pb\cosh pb)(\ell-b) -$$
$$\left. -b(\ell-b)(\cosh p\ell\sinh pb)(p - p\cosh p(\xi-b))\right], \quad (4.17d)$$

$$c_{1II} = 0, \quad (4.17e)$$

$$c_{2II} = \frac{1}{2p^3\mathcal{D}_t}\left[(\sinh p(\xi-\ell))(\sinh pb\sinh p(\ell-b) - p(\ell-b)\sinh pb) + \right.$$
$$+ \sinh p(\xi-b)(\sinh p(\ell-b)\sinh pb - p(\ell-b)\sinh pb\cosh p(\ell-b)) -$$
$$- (\sinh p(\ell-b)\sinh pb)(\sinh p(\xi-\ell) - p\xi + p\ell) -$$
$$- (\sinh p(\ell-b)\sinh pb)(\sinh p(\xi-b) - p\xi + pb) +$$
$$\left. - (\ell-b)(\sinh p(\ell-b)\sinh pb)(p - p\cosh p(\xi-b))\right], \quad (4.17f)$$

$$c_{3II} = 0, \quad (4.17g)$$

$$c_{4II} = \frac{1}{2p^3\mathcal{D}}\left[b\sinh p(\ell-b)(\sinh p(\xi-b) - p\xi + pb) - \right.$$
$$- \sinh p(\xi-b)(b\sinh p(\ell-b) - pb(\ell-b)\cosh p(\ell-b)) -$$

$$- (\sinh p\,(\xi - \ell))\,(b \sinh p\,(\ell - b) - pb\,(\ell - b)) +$$
$$+ b\,(\sinh p\,(\ell - b))\,(\sinh p\,(\xi - \ell) - p\xi + p\ell) +$$
$$+ b\,(\ell - b)\,(\sinh p\,(\ell - b))\,(p - p\cosh p\,(\xi - b))] \,. \quad (4.17h)$$

With $a_{\ell II}$, $b_{\ell II} = b_{\ell I}$ and $c_{\ell I}$ presented above for the tensile axial force equation (4.11) can be used to find the Green function if $\xi \in [0, b]$. According to a numerical check the Green function satisfies the symmetry condition $G(x, \xi) = G(\xi, x)$.

4.2.3. *Graphical representation of the Green function.* The dimensionless critical force $\mathcal{N}_{\rm crit}$ ($p_{\rm crit}$) as function of the location of the intermediate roller support is given by the polynomial [17]:

$$\sqrt{\mathcal{N}_{\rm crit}}/\pi = p_{\rm crit}/\pi =$$
$$= -25.651\,118\,291\,1b^5 + 18.328\,978\,830\,0b^4 - 4.701\,184\,038\,74b^3 +$$
$$+ 1.395\,339\,140\,36b^2 + 0.928\,843\,353\,123b + 1.430\,503\,352\,36\,, \quad b \in [0, 0.5]. \quad (4.18)$$

Note that for symmetry reasons $b \in [0, 0.5]$.

Assume that $b = 0.5$ and $\xi = 0.75$. Assume further that the axial force is compressive. Figure 3 shows the Green function provided that $p = 0.4p_{\rm crit}$ and $p = 0.8p_{\rm crit}$. Since the Green function is the dimensionless vertical displacement due to a dimensionless unit force applied to the beam at $\xi = 0.75$ it follows that the bending moment caused by the compressive force $\mathcal{N}$ has the same sign as the bending moment caused by the dimensionless unit force. Its magnitude increases with $\mathcal{N}$. The same is valid for the magnitude of the Green function. Figure 3 clearly shows this change.

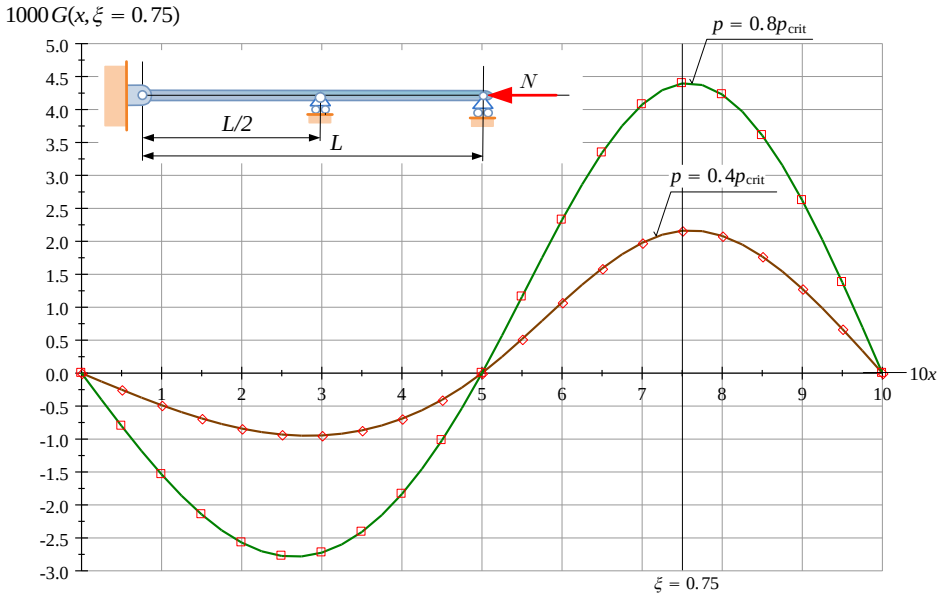

Figure 3.

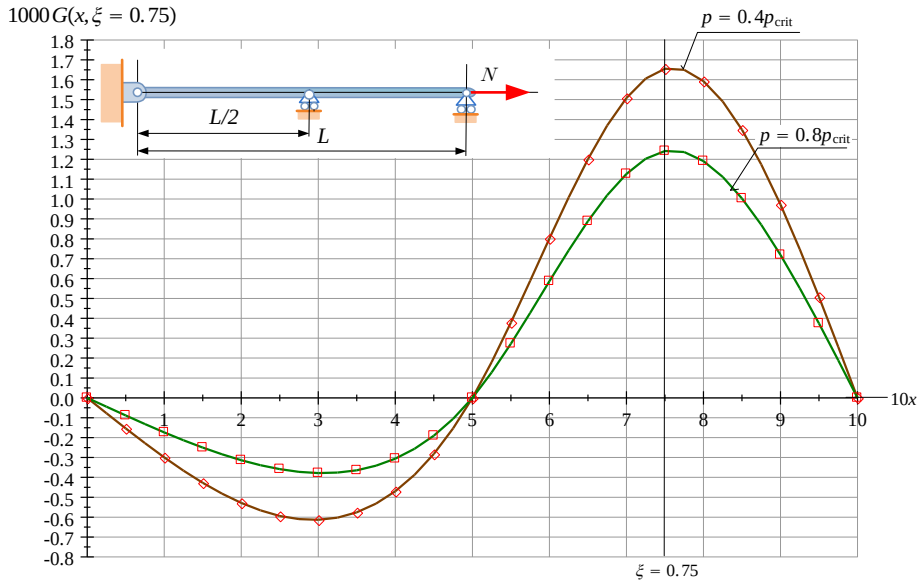

Figure 4.

Assume again that $b = 0.5$ and $\xi = 0.75$ but the axial force is tensile. Figure 4 shows the Green function provided that $p = 0.4p_{\text{crit}}$ and $p = 0.8p_{\text{crit}}$. This time there is a sign difference between the bending moments due to the dimensionless unit force and the tensile force. Hence the magnitude of the Green function decreases as the axial force $\mathcal{N}$ increases. Figure 4 clearly represents this phenomenon.

According to equation (3.4) the dimensionless vertical displacement w due to the dimensionless vertical force system f_z can be calculated by performing the integral in

$$w(x) = \int_{\xi=0}^{\ell=1} G(x,\xi) f_z(\xi)\,\mathrm{d}\xi\,. \tag{4.19}$$

5. Computational results

5.1. **Integral equation of the problem.** We shall assume that the inertia forces resulting from the longitudinal motion in the axial direction are neglected. It is also assumed that the moments of the inertia forces obtained from the rotation of cross section are negligible. Under these assumptions the dimensionless amplitude of the vibrations is denoted by w. It can be seen on the basis of Subsection 8.16 in [18], (4.1) and (4.12) that the amplitude w should fulfill the differential equation

$$\begin{aligned} L[w(x)] &= w^{(4)} \pm \mathcal{N} w^{(2)} = \lambda w = f_z\,, \\ p^2 &= \mathcal{N} = \frac{L^2 N}{I_{ey}}, \qquad \lambda = \frac{\rho_a A \omega^2 L^4}{I_{ey}}, \end{aligned} \tag{5.1}$$

where ρ_a is the average density over the cross section of the beam, ω is the natural circular frequency while λ is the eigenvalue sought. Differential equation (5.1) is

associated with the homogeneous boundary and continuity conditions presented in Table 1. These constitute an eigenvalue problem with λ as the eigenvalue. If we substitute $\lambda w(\xi)$ for $f_z(\xi)$ in (4.19) we obtain the homogeneous Fredholm integral equation

$$w(x) = \lambda \int_{\xi=0}^{\ell=1} G(x,\xi) w(\xi)\, \mathrm{d}\xi \tag{5.2}$$

for which the kernel $G(x,\xi)$ is presented in Subsection 4.1 if the axial force is compressive and in Subsection 4.2 if the axial force is tensile. The above integral equation determines an eigenvalue problem equivalent to the eigenvalue problem determined by differential equation (5.1) and the homogeneous boundary and continuity conditions presented in Table 1. Making use of the boundary element algorithm presented in [15] – see Subsection 7.2 – the eigenvalue problem determined by (5.2) can be reduced to an algebraic eigenvalue problem which can be solved numerically. A Fortran 90 code has been developed and applied to find numerical solutions for the eigenvalue λ. The interval $[0, \ell = 1]$ was divided into 12 elements and a quadratic isoparametric approximation was used over the elements in the code we developed.

If the axial force is zero the lowest dimensionless eigenvalue and circular frequency will be denoted by $\breve{\lambda}_1$ and $\breve{\omega}_1$.

5.2. **Numerical results if b tends to zero.** Table 2 represents the computational results if $b \longrightarrow 0$. The quotient $\sqrt{\mathcal{N}_{\mathrm{crit}}}/\pi$ is computed using equation (4.18). The value of $\breve{\lambda}_1$ is given by equation (105) in [15]:

$$\begin{aligned}\sqrt{\breve{\lambda}_1}/\pi^2 = {} & 402.66423 \times (1.0-b)^5 - 1594.73367 \times (1.0-b)^4 + \\ & + 2494.995 \times (1.0-b)^3 - 1918.4007 \times (1.0-b)^2 + \\ & + 716.4361 \times (1.0-b) - 99.3904, \quad b \in [0, 0.5],\end{aligned} \tag{5.3}$$

or can be taken from Table 2 in [15]. This is also valid for Tables 3,...,7 which have the same structure as Table 2. The quotient $\omega_1^2/\breve{\omega}_1^2 = \lambda_1/\breve{\lambda}_1$ is computed for $\mathcal{N}/\mathcal{N}_{\mathrm{crit}} = 0.00, 0.10, \ldots, 0.90$ – see columns 2, 3 and 5 in Tables 2,...,7.

The computed values of $\omega_1^2/\breve{\omega}_1^2 = \lambda_1/\breve{\lambda}_1$ are denoted by diamonds in Figures 5,...,9. The difference between two subsequent values of $\omega_1^2/\breve{\omega}_1^2$ is also included in these tables – see columns 4 and 6. If the function $\omega_1^2/\breve{\omega}_1^2(\mathcal{N}/\mathcal{N}_{\mathrm{crit}})$ is [non-linear](linear) the difference [varies](is constant).

Quadratic polynomials are fitted onto the computational results. Their graphs are drawn using continuous lines in the figures.

The beam behaves as if it were a fixed-pinned beam if $b \longrightarrow 0$. Hence the results obtained should be the same as those valid for fixed-pinned beams. A comparison of the present results to those published in [18] – see Section 8.17.2 – proves that there is a very good agreement.

Table 2.

		b tends to zero			
		$\sqrt{\mathcal{N}_{\text{crit}}}/\pi = 1.4304$, $\check{\lambda}_1 = 1.5622$			
		Compression		Tension	
Load step	$\mathcal{N}/\mathcal{N}_{\text{crit}}$ (p^2/p^2_{crit})	$\omega_1^2/\check{\omega}_1^2$ $(\lambda_1/\check{\lambda}_1)$	Difference	$\omega_1^2/\check{\omega}_1^2$ $(\lambda_1/\check{\lambda}_1)$	Difference
1	0.00	1.000000		1.000000	
2	0.10	0.902010	0.0979900	1.097670	0.097670
3	0.20	0.803642	-0.098369	1.195005	0.097335
4	0.30	0.704879	-0.098763	1.292038	0.097032
5	0.40	0.605692	-0.099186	1.388785	0.096747
6	0.50	0.506050	-0.099642	1.485264	0.096478
7	0.60	0.405916	-0.100134	1.581488	0.096224
8	0.70	0.305247	-0.100668	1.677471	0.095983
9	0.80	0.203999	-0.101248	1.773227	0.095755
10	0.90	0.102117	-0.101881	1.868766	0.095538

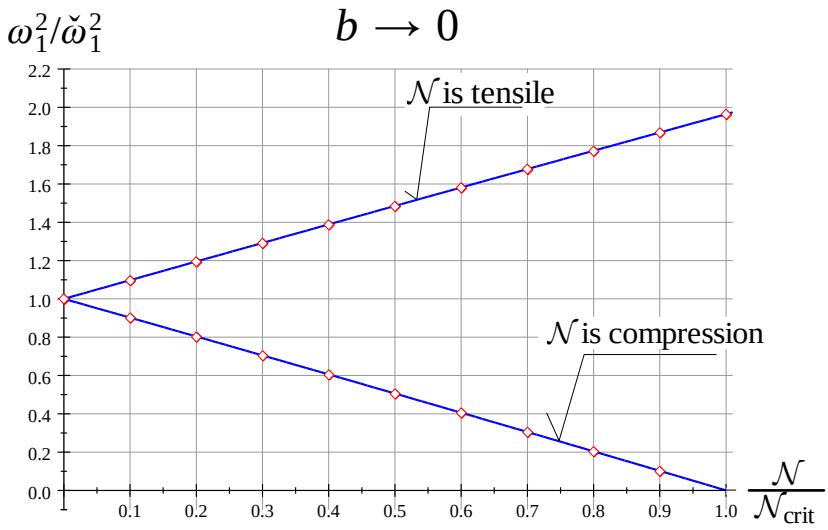

Figure 5.

The quadratic polynomials fitted onto the computational results both for compression and tension are given by the following equations:

$$\frac{\omega_1^2}{\check{\omega}_1^2} = \frac{\lambda_1}{\check{\lambda}_1} = 0.9999 - 0.9756\frac{\mathcal{N}}{\mathcal{N}_{\text{crit}}} - 2.4061 \times 10^{-2}\left(\frac{\mathcal{N}}{\mathcal{N}_{\text{crit}}}\right)^2, \tag{5.4a}$$

$$\frac{\omega_1^2}{\check{\omega}_1^2} = \frac{\lambda_1}{\check{\lambda}_1} = 1.0000 + 0.9770\frac{\mathcal{N}}{\mathcal{N}_{\text{crit}}} - 1.3205 \times 10^{-2}\left(\frac{\mathcal{N}}{\mathcal{N}_{\text{crit}}}\right)^2 \tag{5.4b}$$

5.3. **Numerical results if** $b = 0.1$**.** Table 3 and Figure 6 represent the results obtained.

Table 3.

		$b = 0.1$			
		$\sqrt{\mathcal{N}_{\text{crit}}}/\pi = 1.5341$, $\check{\lambda}_1 = 1.8098$			
		Compression		Tension	
Load step	$\mathcal{N}/\mathcal{N}_{\text{crit}}$ (p^2/p^2_{crit})	$\omega_1^2/\check{\omega}_1^2$ $(\lambda_1/\check{\lambda}_1)$	Difference	$\omega_1^2/\check{\omega}_1^2$ $(\lambda_1/\check{\lambda}_1)$	Difference
1	0.00	1.000000		1.000000	
2	0.10	0.898254	-0.098720	1.093780	0.093780
3	0.20	0.800038	-0.098215	1.191130	0.097350
4	0.30	0.701491	-0.098547	1.288230	0.097099
5	0.40	0.602586	-0.098905	1.385094	0.096863
6	0.50	0.503293	-0.099292	1.481736	0.096642
7	0.60	0.403580	-0.099712	1.578170	0.096434
8	0.70	0.303411	-0.100169	1.674408	0.096237
9	0.80	0.202743	-0.100667	1.770460	0.096051
10	0.90	0.101529	-0.101214	1.866336	0.095876

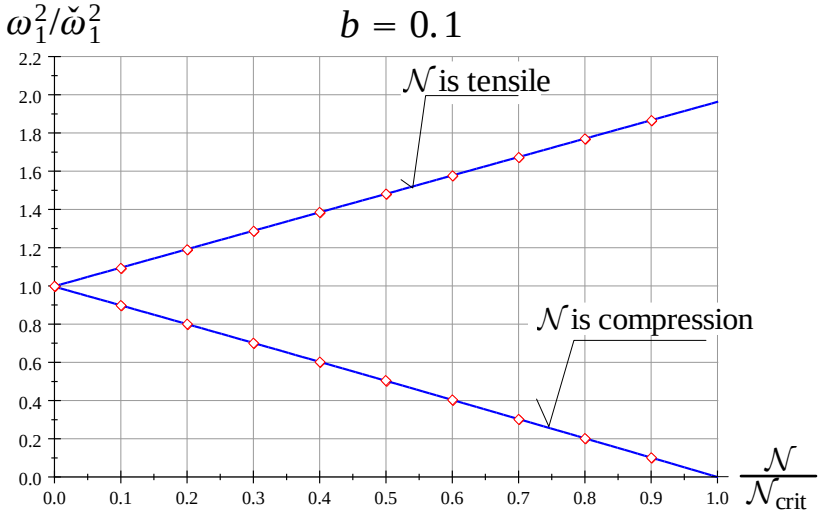

Figure 6.

The quadratic polynomials fitted onto the numerical results are as follows:

$$\frac{\omega_1^2}{\check{\omega}_1^2} = \frac{\lambda_1}{\check{\lambda}_1} = 0.998\,400 - 0.985\,245\,\frac{\mathcal{N}}{\mathcal{N}_{\text{crit}}} - 1.174\,606 \times 10^{-2}\left(\frac{\mathcal{N}}{\mathcal{N}_{\text{crit}}}\right)^2, \tag{5.5a}$$

$$\frac{\omega_1^2}{\check{\omega}_1^2} = \frac{\lambda_1}{\check{\lambda}_1} = 0.998\,592 + 0.966\,543\,\frac{\mathcal{N}}{\mathcal{N}_{\text{crit}}} - 2.109\,042 \times 10^{-3}\left(\frac{\mathcal{N}}{\mathcal{N}_{\text{crit}}}\right)^2. \tag{5.5b}$$

5.4. **Numerical results if** $b = 0.2$**.** Table 4 and Figure 6 represent the results obtained.

Table 4.

		$b = 0.2$			
		$\sqrt{\mathcal{N}_{\text{crit}}}/\pi = 1.6557$, $\check{\lambda}_1 = 2.1610$			
		Compression		Tension	
Load step	$\mathcal{N}/\mathcal{N}_{\text{crit}}$ (p^2/p^2_{crit})	$\omega_1^2/\check{\omega}_1^2$ $(\lambda_1/\check{\lambda}_1)$	Difference	$\omega_1^2/\check{\omega}_1^2$ $(\lambda_1/\check{\lambda}_1)$	Difference
1	0.00	1.000000		1.000000	
2	0.10	0.904873	-0.099724	1.104529	0.099631
3	0.20	0.804869	-0.100004	1.204192	0.099662
4	0.30	0.704740	-0.100128	1.303750	0.099558
5	0.40	0.604481	-0.100259	1.403208	0.099458
6	0.50	0.504084	-0.100396	1.502570	0.099362
7	0.60	0.403543	-0.100541	1.601840	0.099269
8	0.70	0.302849	-0.100693	1.701020	0.099180
9	0.80	0.201995	-0.100854	1.800115	0.099094
10	0.90	0.100970	-0.101025	1.899127	0.099011

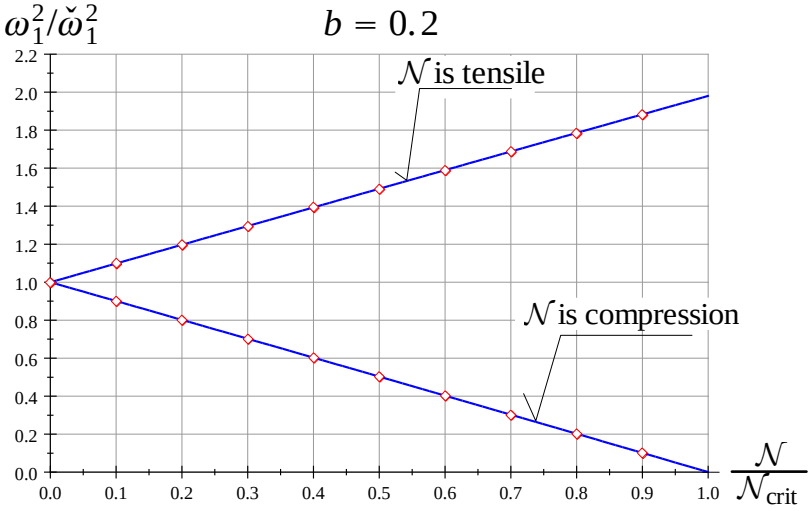

Figure 7.

Equations

$$\frac{\omega_1^2}{\check{\omega}_1^2} = \frac{\lambda_1}{\check{\lambda}_1} = 0.999\,596 - 0.987\,083\,\frac{\mathcal{N}}{\mathcal{N}_{\text{crit}}} - 1.214\,649 \times 10^{-2}\left(\frac{\mathcal{N}}{\mathcal{N}_{\text{crit}}}\right)^2, \tag{5.6a}$$

$$\frac{\omega_1^2}{\check{\omega}_1^2} = \frac{\lambda_1}{\check{\lambda}_1} = 0.999\,633 + 0.987\,212\,\frac{\mathcal{N}}{\mathcal{N}_{\text{crit}}} - 6.295\,185 \times 10^{-3}\left(\frac{\mathcal{N}}{\mathcal{N}_{\text{crit}}}\right)^2. \tag{5.6b}$$

are the quadratic polynomials fitted onto the computational results.

5.5. **Numerical results if $b = 0.3$.** Table 5, Figure 8 and equations (5.7) represent the results obtained.

Table 5.

		$b = 0.3$			
		$\sqrt{\mathcal{N}_{\text{crit}}}/\pi = 1.79382$, $\check{\lambda}_1 = 2.6683$			
		Compression		Tension	
Load step	$\mathcal{N}/\mathcal{N}_{\text{crit}}$ (p^2/p^2_{crit})	$\omega_1^2/\check{\omega}_1^2$ $(\lambda_1/\check{\lambda}_1)$	Difference	$\omega_1^2/\check{\omega}_1^2$ $(\lambda_1/\check{\lambda}_1)$	Difference
1	0.00	1.000000		1.000000	
2	0.10	0.900657	-0.099075	1.098279	0.098279
3	0.20	0.801574	-0.099083	1.196842	0.098563
4	0.30	0.702290	-0.099283	1.295255	0.098412
5	0.40	0.602790	-0.099500	1.393526	0.098271
6	0.50	0.503055	-0.099734	1.491664	0.098138
7	0.60	0.403065	-0.099990	1.589678	0.098013
8	0.70	0.302795	-0.100269	1.687574	0.097895
9	0.80	0.202221	-0.100574	1.785359	0.097784
9	0.90	0.101311	-0.100910	1.883038	0.097679

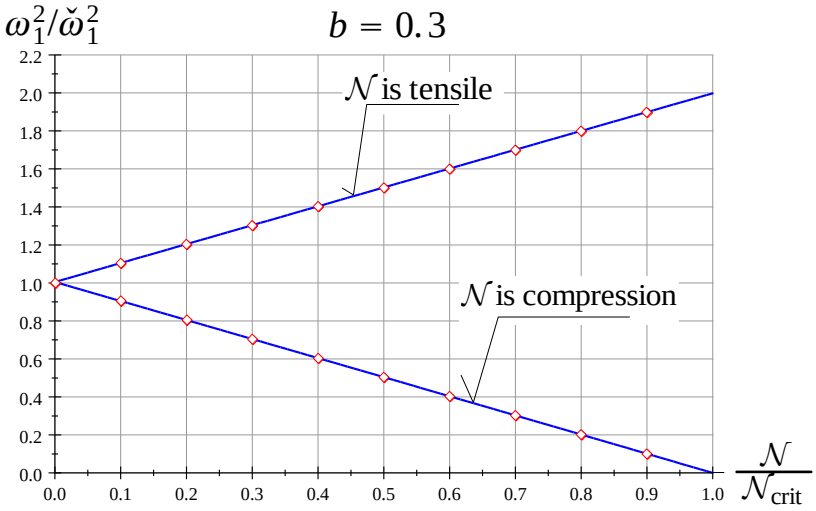

Figure 8.

$$\frac{\omega_1^2}{\check{\omega}_1^2} = \frac{\lambda_1}{\check{\lambda}_1} = 1.004\,689 - 0.997\,570\,\frac{\mathcal{N}}{\mathcal{N}_{\text{crit}}} - 7.276\,534 \times 10^{-3}\left(\frac{\mathcal{N}}{\mathcal{N}_{\text{crit}}}\right)^2, \tag{5.7a}$$

$$\frac{\omega_1^2}{\check{\omega}_1^2} = \frac{\lambda_1}{\check{\lambda}_1} = 1.004\,794 + 0.997\,875\,\frac{\mathcal{N}}{\mathcal{N}_{\text{crit}}} - 4.643\,405 \times 10^{-3}\left(\frac{\mathcal{N}}{\mathcal{N}_{\text{crit}}}\right)^2. \tag{5.7b}$$

5.6. **Numerical results if** $b = 0.4$**.** Table 6 and Figure 9 represent the results obtained.

Table 6.

		$b = 0.4$			
		$\sqrt{\mathcal{N}_{\text{crit}}}/\pi = 1.93113,\ \check{\lambda}_1 = 3.3881$			
		Compression		Tension	
Load step	$\mathcal{N}/\mathcal{N}_{\text{crit}}$ (p^2/p^2_{crit})	$\omega_1^2/\check{\omega}_1^2$ $(\lambda_1/\check{\lambda}_1)$	Difference	$\omega_1^2/\check{\omega}_1^2$ $(\lambda_1/\check{\lambda}_1)$	Difference
1	0.00	1.000000		1.000000	
2	0.10	0.894987	-0.098455	1.091328	0.098059
3	0.20	0.796529	-0.098458	1.189232	0.097904
4	0.30	0.697862	-0.098666	1.286971	0.097739
5	0.40	0.598974	-0.098888	1.384555	0.097583
6	0.50	0.499848	-0.099125	1.481990	0.097435
7	0.60	0.400468	-0.099380	1.579285	0.097294
8	0.70	0.300814	-0.099653	1.676446	0.097160
9	0.80	0.200866	-0.099947	1.773479	0.097033
9	0.90	0.100599	-0.100266	1.870391	0.096911

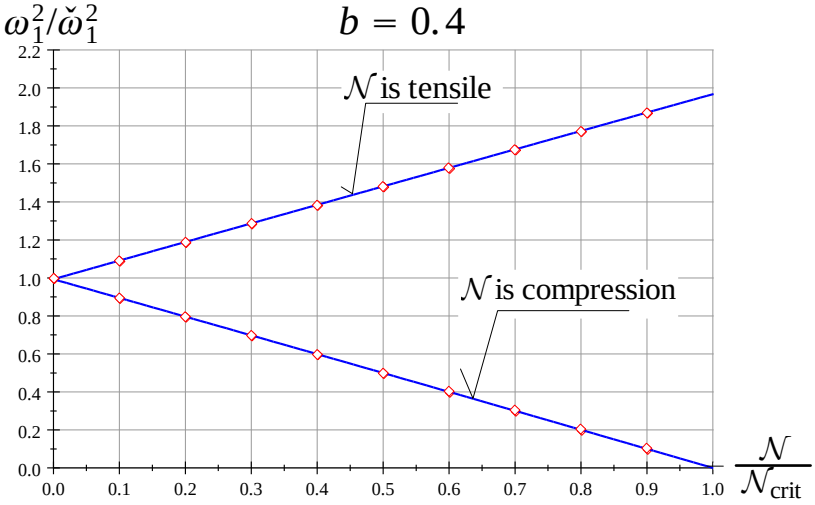

Figure 9.

The two quadratic polynomials fitted onto the numerical results are presented here:

$$\frac{\omega_1^2}{\check{\omega}_1^2} = \frac{\lambda_1}{\check{\lambda}_1} = 0.993\,088 - 0.980\,042\,\frac{\mathcal{N}}{\mathcal{N}_{\text{crit}}} - 1.286\,556 \times 10^{-2}\left(\frac{\mathcal{N}}{\mathcal{N}_{\text{crit}}}\right)^2, \tag{5.8a}$$

$$\frac{\omega_1^2}{\check{\omega}_1^2} = \frac{\lambda_1}{\check{\lambda}_1} = 0.993\,323 + 0.980\,873\frac{\mathcal{N}}{\mathcal{N}_{\text{crit}}} - 7.074\,0713 \times 10^{-3}\left(\frac{\mathcal{N}}{\mathcal{N}_{\text{crit}}}\right)^2. \tag{5.8b}$$

5.7. **Numerical results if $b = 0.5$.** Table 7 represents the results obtained.

Table 7.

		$b = 0.5$			
		$\sqrt{\mathcal{N}_{\text{crit}}}/\pi = 2.0000$, $\check{\lambda}_1 = 4.0000$			
		Compression		Tension	
Load step	$\mathcal{N}/\mathcal{N}_{\text{crit}}$ (p^2/p^2_{crit})	$\omega_1^2/\check{\omega}_1^2$ $(\lambda_1/\check{\lambda}_1)$	Difference	$\omega_1^2/\check{\omega}_1^2$ $(\lambda_1/\check{\lambda}_1)$	Difference
1	0.00	1.000000		1.000000	
2	0.10	0.893682	-0.099310	1.092295	0.099313
3	0.20	0.794376	-0.099306	1.191601	0.099306
4	0.30	0.695069	-0.099306	1.290908	0.099306
5	0.40	0.595763	-0.099306	1.390214	0.099306
6	0.50	0.496457	-0.099306	1.489521	0.099306
7	0.60	0.397150	-0.099306	1.588827	0.099306
8	0.70	0.297844	-0.099306	1.688133	0.099306
9	0.80	0.198538	-0.099306	1.787440	0.099306
9	0.90	0.099231	-0.099306	1.886746	0.099306

The polynomial approximations (the differences are constants)

$$\frac{\omega_1^2}{\check{\omega}_1^2} = \frac{\lambda_1}{\check{\lambda}_1} = 0.993\,064 - 0.992\,989\,\frac{\mathcal{N}}{\mathcal{N}_{\text{crit}}} \approx 1.000 - \frac{\mathcal{N}}{\mathcal{N}_{\text{crit}}}\,, \tag{5.9a}$$

$$\frac{\omega_1^2}{\check{\omega}_1^2} = \frac{\lambda_1}{\check{\lambda}_1} = 0.993\,064 + 0.992\,989\frac{\mathcal{N}}{\mathcal{N}_{\text{crit}}} \approx 1.000 + \frac{\mathcal{N}}{\mathcal{N}_{\text{crit}}}\,. \tag{5.9b}$$

show that the functions $\omega_1^2/\check{\omega}_1^2(\mathcal{N}/\mathcal{N}_{\text{crit}})$ fitted onto the computational results are linear.

5.8. **What characters do the solutions have?** If $b \neq 0.5$ the function

$$\omega_1^2/\check{\omega}_1^2(\mathcal{N}/\mathcal{N}_{\text{crit}})$$

is non-linear, but the deviation from the linearity is not significant at all. It becomes smaller when $b \longrightarrow 0.5$. If $b = 0.5$ the half beam behaves as if it were a simply supported beam for which the function $\omega_1^2/\check{\omega}_1^2(\mathcal{N}/\mathcal{N}_{\text{crit}})$ is, in principal, a linear one. This fact is reflected in equations (5.9).

6. Concluding remarks

The present paper clarifies what effect the axial load (compressive or tensile) has on the eigenfrequencies of a heterogeneous pinned-pinned beam with an intermediate roller support. This problem is, in fact, a three-point boundary value problem (eigenvalue problem) associated with homogeneous boundary conditions. After determining the Green function of the three-point boundary value problem the eigenvalue problem that provides the eigenfrequencies for the PrsP beam is transformed into an eigenvalue problem governed by a homogeneous Fredholm integral equation with the Green

function as its kernel. The later eigenvalue problem is reduced to an algebraic eigenvalue problem which we solved numerically by using an effective solution algorithm based on the boundary element method. We have derived polynomial approximations for the sought function $\omega_1^2/\breve{\omega}_1^2(\mathcal{N}/\mathcal{N}_{\mathrm{crit}})$.

References

1. I. Ecsedi and D. Gönczi. "Thermoelastic stresses in nonhomogeneous prismatic bars." *Annals of Faculty of Engineering Hunedoara - International Journal of Engineering,* **13**(2), (2015), pp. 49–52.
2. I. Ecsedi and A. Baksa. "Deformation of a cantilever curved beam with variable cross section." *Journal of Computational and Applied Mechanics,* **16**(1), (2021), pp. 23–36. URL: 10.32973/jcam.2021.006.
3. H. K. Kim and M. S. Kim. "Vibration of beams with generally restrained boundary conditions using Fourier series." *Journal of Sound and Vibration,* **245**(5), (2001), pp. 771–784. DOI: 10.1006/jsvi.2001.3615.
4. A. Bizzi, E. L. Fortaleza, and T. S. N. Guenka. "Dynamics of heavy beams: Closed-form vibrations of gravity-loaded Rayleigh–Timoshenko columns." *Journal of Sound and Vibration,* **510**, (2021), p. 116259. DOI: 10.1016/j.jsv.2021.116259.
5. V. Ondra and B. Titurus. "Free vibration and stability analysis of a cantilever beam axially loaded by an intermittently attached tendon." *Mechanical Systems and Signal Processing,* **158**, (2021), p. 107739. DOI: 10.1016/j.ymssp.2021.107739.
6. B. Bozyigit, Y. Yesilce, and S. Catal. "Free vibrations of axial-loaded beams resting on viscoelastic foundation using Adomian decomposition method and differential transformation." *Engineering Science and Technology, an International Journal,* **21**(6), (2018), pp. 1181–1193. ISSN: 2215-0986. DOI: 10.1016/j.jestch.2018.09.008.
7. A. Mirzabeigy and R. Madoliat. "Large amplitude free vibration of axially loaded beams resting on variable elastic foundation." *Alexandria Engineering Journal,* **55**(2), (2016), pp. 1107–1114. DOI: 10.1016/j.aej.2016.03.021. URL: https://www.sciencedirect.com/science/article/pii/S1110016816300345.
8. Jong-Shyong Wu and Bo-Hau Chang. "Free vibration of axial-loaded multi-step Timoshenko beam carrying arbitrary concentrated elements using continuous-mass transfer matrix method." *European Journal of Mechanics - A/Solids,* **38**, (2013), pp. 20–37. DOI: 10.1016/j.euromechsol.2012.08.003.
9. G. G. G. Lueschen, L. A. Bergman, and D. M. McFarland. "Green's functions for uniform Timoshenko beams." *Journal of Sound and Vibration,* **194**(1), (1996), pp. 93–102. DOI: 10.1006/jsvi.1996.0346.
10. M. A. Foda and Z. Abduljabbar. "A dynamic Green function formulation for the response of a beam structure to a moving mass." *Journal of Sound and Vibration,* **210**(3), (1998), pp. 295–306. DOI: 10.1006/jsvi.1997.1334.

11. S. Kukla and I. Zamojska. "Frequency analysis of axially loaded stepped beams by Green's function method." *Journal of Sound and Vibration,* **300**(3), (2007), pp. 1034–1041. DOI: 10.1016/j.jsv.2006.07.047.
12. G. Failla and A. Santini. "On Euler–Bernoulli discontinuous beam solutions via uniform-beam Green's functions." *International Journal of Solids and Structures,* **44**(22), (2007), pp. 7666–7687. DOI: 10.1016/j.ijsolstr.2007.05.003.
13. A. Baksa and I. Ecsedi. "A note on the pure bending of nonhomogeneous prismatic bars." *International Journal of Mechanical Engineering Education,* **37**(2), (2009), pp. 118–129. URL: 10.7227/IJMEE.37.2.4.
14. L. P. Kiss. "Vibrations and Stability of Heterogeneous Curved Beams." Ph.D Thesis. Institute of Applied Mechanics, University of Miskolc, Hungary, 2015. URL: http://geik.uni-miskolc.hu/intezetek/SALYI/ertekezesek.
15. G. Szeidl and L. Kiss. "Green Functions for Three Point Boundary Value Problems with Applications to Beams." *Advances in Mathematics Research.* Ed. by Albert R. Raswell. New York: Nova Science Publisher, Inc., 2020. Chap. Chapter 5, pp. 121–161.
16. J. M. Hoene-Wroński. *Réfutation de la théorie des fonctions analytiques de Lagrange.* Blankenstein, Paris, 1812.
17. L. Kiss, G. Szeidl, and M. Abderrazek. "Stability of heterogeneous beams with three supports – a novel approach to some classical stability problems." Unpublished manuscript. 2021.
18. G. Szeidl and L. P. Kiss. *Mechanical Vibrations, an Introduction.* Ed. by Vladimir I. Babitsky and Jens Wittenburg. Foundation of Engineering Mechanics. Springer Nature, Switzerland, 2005. Chap. 10. DOI: 10.1007/978-3-030-45074-8.

Journal of Computational and Applied Mechanics, Vol. 16, No. 2, (2021), pp. 129–157
DOI: 10.32973/jcam.2021.008

FINDING A WEAK SOLUTION OF THE HEAT DIFFUSION DIFFERENTIAL EQUATION FOR TURBULENT FLOW BY GALERKIN'S VARIATION METHOD USING P-VERSION FINITE ELEMENTS

I. Páczelt
Institute of Applied Mechanics, University of Miskolc
3515 Miskolc-Egyetemváros, Hungary
Istvan.Paczelt@uni-miskolc.hu

[Received: September 29, 2021; Accepted: November 11, 2021]

Dedicated to Professor Tibor Czibere on the occasion of his 90th birthday

Abstract. The stochastic turbulence model developed by Professor Czibere provides a means of clarifying the flow conditions in pipes and of describing the heat evolution caused by shear stresses in the fluid. An important part of the theory is a consideration of the heat transfer-diffusion caused by heat generation. Most of the heat is generated around the pipe wall. One part of the heat enters its environment through the wall of the tube (heat transfer), the other part spreads in the form of diffusion in the liquid, increasing its temperature. The heat conduction differential equation related to the model contains the characteristics describing the turbulent flow, which decisively influence the resulting temperature field, appear. A weak solution of the boundary value problem is provided by Bubnov-Galerkin's variational principle. The axially symmetric domain analyzed is discretized by a geometrically graded mesh of a high degree of p-version finite elements, this method is capable of describing substantial changes in the temperature gradient in the boundary layer. The novelty of this paper is the application of the p-version finite element method to the heat diffusion problem using Czibere's turbulence model. Since the material properties depend on temperature, the problem is nonlinear, therefore its solution can be obtained by iteration. The temperature states of the pipes are analyzed for a variety of technical parameters, and useful suggestions are proposed for engineering designs.

Mathematical Subject Classification: 76F10, 80A19, 65N30
Keywords: Stochastic turbulent flow model, heat diffusion problem, Galerkin method, p-version finite elements

1. Introduction

In short, the calculation of turbulent flow in a long straight pipe based on the stochastic turbulence model [1–3] will be summarized. In this model, the mechanical similarity hypothesis was successfully extended to a three-dimensional turbulent flow by confirming it with experimental results. The model is suitable for investigating steady-state turbulent flow. An important result is the introduction of the eddy viscosity tensor $\mathbf{G}$ instead of the Bousinesq scalar vortex viscosity factor, as well as an extended interpretation of Prandtl's length scale $l_{\max}$. The latter could be derived using the known dimensional analysis: $(l = l_{\max}/\kappa)$. Here l is the length scale of turbulence, and κ is the Kármán constant.

This paper does not aim to critically analyze different turbulence models [4–11]. Here, we focus primarily on the approximate solution of the thermal conduction problem related to Czibere's turbulence model.

1.1. **Fundamental assumptions.** For an incompressible fluid flow in the stochastic turbulence model, the governing equations of the transport of mass, momentum, internal energy and the turbulent kinetic energy equation are written in direct notation:

$$\nabla \cdot \mathbf{v} = 0\,, \tag{1}$$

$$\rho\left(\frac{\partial \mathbf{v}}{\partial t} + (\mathbf{v}\cdot\nabla)\,\mathbf{v}\right) = \rho\mathbf{g} - \nabla\mathbf{p} - \frac{2}{3}\rho\nabla k + \eta\Delta\mathbf{v} + \mathrm{Div}\,(\Theta\mathbf{G}) \tag{2}$$

$$\rho c_p\left(\frac{\partial T}{\partial t} + (\mathbf{v}\cdot\nabla)\,T\right) = \nabla\cdot\left[(\lambda+\Lambda)\,\nabla T\right] + \rho\,(\varphi_D + \varepsilon) \tag{3a}$$

$$\rho\left(\frac{\partial k}{\partial t} + (\mathbf{v}\cdot\nabla)\,k\right) = \Theta\mathbf{G} : (\nabla\circ\mathbf{v}) - \rho\varepsilon - \nabla\cdot\left\{\frac{\Theta^{3/2}\mathbf{t}}{2\rho^{1/2}\kappa^3} - \frac{C_k}{\kappa\Omega}\,(\Theta\rho k)^{1/2}\right\} + \\ + \upsilon\left[\frac{5}{3}\rho\Delta k - \nabla\cdot\mathrm{Div}\,(\Theta\mathbf{G})\right], \tag{3b}$$

where the interpretation of the different quantities can be found in the Nomenclature. In addition, $\mathbf{H}$ and $\mathbf{H}_*$ are the similarity tensor and its deviator of the stochastic turbulence model, respectively:

$$\mathbf{H} = \begin{pmatrix} \alpha & 1 & 0 \\ 1 & \beta & 0 \\ 0 & 0 & \gamma \end{pmatrix}, \qquad \mathbf{H}_* = \begin{pmatrix} \alpha_* & 1 & 0 \\ 1 & \beta_* & 0 \\ 0 & 0 & \gamma_* \end{pmatrix}; \qquad \begin{aligned} \alpha_* &= \tfrac{1}{3}\,(2\alpha-\beta-\gamma) \\ \beta_* &= \tfrac{1}{3}(2\beta-\alpha-\gamma) \\ \gamma_* &= \tfrac{1}{3}(2\gamma-\alpha-\beta) \end{aligned}$$

where $a^2 = -\frac{1}{2}(\alpha+\beta+\gamma)$, $\alpha = -3.28$, $\beta = -1.64$, $\gamma = -2.46\times\mathbf{v}$ are the three entries of these tensors, according to Prandtl parameter $C_k \le 1$. Naturally, for fully-developed turbulent flows, the terms of the time derivatives are omitted in equations (2) and (3). $\mathbf{G}$, the eddy viscosity tensor, is also defined as $\mathbf{G} = \mathbf{E}\cdot\mathbf{H}_*\cdot\mathbf{E}^T$, where $\mathbf{E} = [E_{ij}]$ is the tensor of the transformation between the natural and the reference coordinate systems, with $\mathbf{E}^T = [E_{ji}]$ being its transpose. The elements of the transformation tensor $\mathbf{E}$ are given as:

$$E_{i1} = \frac{1}{\sqrt{1-S^2}}\left(\frac{v_i}{v} - S\frac{\Omega_i}{\Omega}\right), \quad E_{i2} = \frac{1}{\sqrt{1-S^2}}\left(\frac{v_{i+1}\Omega_{i+2} - v_{i+2}\Omega_{i+1}}{v\Omega}\right), \quad E_{i3} = -\frac{\Omega_i}{\Omega}$$

$$v = \sqrt{v_1^2+v_2^2+v_3^2}, \quad \Omega = \sqrt{\Omega_1^2+\Omega_2^2+\Omega_3^2}, \quad S = \frac{1}{\sqrt{1-S^2}}\left(\frac{v_1\Omega_1 + v_2\Omega_2 + v_3\Omega_3}{v\Omega}\right),$$

$$i = 1, 2, 3$$

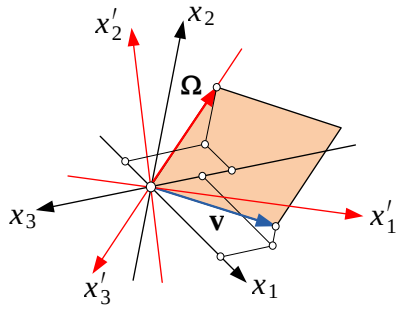

Figure 1. Natural x_1', x_2', x_3' and reference x_1, x_2, x_3 coordinate systems [1]

The base vectors of the natural coordinate system are defined by the velocity $\mathbf{v}$ and vortex velocity vector $\mathbf{\Omega} = \nabla \times \mathbf{v}$:

$$\mathbf{e}_2' = \frac{\mathbf{v} \times \mathbf{\Omega}}{|\mathbf{v} \times \mathbf{\Omega}|}, \qquad \mathbf{e}_3' = -\frac{\mathbf{\Omega}}{\Omega} = -\frac{\nabla \times \mathbf{v}}{|\nabla \times \mathbf{v}|}, \qquad \mathbf{e}_1' = \mathbf{e}_2' \times \mathbf{e}_3'.$$

Equations (1) to (3) consist of a total of five scalar differential equations. In this differential equation system there are six unknown functions: $(v_1, v_2, v_3, p, T, \Theta)$, therefore the system (1)-(3) is underdetermined, that is, it needs to be supplemented with one equation.

The additional differential equation is created considering the following assumptions. Using the definition of the specific turbulent dissipation

$$\varepsilon = \upsilon \overline{(\mathbf{v}' \circ \nabla) : (\mathbf{v}' \circ \nabla + \nabla \circ \mathbf{v}')}$$

in case of stochastic turbulence it is written as [1]:

$$\varepsilon = -\upsilon\kappa^2 \left[a_{11}A_1^2 + a_{22}A_2^2 + a_{33}A_3^2 + 2\left(a_{12}A_1A_2 + a_{13}A_1A_3 + a_{23}A_2A_3\right)\right],$$

where $\mathbf{v}'$ is fluctuation of the velocity, and $\bar{(\cdot)}$ is the time-average value,

$$a_{11} = 2\alpha + \beta + \gamma, \qquad a_{22} = \alpha + 2\beta + \gamma, \qquad a_{33} = \alpha + \beta + 2\gamma,$$
$$a_{12} = \alpha + \beta + \gamma + 1, \qquad a_{13} = \alpha + \beta + \gamma, \qquad a_{23} = \alpha + \beta + \gamma,$$

$$A_i = \frac{1}{2\kappa\left(\rho\Theta\right)^{1/2}}\left[E_{i1}\frac{\partial\Theta}{h_1\partial x_1} + E_{i2}\frac{\partial\Theta}{h_2\partial x_2} + E_{i3}\frac{\partial\Theta}{h_3\partial x_3}\right], \qquad i = 1, 2, 3.$$

The π theorem of dimensional analysis states that every physical process can be outlined by a relationship between a certain number of dimensionless characteristics. The process of turbulent fluctuation is fundamentally determined by the length scale l, the absolute value of the vortex vector $\mathbf{\Omega}$, the specific turbulent dissipation ε, and the kinematic viscosity υ of the medium [1]. In view of the above, with the help of the π theory of dimension analysis, the specific turbulent dissipation ε takes the form of

$$\varepsilon = C_E \upsilon^N \frac{\Omega^{N-1}}{\left(l\Omega\right)^{2(N-1)}} = C_E \kappa^{2(N-1)} \frac{\eta^N}{\rho} \frac{\Omega^{N-1}}{\Theta^{N-1}},$$

where $1 < N < 3$ and C_E is a suitably chosen coefficient. The additional differential equation is obtained by combining the two equations for ε:

$$a_{11}A_1^2 + a_{22}A_2^2 + a_{33}A_3^2 + 2\left(a_{12}A_1A_2 + a_{13}A_1A_3 + a_{23}A_2A_3\right) = \\ = -C_E\kappa^{2(N-2)}\eta^{N-1}\frac{\Omega^{N-1}}{\Theta^{N-1}}. \quad (4)$$

As there is no unknown function in this differential equation, it is a good candidate for supplementing the underdetermined system of differential equations (1) to (3), forming a *one-equation* version of the stochastic turbulence model.

The following will address axisymmetric problems for a steady-state turbulent flow, that is the problems are time-independent.

In the case of fluid flow in a long straight pipe, in the x_1, x_2, x_3 coordinate system, only the velocity component v_1 depends on the radial coordinate x_2, and it is different from zero. In this case, the turbulence length scale l varies only in the radial direction, and consequently the dominant turbulent shear stress Θ and the turbulent kinetic energy k also depend only on radial direction: i.e., $\Theta(x_2)$ and $k(x_2)$. However, pressure and temperature depend on two coordinates: i.e., $p(x_1, x_2)$, $T(x_1, x_2)$. After that, the vortex components are given as follows:

$$\Omega_1 = \Omega_2 = 0, \qquad \Omega_3 = -\frac{dv_1}{dx_2}.$$

Entries of tensor $\mathbf{E}$ transforming between the natural and reference coordinate systems are given as:

$$\begin{aligned} &E_{11} = 1, && E_{12} = 0, && E_{13} = 0, \\ &E_{21} = 0, && E_{22} = -1, && E_{23} = 0, \\ &E_{31} = 0, && E_{32} = 0, && E_{33} = -1. \end{aligned}$$

The entries of the vortex viscosity tensor $\mathbf{G}$ are as follows:

$$\begin{aligned} &G_{11} = \alpha_*, && G_{22} = \beta_*, && G_{33} = \gamma_* \\ &G_{12} = G_{21} = -1, && G_{13} = G_{31} = G_{23} = G_{32} = 0. \end{aligned}$$

This means that in the case of fluid flow in a long straight pipe, the continuity equation (1) is automatically satisfied; and the equation of linear momentum (2) develops in this way by neglecting the gravity force in axial direction:

$$0 = -\frac{\partial p}{\partial x_1} + \eta\left(\frac{d^2v_1}{dx_2} + \frac{1}{x_2}\frac{dv_1}{dx_2}\right) - \frac{d\Theta}{dx_2} - \frac{\Theta}{x_2} \quad (5a)$$

in radial direction:

$$0 = -\frac{\partial p}{\partial x_2} + \left(\beta_* - \frac{2a^2}{3}\right)\frac{d\Theta}{dx_2} + \frac{\Theta}{x_2}(\beta_* - \gamma_*) \quad (5b)$$

Deriving (5a) with respect to x_1, $\frac{\partial^2 p}{\partial x_1^2} = 0$ is obtained for the pressure p, and its solution is given as $p(x_1, x_2) = A(x_2) + Bx_1$, where constant B can be calculated by a pressure drop $\Delta p = p_1 - p_2$, which is measured in length L of the pipe $B = -\frac{\Delta p}{L}$,

$p_1 = p(0, x_2)$, $p_2 = p_2(L, x_2)$. Then the momentum equations (5a) and (5b) can be written in the following form:

$$\eta\left(\frac{d^2v_1}{dx_2} + \frac{1}{x_2}\frac{dv_1}{dx_2}\right) - \frac{d\Theta}{dx_2} - \frac{\Theta}{x_2} = -\frac{\Delta p}{L}, \tag{6a}$$

$$\left(\beta_* - \frac{2a^2}{3}\right)\frac{d\Theta}{dx_2} + \frac{\Theta}{x_2}(\beta_* - \gamma_*) = f^{'}(x_2). \tag{6b}$$

Equation (6a) can be reshaped as follows:

$$\eta\frac{d}{dx_2}\left(x_2\frac{dx_1}{dx_2}\right) - \frac{d}{dx_2}(x_2\Theta) = -\frac{\Delta p}{L}x_2.$$

This equation is integrated with respect to x_2, and the result is divided by x_2:

$$\eta\frac{dv_1}{dx_2} - \Theta = -\frac{\Delta p}{2L}x_2 + \frac{C}{x_2}.$$

Taking into account that in the middle of the pipe (where $x_2 = 0$) neither dv_1/dx_2 nor the dominant turbulent shear stress Θ can be infinitely high, the integration constant C is zero. Thus the momentum equation (6a) is finally written as follows:

$$\eta\frac{dv_1}{dx_2} - \Theta = -\frac{\Delta p}{2L}x_2 \tag{7}$$

In the case of fluid flow in a long straight pipe, the parameters A_i of equation (4) are given as follows:

$$A_1 = 0, \qquad A_2 = -\frac{1}{2\kappa\left(\rho\Theta\right)^{1/2}}\frac{d\Theta}{dx_2}, \qquad A_3 = 0.$$

Finally, equation (4) takes the form of:

$$\frac{a_{22}}{4\kappa^2\rho\Theta}\left(\frac{d\Theta}{dx_2}\right)^2 = -C_E\kappa^{2(N-2)}\eta^{N-1}\frac{\Omega^{N+1}}{\Theta^{N-1}}$$

After some manipulations we have the following form:

$$\Theta^{\frac{N-2}{2}}\frac{d\Theta}{dx_2} = 2\rho^{\frac{N}{2}}\left(-\frac{C_E\upsilon^{N-1}}{\alpha + 2\beta + \gamma}\right)^{1/2}\kappa^{N-1}\Omega^{\frac{N+1}{2}}. \tag{8}$$

It is easy to see that from the point of view of determining the unknown functions v_1 and Θ, differential equations (7) and (8) form a closed system. By solving them, the functions can be numerically determined.

1.2. **Preparation for numerical computations.** Numerical computations are performed with dimensionless physical variables. The dimensionless counterpart of velocity v_1 is the wall friction velocity v_*, which is defined by the viscous shear stress on the wall $\tau(R_0)$. The wall friction velocity is obtained as:

$$\rho v_*^2 = |\tau R_0| = \eta\left|\frac{dv_1}{dx_2}\right|_{x_2=R_0} = \frac{\Delta p R_0}{2L}, \qquad v_* = \sqrt{\frac{\Delta p R_0}{\rho 2L}},$$

where R_0 is the inner radius of the pipe. The modified Reynolds number is calculated with the wall friction velocity v_*: $\mathrm{Re}_* = v_* R_0/\upsilon$.

Introducing the following notations

$$\xi = \frac{x_2}{R_0}, \qquad V(\xi) = \frac{v_1}{v_*}, \qquad H(\xi) = \frac{\Theta}{\rho v_*^2}$$

the momentum transport equation (7) takes the form of

$$\frac{dV}{d\xi} = \mathrm{Re}_*(H - \xi). \tag{9a}$$

Using the dimensionless parameters in differential equation (7) and substituting them into equation (9a), the following differential equation is obtained:

$$\frac{dH}{d\xi} = C_H\sqrt{\frac{|H-\xi|^{N+1}}{H^{N-2}}}, C_H = 2\kappa^{N-1}\,\mathrm{Re}_*\sqrt{-\frac{C_E}{\alpha+2\beta+\gamma}} \tag{9b}$$

where coefficient C_H from the numerical experiment is [3]:

$$C_H = 0.157\,\mathrm{Re}_*^{1.528} \text{ for } \mathrm{Re}_* < 1134, \quad C_H = 1.125\,\mathrm{Re}_*^{1.248} \text{ for } 1134 < \mathrm{Re}_* < 21553,$$

$$C_H = 446\,\mathrm{Re}_*^{0.418} \text{ for } 21553 < \mathrm{Re}_*$$

By solving the closed system of differential equations (9a) and (9b), the functions $V(\xi)$ and $H(\xi)$ can be numerically determined. The boundary conditions at $\xi = 0$ are defined as:

$$H(0) = 0, \qquad V(0) = \frac{v_m}{v_*} = \frac{1}{\kappa}\ln \mathrm{Re}_* + 6.0,$$

where v_m is the velocity maximum [3]. Differential equations (9a) and (9b) are solved by the Runge-Kutta method.

For fluid flows in pipes, the relationship between the Reynolds number Re and its modified value Re_* is written as $\mathrm{Re}_* = \sqrt{\frac{f}{2}}\frac{\mathrm{Re}}{4}$, where

$$\mathrm{Re} = \frac{2v_a R_0}{\upsilon}\frac{1}{\sqrt{f}} = \frac{1}{2\kappa\sqrt{2}}\ln\left(\mathrm{Re}\sqrt{f}\right) - 0.8. \tag{10}$$

Here v_a is the average velocity in the pipe section, f is the friction factor in the fluid flow.

Differential equations (9a) and (9b), like the turbulence model itself, are based on the already fully formed turbulence condition. They lose their validity in the viscous boundary layer along the wall because the presence of the wall attenuates the development of turbulence. Therefore, the slowing effect of the wall on the turbulence in the pipe flow is represented by the following damping function $\tilde{D}(\xi)$:

$$\widetilde{D}(\xi) = \exp\left(\frac{b\xi}{\xi - 1}\right), \qquad b = \frac{3}{\mathrm{Re}_*}.$$

Multiplying the solution of differential equation (9b) by this damping function, the result satisfies also the boundary condition $H(1) = 0$. Then differential equation (9a) is solved with the attenuated distribution $H(\xi)$ to determine the function $V(\xi)$. In order to satisfy the condition $V(1) = 0$, differential equation (9a) is solved with the

help of the following multiplicative cutoff function, which makes the solution smooth in the vicinity of the wall:

$$Y(\xi) = (\widetilde{A}_1\xi + \widetilde{A}_0)(\xi - 1), \xi_\delta \le \xi \le 1$$

where $\xi_\delta = 1 - 3/\operatorname{Re}_*$ denotes the location of the fitting; and the coefficients $\widetilde{A}_1$ and $\widetilde{A}_0$ can be calculated as follows:

$$\widetilde{A}_1 = \frac{V^{'}(\xi_\delta)}{\xi_\delta - 1} - \frac{V(\xi_\delta)}{(\xi_\delta - 1)^2}, \qquad A_0 = V^{'}(\xi_\delta) - (2\xi_\delta - 1)\widetilde{A}_1$$

In case of stationary flow in a long straight pipe, using the divergence of the vector function $\mathbf{f}(r)$:

$$\nabla \cdot \mathbf{f} = \frac{1}{h_1 h_2 h_3}\left(\frac{\partial}{\partial x_1}(f_1 h_2 h_3) + \frac{\partial}{\partial x_2}(f_2 h_3 h_1) + \frac{\partial}{\partial x_3}(f_3 h_1 h_2)\right)$$

and taking into account that $h_1 = h_2 = 1$ and $h_3 = x_2$ the transport equation for internal energy (3) will have the form

$$\rho c_p v_1 \frac{\partial T}{\partial x_1} = \frac{\partial}{\partial x_1}\left[(\lambda + \Lambda)\frac{\partial T}{\partial x_1}\right] + \frac{\partial}{\partial x_2}\left[(\lambda + \Lambda)\frac{\partial T}{\partial x_2}\right] + \\ + \frac{1}{x_2}(\lambda + \Lambda)\frac{\partial T}{\partial x_2} + \rho(\varphi_D + \varepsilon), \qquad (11a)$$

where the viscous and turbulent dissipations φ_D and ε are given by the expressions

$$\varphi_D = \upsilon\left(\frac{dv_1}{dx_2}\right)^2, \qquad \varepsilon = -\upsilon\frac{a_{22}}{4\rho\Theta}\left(\frac{d\Theta}{dx_2}\right)^2.$$

Let us introduce dimensionless location coordinates $s = x_1/R_0$, $\xi = x_2/R_0$ and dimensionless variables

$$\varphi = \frac{R_0\varphi_D}{v_*^3} = \frac{1}{\operatorname{Re}_*}\left(\frac{dV}{d\xi}\right)^2, \quad \psi = \frac{R_0\varepsilon}{v_*^3} = -\frac{\alpha + 2\beta + \gamma}{4\operatorname{Re}_* H}\left(\frac{dH}{d\xi}\right)^2, \quad \vartheta = \frac{T}{T_0},$$

where T_0 is the reference temperature.

The former transport equation of internal energy (11a) with the dimensionless coordinates and variables is formed as

$$\operatorname{Pr}\operatorname{Re}_* V(\xi)\frac{d\vartheta}{ds} = \frac{1}{\lambda}\left[\frac{\partial\lambda}{\partial s}(1 + \frac{\Lambda}{\lambda})\frac{\partial\vartheta}{\partial s}\right] + \frac{1}{\lambda}\left[\frac{\partial\lambda}{\partial\xi}(1 + \frac{\Lambda}{\lambda})\frac{\partial\vartheta}{\partial\xi}\right] + \\ + \frac{\partial}{\partial s}\left[(1 + \frac{\Lambda}{\lambda})\frac{\partial\vartheta}{\partial s}\right] + \frac{\partial}{\partial\xi}\left[(1 + \frac{\Lambda}{\lambda})\frac{\partial\vartheta}{\partial\xi}\right] + \frac{1}{\xi}(1 + \frac{\Lambda}{\lambda})\frac{\partial\vartheta}{\partial\xi} + \operatorname{Pr}\operatorname{Re}_*\operatorname{Ec}(\varphi + \psi), \quad (11b)$$

where $\operatorname{Pr} = \eta c_p/\lambda$ is the Prandtl number and $\operatorname{Ec} = v_*^2/(c_p T_0)$ is the Eckert number.

The ratio of the turbulent and molecular heat conductivity factors Λ and λ is given as:

$$\frac{\Lambda}{\lambda} = \frac{c_p}{\lambda}\frac{\kappa_*}{\kappa}\frac{\Theta}{\Omega} = \operatorname{Pr}\operatorname{Re}_*\frac{\kappa_*}{\kappa}H\left|\frac{d\xi}{dV}\right| = \operatorname{Pr}\frac{\kappa_*}{\kappa}\frac{H}{|H - \xi|}$$

The partial differential equation (11b) can be solved for the given initial and boundary conditions when $V(\xi)$ and $H(\xi)$ are known. The similarity numbers Pr, Re_*, Ec and

$\frac{\Lambda}{\lambda}$ depend on temperature T. An approximate solution of differential equation (11b) will be proposed in the following.

2. Variational equation of thermal convection-diffusion problems

It should be emphasized that the variational discussion of the convection-diffusion heat transfer problem of turbulent flow and then its p-version finite element solution constitute a new contribution part of this work.

At the given average pipe velocity v_a, the value $\tilde{\mathrm{Ec}} = \nu_a^2/(c_p T_0)$ can be determined by interpolating c_p in Table 1 for a given temperature. According to equation (10), Re_* can be calculated, and using equation $\mathrm{Re}_* = v_* R_0/\upsilon$, v_* will be known. Hence $\mathrm{Ec} = v_*^2/(c_p T_0)$ and also $\mathrm{Ec} = \tilde{\mathrm{Ec}}/(v_a v_*)^2$ can be written.

Let us introduce the following value: $C = 1 + \frac{\Lambda}{\lambda}$.

Rewrite equation (11b) for coordinates x_1, x_2:

$$\mathrm{Pr}\,\mathrm{Re}_* V(\xi)\frac{\partial T}{\partial x_1}\frac{R_0}{T_0} = \frac{1}{\lambda}\left[\frac{\partial \lambda}{\partial x_1} C \frac{\partial T}{\partial x_1}\right]\frac{R_0^2}{T_0} + \frac{1}{\lambda}\left[\frac{\partial \lambda}{\partial x_2} C \frac{\partial T}{\partial x_2}\right]\frac{R_0^2}{T_0} + \\ + \frac{R_0^2}{T_0}\frac{\partial}{\partial x_1}\left[C\frac{\partial T}{\partial x_1}\right] + \frac{R_0^2}{T_0}\frac{\partial}{\partial x_2}\left[C\frac{\partial T}{\partial x_2}\right] + \frac{R_0^2}{T_0 x_2} C \frac{\partial T}{\partial x_2} + \\ + \mathrm{Pr}\,\mathrm{Re}_*\,\mathrm{Ec}(\varphi + \psi). \quad (12)$$

Then performing the derivations, equation (12) takes a new form:

$$\mathrm{Pr}\,\mathrm{Re}_* V(\xi)\frac{\partial T}{\partial x_1}\frac{R_0}{T_0} = \frac{1}{\lambda}\left[\frac{\partial \lambda}{\partial x_1} C \frac{\partial T}{\partial x_1}\right]\frac{R_0^2}{T_0} + \frac{1}{\lambda}\left[\frac{\partial \lambda}{\partial x_2} C \frac{\partial T}{\partial x_2}\right]\frac{R_0^2}{T_0} + \\ + \frac{R_0^2}{T_0}\left\{\frac{\partial C}{\partial x_1}\frac{\partial T}{\partial x_1} + \frac{\partial C}{\partial x_2}\frac{\partial T}{\partial x_2} + \frac{1}{x_2} C \frac{\partial T}{\partial x_2} + C\left[\frac{\partial^2 T}{\partial x_1^2} + \frac{\partial^2 T}{\partial x_2^2}\right]\right\} + \\ + \mathrm{Pr}\,\mathrm{Re}_*\,\mathrm{Ec}(\varphi + \psi). \quad (13)$$

Using the Laplace differential operator for the axisymmetric case, the following is obtained:

$$\mathrm{Pr}\,\mathrm{Re}_* V(\xi)\frac{\partial T}{\partial x_1}\frac{R_0}{T_0} = \frac{1}{\lambda}\left[\frac{\partial \lambda}{\partial x_1} C \frac{\partial T}{\partial x_1}\right]\frac{R_0^2}{T_0} + \frac{1}{\lambda}\left[\frac{\partial \lambda}{\partial x_2} C \frac{\partial T}{\partial x_2}\right]\frac{R_0^2}{T_0} + \\ + \frac{R_0^2}{T_0}\left\{\frac{\partial C}{\partial x_1}\frac{\partial T}{\partial x_1} + \frac{\partial C}{\partial x_2}\frac{\partial T}{\partial x_2} + C(\nabla^2 T)\right\} + \mathrm{Pr}\,\mathrm{Re}_*\,\mathrm{Ec}(\varphi + \psi) \quad (14)$$

Taking into account the definitions at the beginning of this chapter

$$\frac{\Lambda}{\lambda} = \frac{c_p}{\lambda}\frac{\kappa_*}{\kappa}\frac{\Theta}{\Omega} = \frac{\Lambda}{\lambda}(x_1, x_2), \quad (15)$$

this ratio depends on coordinates x_1, x_2. Therefore the following parameter will also depend on x_1, x_2:

$$C = 1 + \frac{\Lambda}{\lambda} = C(x_1, x_2) \quad (16)$$

Thus, differential equation (14) is written in a new form

$$\Im = \Im(T) = \\ = \left\{ \frac{1}{\lambda} \left[\frac{\partial \lambda}{\partial x_1} C \frac{\partial T}{\partial x_1} \right] + \frac{1}{\lambda} \left[\frac{\partial \lambda}{\partial x_2} C \frac{\partial T}{\partial x_2} \right] + \frac{\partial C}{\partial x_1} \frac{\partial T}{\partial x_1} + \frac{\partial C}{\partial x_2} \frac{\partial T}{\partial x_2} + C(\nabla^2 T) \right\} - \\ - \Pr \operatorname{Re}_* V(\xi) \frac{\partial T}{\partial x_1} \frac{1}{R_0} + \Pr \operatorname{Re}_* \operatorname{Ec}(\varphi + \psi) \frac{T_0}{R_0^2} \quad (17)$$

or which an approximate solution is to be sought. In order to obtain a specific solution for (17) the following boundary conditions need to be prescribed.

The temperature of the inlet water on boundary Γ_1 at $x_1 = 0$ is given as

$$T = T(x_1 = 0, x_2) = T_0 \quad (18)$$

The outflow of heat flux is zero

$$\frac{\partial T}{\partial x_1} - q_{FL} = 0, \qquad q_{FL} = 0 \qquad \text{on boundary } \Gamma_3 \text{ at } x_1 = \infty. \quad (19a)$$

There is heat transfer on boundary Γ_2 in the cylindrical surface $x_2 = R_0$:

$$P = P(T) = \frac{\partial T}{\partial x_2} \rfloor_{x_2 = R_0} + \frac{h}{\lambda} [T(x_1, R_0) - T_K] = 0, \quad (19b)$$

where T_K is the temperature of the environment, h is the heat convection coefficient (convective heat transfer coefficient).

According to the Galerkin variation principle [12, 13] the weak form of the boundary value problem is

$$\int_\Omega \delta T \Im(T) d\Omega + \int_{\Gamma_2} \delta T P(T) d\Gamma - \int_{\Gamma_3} \delta T C (\frac{\partial T}{\partial x_1} - q_{FL}) d\Gamma = 0, \quad (20)$$

where δT is the variation of the temperature field, which is zero on the boundary Γ_1, $\delta T = 0$.

Based on the product derivation rule

$$[\nabla \delta T \cdot C(\nabla T)] = (\nabla \delta T) \cdot C(\nabla T) + \delta T \left(\nabla C \right) \cdot (\nabla T) + \delta T C \left(\nabla^2 T \right). \quad (21)$$

Using the Gauss theorem

$$\int_\Omega \delta T C (\nabla^2 T) d\Omega = \int_{\Gamma_2 + \Gamma_3} \delta T C (\nabla T) \cdot \mathbf{n} d\Gamma - \int_\Omega \{ (\nabla \delta T) \cdot C(\nabla T) + \delta T \left(\nabla C \right) \cdot (\nabla T) \} d\Omega. \quad (22)$$

For boundary value problems (17)-(19), the Galerkin principle takes the following form:

$$\int_\Omega \delta T \left\{ \frac{1}{\lambda} \left[\frac{\partial \lambda}{\partial x_1} C \frac{\partial T}{\partial x_1} \right] + \frac{1}{\lambda} \left[\frac{\partial \lambda}{\partial x_2} C \frac{\partial T}{\partial x_2} \right] + \frac{\partial C}{\partial x_1} \frac{\partial T}{\partial x_1} + \frac{\partial C}{\partial x_2} \frac{\partial T}{\partial x_2} + C(\nabla^2 T) - \right. \\ \left. - \Pr \operatorname{Re}_* V(\xi) \frac{\partial T}{\partial x_1} \frac{1}{R_0} + \Pr \operatorname{Re}_* \operatorname{Ec}(\varphi + \psi) \frac{T_0}{R_0^2} \right\} d\Omega + \\ + \int_{\Gamma_2} \delta T \left[\frac{\partial T}{\partial x_2} + \frac{h}{\lambda} (T - T_K) \right] d\Gamma - \int_{\Gamma_3} \delta T C (\frac{\partial T}{\partial x_1} - q_{FL}) d\Gamma = 0. \quad (23)$$

Substituting (22) into (23) and using the following relation

$$\delta T(\nabla C)\cdot(\nabla T)=\delta T\left[\frac{\partial C}{\partial x_1}\frac{\partial T}{\partial x_1}+\frac{\partial C}{\partial x_2}\frac{\partial T}{\partial x_2}\right] \tag{24}$$

after some manipulations the final variational equation is

$$\begin{aligned}\int_\Omega\Big\{-\frac{\delta T}{\lambda}\left[\frac{\partial\lambda}{\partial x_1}C\frac{\partial T}{\partial x_1}\right]-\frac{\delta T}{\lambda}\left[\frac{\partial\lambda}{\partial x_2}C\frac{\partial T}{\partial x_2}\right]+(\nabla\delta T)C\cdot(\nabla T)+\\ +\delta T\,\mathrm{Pr}\,\mathrm{Re}_*\,V(\xi)\frac{\partial T}{\partial x_1}\frac{1}{R_0}\Big\}d\Omega-\int_{\Gamma_2}\delta T(1+C)\frac{\partial T}{\partial x_2}d\Gamma-\int_{\Gamma_2}\delta T\frac{h}{\lambda}Td\Gamma=\\ =\int_\Omega\delta T\,\mathrm{Pr}\,\mathrm{Re}_*\,\mathrm{Ec}(\varphi+\psi)\frac{T_0}{R_0^2}d\Omega-\int_{\Gamma_2}\delta T\frac{h}{\lambda}T_K d\Gamma+\int_{\Gamma_3}\delta TCq_{FL}d\Gamma.\end{aligned} \tag{25}$$

3. Approximation by finite element method

According to the finite element method [14, 15], the temperature field is approximated in the following form:

$$T=\mathbf{N}\mathbf{q},\qquad \frac{\partial T}{\partial x_1}=\mathbf{N}_{,x1}\mathbf{q},\qquad \frac{\partial T}{\partial x_2}=\mathbf{N}_{,x2}\mathbf{q}. \tag{26}$$

Here $\mathbf{N}$ is the matrix of shape functions, its derivatives are:

$$\frac{\partial}{\partial x_1}\mathbf{N}=\mathbf{N}_{,x1},\qquad \frac{\partial}{\partial x_2}\mathbf{N}=\mathbf{N}_{,x2}$$

and $\mathbf{q}$ is the vector of the unknown parameters. Hierarchical shape functions will be used in p-version finite elements [14].

In order to discretize functional (25) the following formulae should be evaluated:

$$\nabla T=\begin{bmatrix}\dfrac{\partial\mathbf{N}}{\partial x_1}\\[2mm] \dfrac{\partial\mathbf{N}}{\partial x_2}\end{bmatrix}=\begin{bmatrix}\mathbf{N}_{,x1}\\ \mathbf{N}_{,x2}\end{bmatrix}\mathbf{q}, \tag{27}$$

$$\nabla T\cdot\mathbf{n}=\frac{\partial T}{\partial x_1}n_{x1}+\frac{\partial T}{\partial x_2}n_{x2}=\left[\frac{\partial\mathbf{N}}{\partial x_1}n_{x1}+\frac{\partial\mathbf{N}}{\partial x_2}n_{x2}\right]\mathbf{q}=\mathbf{\Gamma}\mathbf{q}, \tag{28}$$

$$\begin{aligned}\delta\mathbf{q}^T\mathbf{K}\mathbf{q}=\delta\mathbf{q}^T\Bigg(\int_\Omega\left\{\left[\mathbf{N}_{,x1}^T\mathbf{N}_{,x2}^T\right]C\begin{bmatrix}\mathbf{N}_{,x1}\\ \mathbf{N}_{,x2}\end{bmatrix}+\mathrm{Pr}\,\mathrm{Re}_*\left[\mathbf{N}^TV\mathbf{N}_{,x1}\right]\frac{1}{R_0}\right\}d\Omega-\\ -\int_\Omega\mathbf{N}^T\frac{C}{\lambda}\left[\frac{\partial\lambda}{\partial x_1}\mathbf{N}_{,x1}+\frac{\partial\lambda}{\partial x_2}\mathbf{N}_{,x2}\right]d\Omega-\\ -\int_{\Gamma_2}\mathbf{N}^T\left[(1+C)\mathbf{N}_{,x2}+\frac{h}{\lambda}\mathbf{N}\right]d\Gamma\Bigg)\mathbf{q},\end{aligned} \tag{29}$$

$$\delta\mathbf{q}^T\mathbf{f}=\delta\mathbf{q}^T\left(\frac{T_0}{R_0^2}\int_\Omega\mathbf{N}^T\,\mathrm{Pr}\,\mathrm{Re}_*\,\mathrm{Ec}(\varphi+\psi)d\Omega-\int_{\Gamma_2}\mathbf{N}^T\frac{h}{\lambda}T_K d\Gamma+\int_{\Gamma_3}\mathbf{N}^TCq_{FL}d\Gamma\right). \tag{30}$$

The stiffness matrix $\mathbf{K}$ and the load vector $\mathbf{f}$ are produced by Gauss type numerical integration element by element. In order to evaluate the above expressions the fluid flow problem should be solved first, and accordingly the values of V, C, φ and ψ at these points are taken. The rest of the parameters are interpolated from Table 1, the Reynolds numbers can be taken from Figures 25 and 26 as a function of the fluid rate.

Due to arbitrary variation of $\delta\mathbf{q}$, the following algebraic equation system needs to be solved:

$$\mathbf{Kq} - \mathbf{f} = \mathbf{0}. \tag{31}$$

Its solution is given as

$$\mathbf{q} = \mathbf{K}^{-1}\mathbf{f}. \tag{32}$$

The temperature field is approximated by (26), the material constants are modified accordingly, then by the repeatedly calculated stiffness matrix $\mathbf{K}$ and load vector $\mathbf{f}$, equation (26) will be solved successively until the following tolerance has been met as far as the following inequality:

$$e_T = 100\frac{\sqrt{\sum_i (q_i^{(s)})^2} - \sqrt{\sum_i (q_i^{(s-1)})^2}}{\sqrt{\sum_i (q_i^{(s-1)})^2}} \leq 0.001, \tag{33}$$

where s is the number of iteration.

4. Numerical results

Let us examine the flow of water in a rigid pipe. The temperature is given at the inlet edge of the pipe. Our aim is to determine the frictional heat generation caused by the turbulent flow, which will affect the water temperature. The following questions can also be examined: How will the temperature change with different heat transfer parameters, and how will the volume flow rate Q affect the resulting temperature field? It is also a question whether the solution is sensitive to the diameter of the pipe, i.e., whether it is significant or not.

Let the reference temperature and the environment temperature be $T_0 = 373$ K and $T_K = 293$ K, respectively.

Material constants are independent of fluid velocity but depend on the temperature in the case of water as given in Table 1.

Table 1.

$T[^\circ C]$	0	20	100
$\rho\,[\mathrm{kg/m^3}]$	1002.28	1000.52	960.63
$c_p\ [J/(\mathrm{kgK})$	4118	4182	4216
$\upsilon = \eta/\rho\ [\mathrm{m^2/s}]$	1.788×10^{-6}	1.116×10^{-6}	2.94×10^{-7}
$\lambda\ [W/(\mathrm{mK})]$	0.552	0.597	0.680
Pr	13.369	7.821	1.751

In the solution process, first the functions $V(\xi)$ and $H(\xi)$ are determined by solving the fluid flow problem. The viscous and turbulent dissipations depend on these functions:

$$\varphi = \frac{R_0\varphi_D}{v_*^3} = \frac{1}{\mathrm{Re}_*}\left(\frac{dV}{d\xi}\right)^2, \qquad \psi = \frac{R_0\varepsilon}{v_*^3} = -\frac{\alpha+2\beta+\gamma}{4\,\mathrm{Re}_*\,H}\left(\frac{dH}{d\xi}\right)^2. \tag{34}$$

Dissipation leads to an increase in the temperature of the fluid. Two cases will be demonstrated here. Let us take two different pipe diameters (D) with the same flow rate Q. The results are shown in Figure 2.

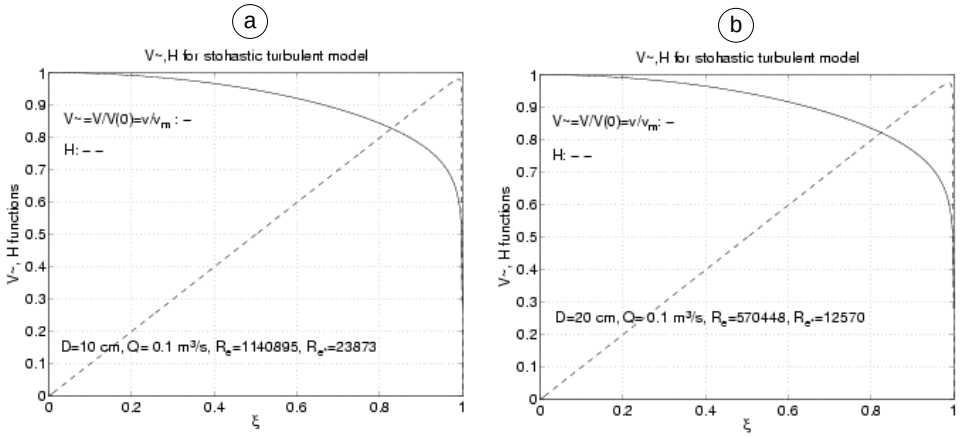

Figure 2. Functions $V^{\tilde{}}$ and H along the radius, a) $D = 0.1$m, b) $D = 0.2$ m

It can be seen that around the pipe wall ($x_2 \sim R_0,\ \xi \sim 1$), both functions change abruptly, since the heat development is significant there.

Let us consider the pressure distribution. The following equations for the pressure can be obtained by integrating differential equation (5a) using transformation $H(\xi) = \Theta/(\rho v_*^2)$ in it.

$$p^{\tilde{}}(\xi) - p_0^{\tilde{}} = \frac{p(\xi)}{\rho v_*^2} - \frac{p_0}{\rho v_*^2} = \left(\beta_* - \frac{2a^2}{3}\right) H + (\beta_* - \gamma_*) \int_0^\xi \frac{1}{\tilde{\xi}} H d\tilde{\xi} \tag{35a}$$

$$p(x_1, x_2) = A(x_2) + Bx_1 = p^{\tilde{}}\left(\frac{x_2}{R_0}\right) - \frac{\Delta p}{L} x_1. \tag{35b}$$

From Figure 26 at $Q = 0.1$ m^3/s, $v_a = 3.1831$ m/s, Reynolds numbers are Re $=$ 570448, $\mathrm{Re}_* = 12680$ and taking $D = 0.2$ m, it follows that

$$v_* = \frac{\mathrm{Re}_*\, v}{R} = \frac{12680 \times 1.116}{10^5} = 0.1415 \text{ m/s}.$$

Furthermore

$$\rho v_*^2 = 1000.52 \times 0.1415^2 = 20.03 \frac{\text{kg}}{\text{ms}^2} = 20.03 \text{ Pa} = 20.03 \times 10^{-5} \text{ bar}.$$

Pressure $\tilde{p}$ changes as shown in Figure 3a at $\tilde{p}=1$. If $p_0 > \rho v_*^2$ then the point ($\xi = 0$, $\tilde{p}(0) = 1$) shifts to a vertically higher position, and the function $\tilde{p}(\xi)$ will be parallel to the current situation.

Computations are repeated for pipes of $D = 0.1$m and $D = 0.3$m, obtaining the pressure distributions are shown in Figure 3b. For all the three different pipe diameters, the pressures are similar and they increase slightly at the vicinity of the wall. The larger the pipe diameter, the greater the rate of change $\Delta\tilde{p} = 1 - \tilde{p}(\xi = 1)$. The maximum rate of change of pressure with respect to its maximum value is $\sim 0.8(\rho v_*^2)$.

When the friction factor f for the pipe is known, the pressure loss can be calculated as follows [16]:

$$\Delta p = f\frac{L}{D}\frac{\rho}{2}v_a^2 = 8f\frac{L}{D^5\pi^2}\rho\, Q^2 \ \ [\text{Pa}]. \tag{36}$$

Taking a pipe of $D = 0.2$m and $f = 0.02$, the pressure drop for one meter length is

$$\Delta p = 8f\frac{L}{D^5\pi^2}\rho\, Q^2\ [\text{Pa}] = 8\times 0.02\frac{1}{0.2^5\pi^2}1000.52\times 0.1^2 = 506.87\ \text{Pa} = 0.0050687\ \text{bar}.$$

This means that the pressure drops are 5.068 bar for length L of 1 km, 25.34 bar for 5 km and 50.68 bar for 10 km, resp.

The supply pressure is determined by the pressure drop along the pipe. For smaller diameters, its value increases significantly, which will affect the performance of the pump used.

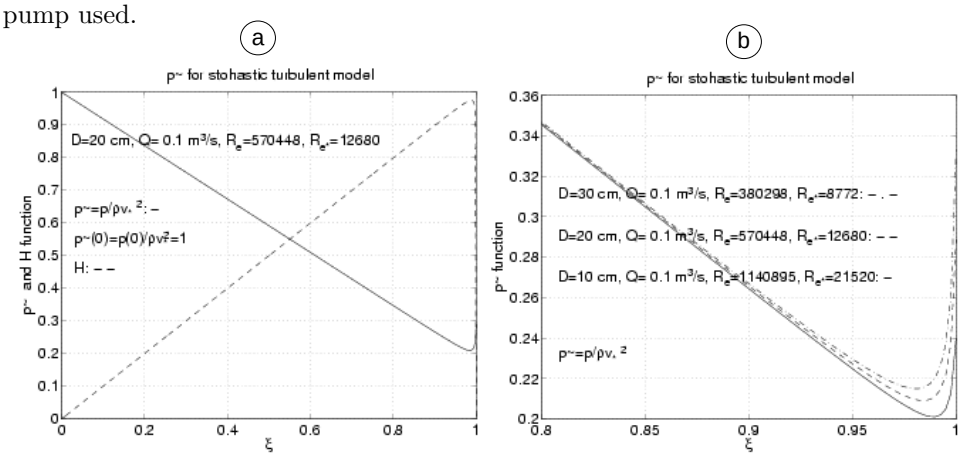

Figure 3. $\tilde{p}(\xi)$ pressure at$\tilde{p}(0) = 1$, a) along the radius, b) in the vicinity of the pipe wall

4.1. **Examination of a five kilometer long pipe.** If the diameter of the pipe is $D = 0.2$m and its length is 5 km, the corresponding finite element mesh is indicated in the figures for temperature. Thin lines that appear for each element correspond to coordinate lines passing through Gaussian (Lobatto) numerical integration points. The polynomial order of each element is $p = 8$. The elements applied are ring elements, which are suitable for describing axially symmetrical relationships. Small elements were taken to better approximate the flow in the boundary layer

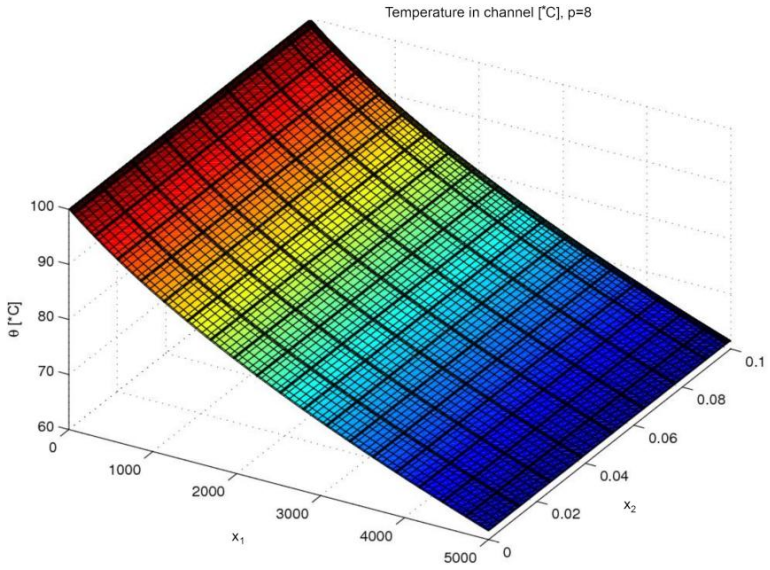

Figure 4. Resulting temperature distribution at $R_0 = 0.1$ m, $Q = 0.009$ m^3, $h = 7.71$ W/(m^{2}K)

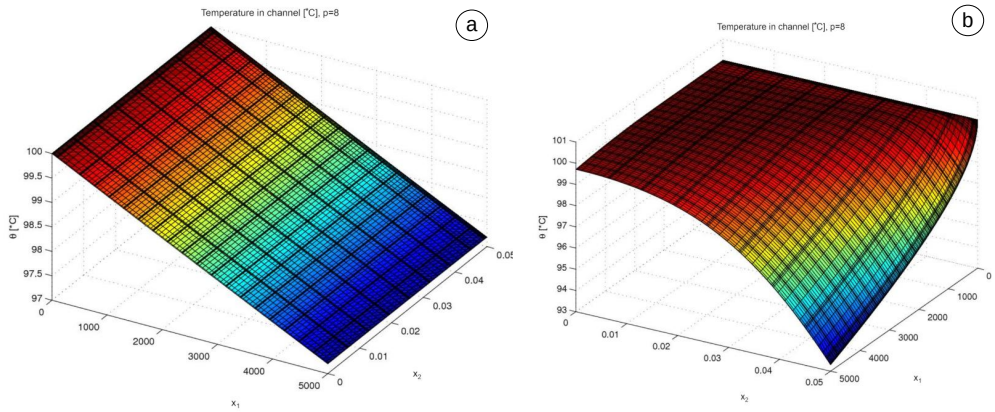

Figure 5. Resulting temperature for parameters $Q = 0.03$ m^3/s, $h = 2.22$ W/(m^{2}K), a) in case of turbulent flow (with heat generation), b) without heat generation for diameter $D = 0.1$m

near the edge $x_2 = R_0$. The same dense mesh is applied in the direction of the longitudinal axis at the entry cross-section.

Figures 25 and 26 show flows of fluids Q [m^3/s], with average velocity v_a[m/s], and the Reynolds number Re depending on the radius R_0 of the pipe and the Re$_*$ number.

Temperature changes are computed for two different convective heat transfer coefficients h [W/(m^{2}K)] and for parameters $R_0 = 0.1$ m, $Q = 0.009$ m^3/s, $h = 7.71$ W/(m^{2}K), shown in Figure 5. In Figure 6 the temperature of the fluid is shown in turbulent flow under parameters: $R_0 = 0.1$ m, $Q = 0.04$ m^3/s, $h = 2.22$ W/(m^{2}K) with and without frictional heat generation. The length of the pipe is 5000 m. In all figures temperature T is denoted by θ.

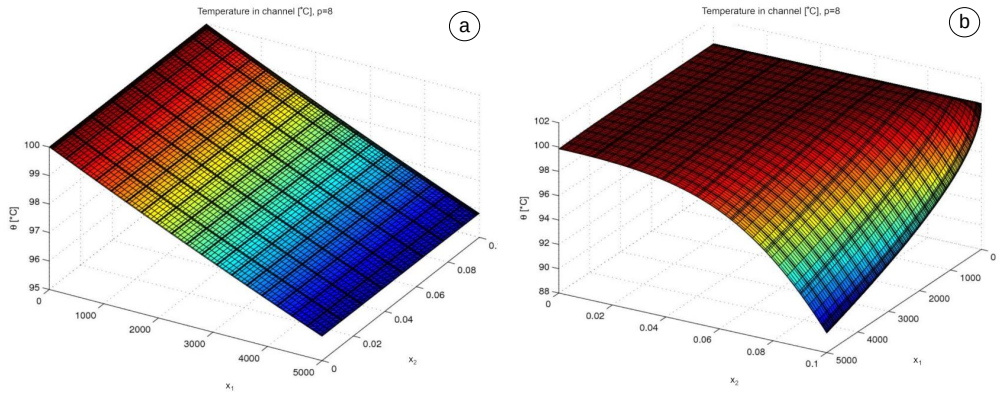

Figure 6. Resulting temperature for parameters $Q = 0.04$ m^3/s, $h = 2.22$ W/(m^{2}K), a) in case of turbulent flow (with heat generation), b) without heat generation for diameter $D = 0.2$m

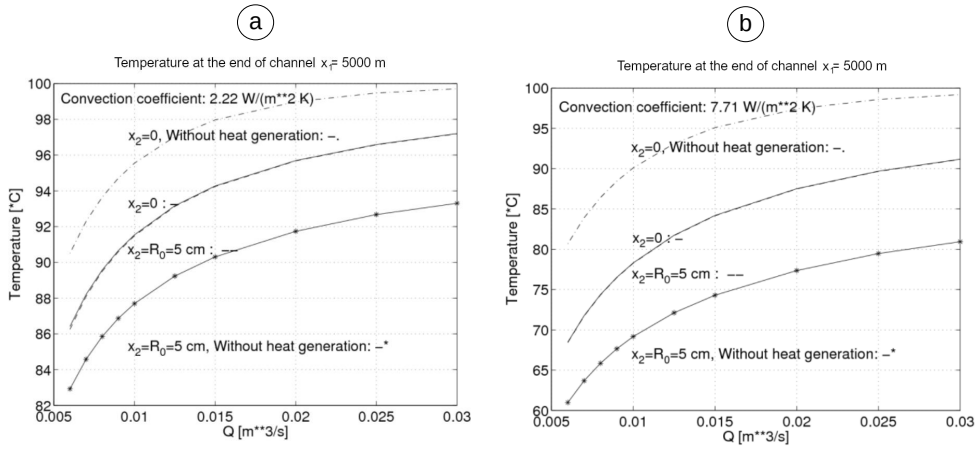

Figure 7. Temperature distributions in the case of pipe radius $R_0 = 0.05$ m, as a function of volume current Q (-,–) with and without heat generation (-*,–); a) $h = 2.22$ W/(m^{2}K), b) $h = 7.71$ W/(m^{2}K)

It is very clear that in computations without heat generation, the temperature changes along the radius of the pipe are significant, and the heat losses along the length are much greater than in cases of frictional internal heat generation resulting

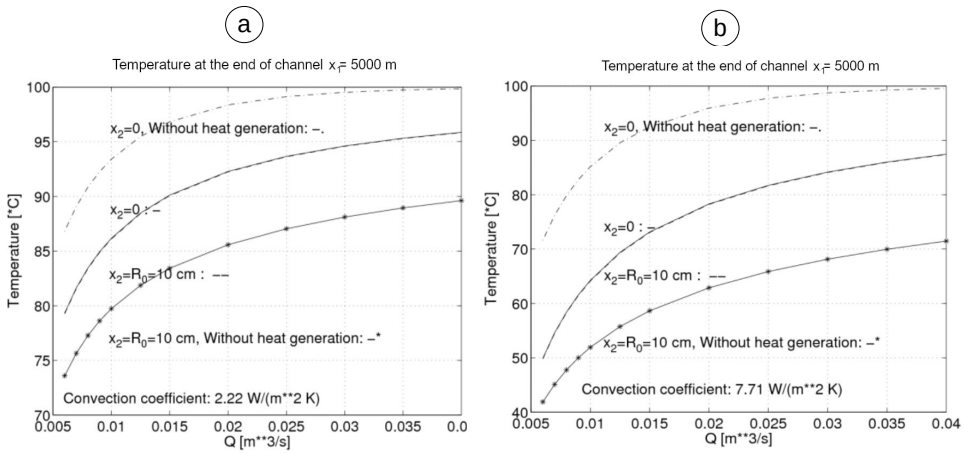

Figure 8. Temperature distributions in the case of pipe radius $R_0 = 0.01$ m, as a function of volume current Q (-,–) with heat generation, and for cases without heat generation (-*,–); a) $h = 2.22$ W/(m^{2}K), b) $h = 7.71$ W/(m^{2}K)

from the turbulence. Therefore, turbulence reduces the cooling of the water flowing in the pipe; the higher the Reynolds number, the smaller the heat loss. It can also be seen that the value of the heat transfer factor significantly affects the temperature that develops. The high-efficiency thermal insulation of the pipe is very important in order to provide the water temperature at the end of the transmission line that is desired for heating.

Summarizing the computational results, in Figures 7 and 8, at the center of the pipe $x_2 = 0$, and at the outer radius of the pipe $x_2 = R_0$ curves are denoted with (-) continuous, (–) dashed curves for turbulent flow, resp., while curves (-*) and (-.) are associated with the case without heat generation. The temperatures are evaluated at the cross-section points at the end of a pipe section $x_1 = 5000$ m. The higher the flow rate Q, the less water will cool along the length of the pipe.

4.2. **Analyses of pipes with lengths of ten and fifteen kilometers without heat generation.**

4.2.1. *Temperature in a ten kilometer long pipe:*

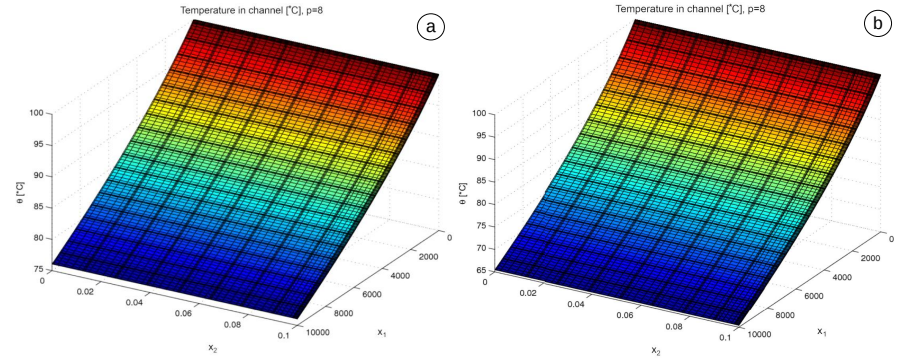

Figure 9. Temperature that develops for a) $Q = 0.01$ m^3, b) $Q = 0.006$ m^3 at $D = 0.2$ m if $h = 2.22$ W/(m^{2}K), $L = 10$ km

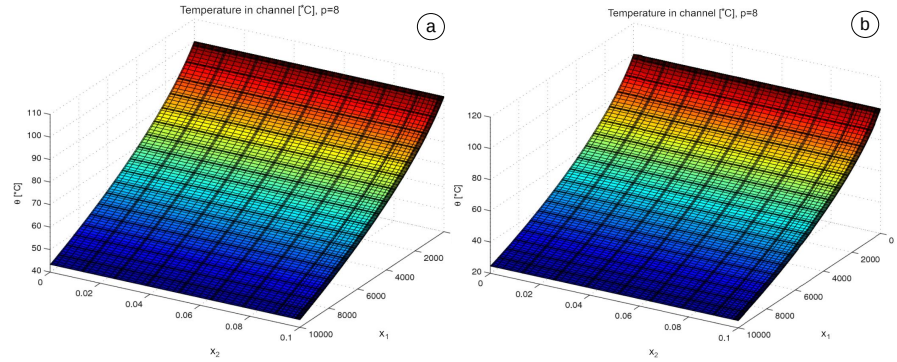

Figure 10. Temperature that develops for a) $Q = 0.01$ m^3, b) $Q = 0.006$ m^3 at $D = 0.2$ m if $h = 7.71$ W/(m^{2}K), $L = 10$ km

4.2.2. *Temperature in a fifteen kilometer long pipe:*

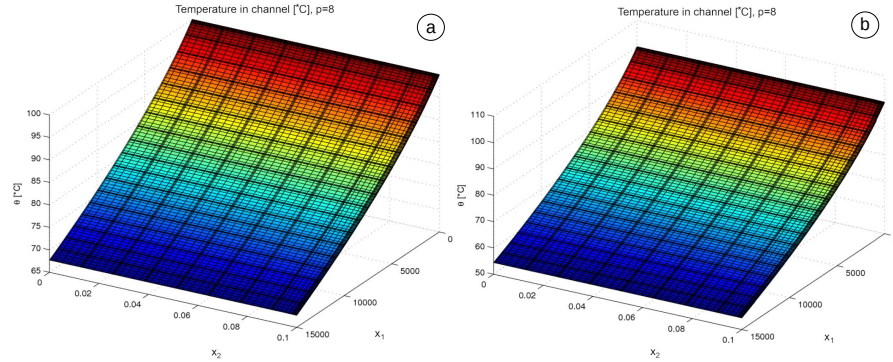

Figure 11. Temperature that develop for a) $Q = 0.01$ m^3, b) $Q = 0.006$ m^3 at $D = 0.2$ m if $h = 2.22$ W/(m^{2}K), $L = 15$ km

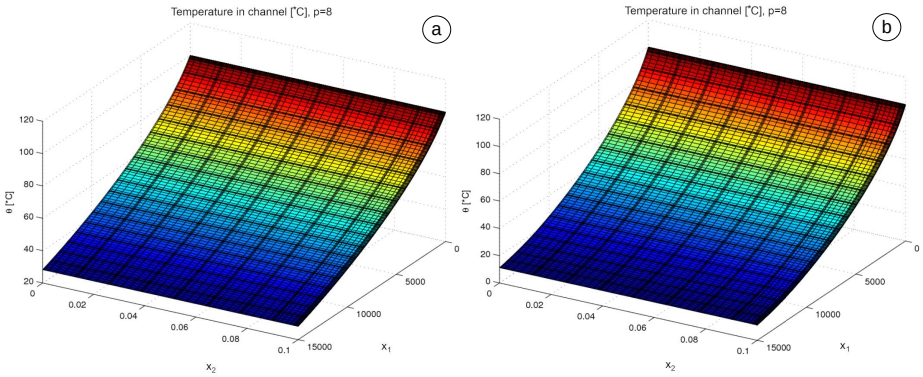

Figure 12. Temperature that develops for a) $Q = 0.01$ m^3, b) $Q = 0.006$ m^3 at $D = 0.2$ m if $h = 7.71$ W/(m^{2}K), $L = 15$ km

4.2.3. *Temperature in a twenty kilometer long pipe:*

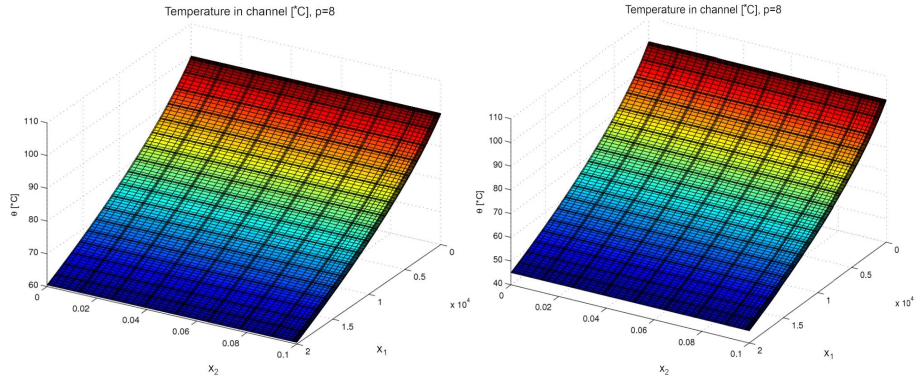

Figure 13. Temperature that develops for a) $Q = 0.01$ m^3, b) $Q = 0.006$ m^3 at $D = 0.2$ m if $h = 2.22$ W/(m^{2}K), $L = 20$ km

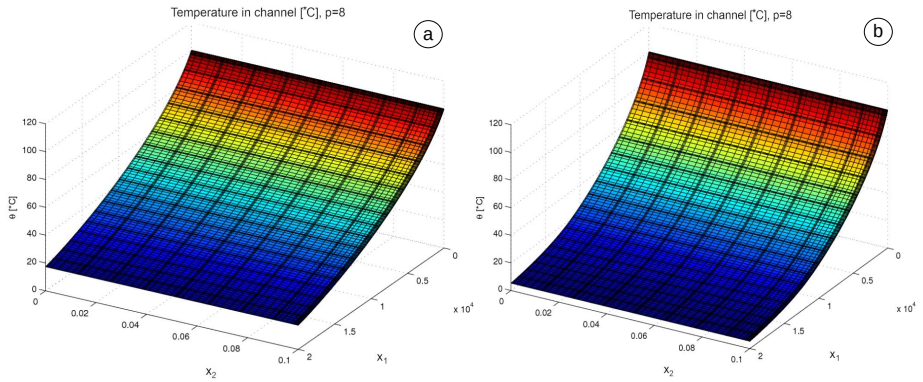

Figure 14. Temperature that develops for a) $Q = 0.01$ m^3, b) $Q = 0.006$ m^3 at $D = 0.2$ m if $h = 7.71$ W/(m^{2}K), $L = 20$ km

Figures 9-14 show the temperature distributions obtained in some of the numerous cases examined.

Figure 15 shows the temperature for pipe diameter $D = 0.1$ m for different heat transfer factors. Figure 16 demonstrates that for a low-value of volume flow rate Q heat loss is very significant, especially for larger $h = 7.71$ W/(m^{2}K). For $Q = 0.006$ m^3, the water has practically taken on the temperature of the environment already at $x_1 = 10$ km distance.

For the larger diameter $D = 0.2$ m the results are more favorable as regards the cooling process (see Figure 16), but the cooling of the water will be significant for a small value of Q. Here the case without heat generation is also indicated. The effect of heat generation is noticeable. For example with $Q = 0.035$ m^3/s, the temperature is about 7 $^\circ C$ higher at the output cross-section of the pipe than for a non-heat generation assumption (see Figure 16a, b). The same can also be seen for $Q = 0.1$ m^3/s (see Figure 16c, d).

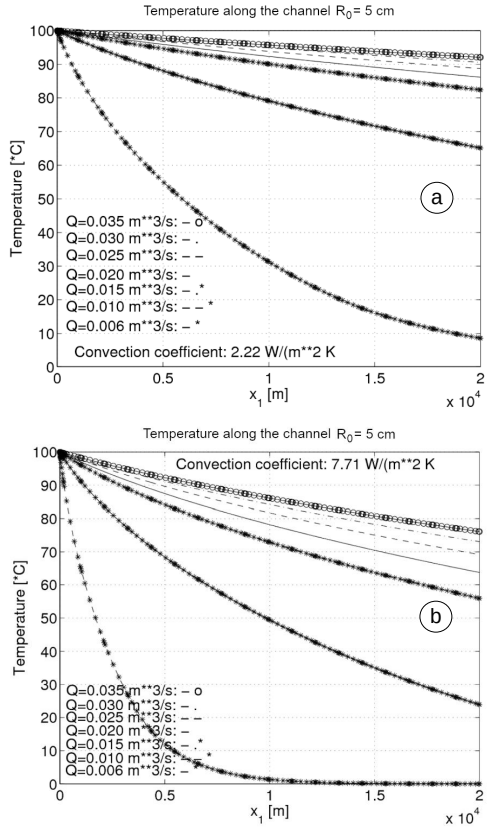

Figure 15. Temperature distribution at the edge of a pipe ($x_2 = R_0$) for different Q values if diameter is $D = 0.1$ m and the pipe length is $L = 20$ km, and there is no heat generation, a) $h = 2.22$ W/(m^{2}K), b) $h = 7.71$ W/(m^{2}K)

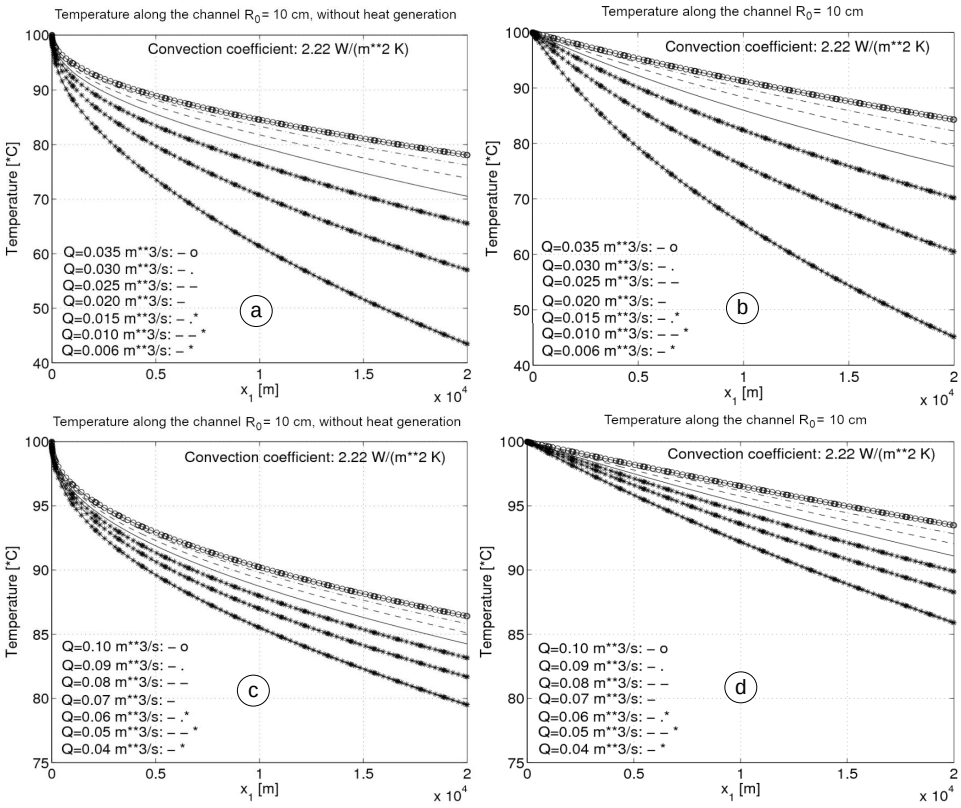

Figure 16. Temperature distribution at the edge of a pipe ($x_2 = R_0$) for different Q values if $D = 0.2$ m, $L = 20$ km; a) and c) without heat generation b) and d) with heat generation

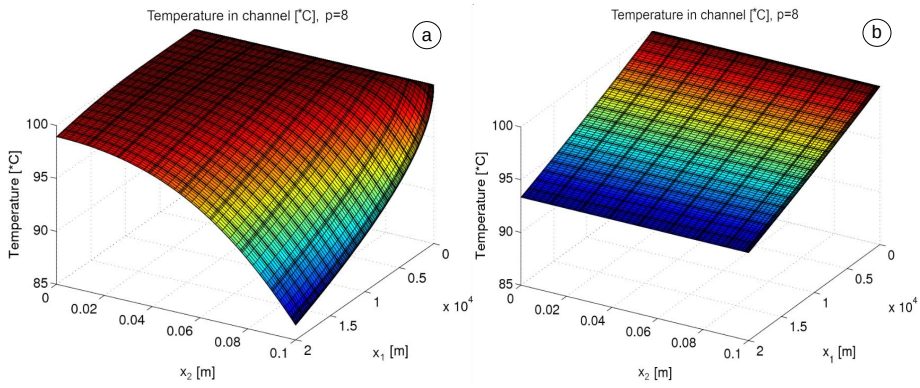

Figure 17. Temperature that develops for $Q = 0.1$ m^3 at $D = 0.2$ m if $h = 2.22$ W/(m^{2}K); a) without heat generation b) with heat generation

Figure 17 shows the temperature distribution for values of $Q = 0.1$ m^3 and $h = 2.22$ W/(m^{2}K). The results obtained for higher $h = 7.71$ W/(m^{2}K) are shown in Figure 19.

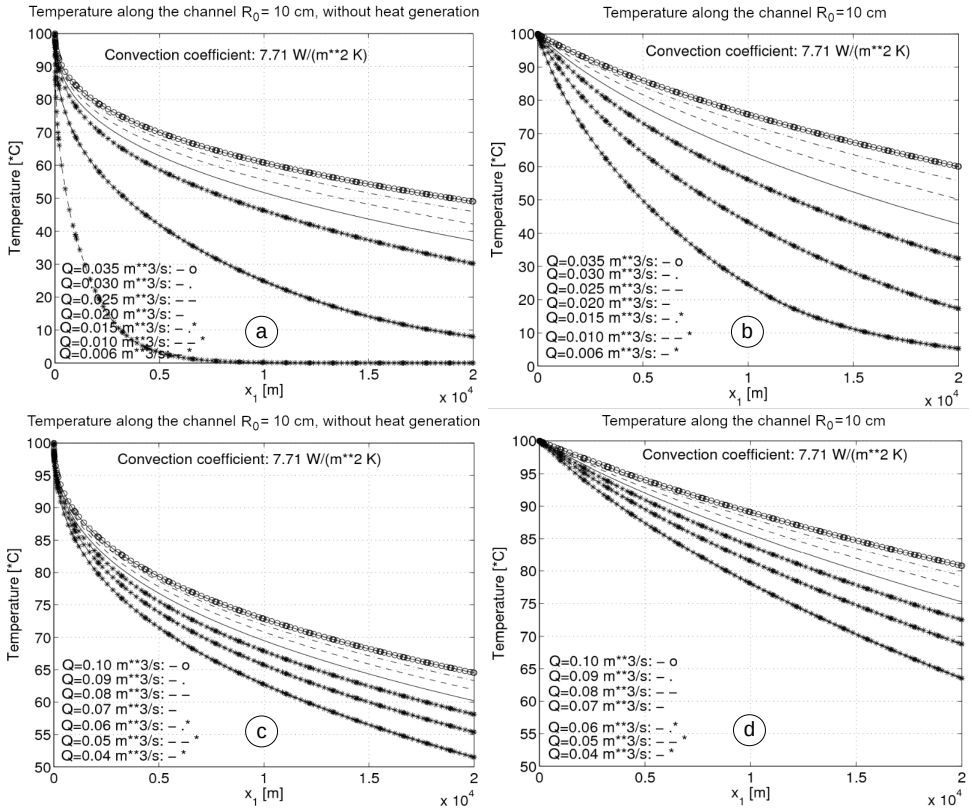

Figure 18. Temperature distribution at the edge of a pipe ($x_2 = R_0$) for different Q values if $D = 0.2$ m, $L = 20$ km; a)c) without heat generation b)d) with heat generation

As noted above, the higher the velocity of the water, the less it cools down. Figure 19 shows the temperature distribution for values of $Q = 0.1$ m^3 and $h = 7.71$ W/(m^{2}K).

We can get an illustrative picture of how the final cross-sectional pipe wall temperature changes as a function of the parameters Q and v_a depending on the two heat transfer factors $h = 2.22$ W/(m^{2}K) and $h = 7.71$ W/(m^{2}K) (see Figure 20). For $h = 7.71$ W/(m^{2}K) , the pipe wall temperature changes will be small above certain values of Q or v_a.

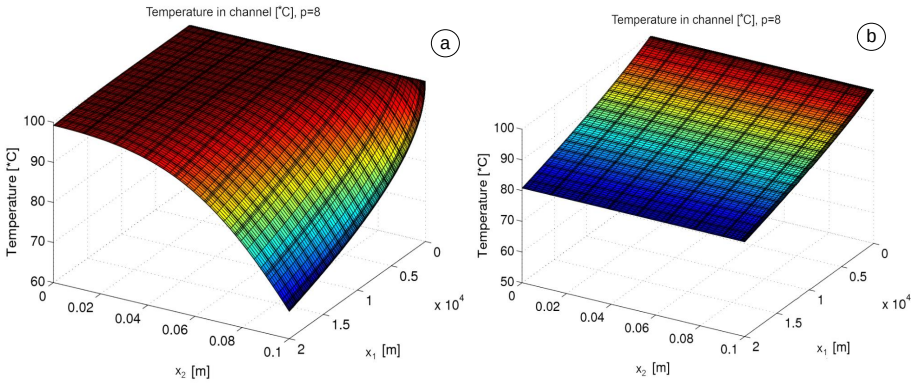

Figure 19. The resulting temperature for parameters $Q = 0.1$ m^3, $h = 7.71$ W/(m^{2}K); at $D = 0.2$ m a) without heat generation b) with heat generation

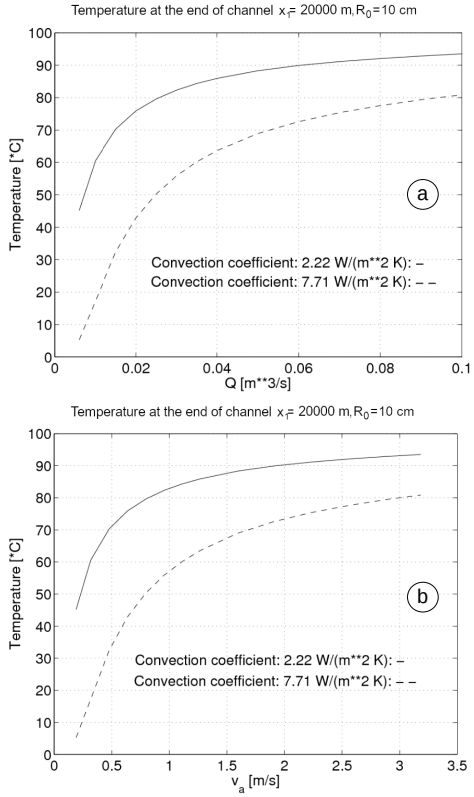

Figure 20. The resulting temperature at the boundary ($x_2 = R_0$) of the cross section $x_1 = 20$ km for parameters $h = 2.22$ W/(m^{2}K), $h = 7.71$ W/(m^{2}K), $D = 0.2$ m a) as a function of Q b) as a function of v_a [m/a]

Finally, performing the computations for a pipe with a diameter of $D = 0.3$ m, the results are shown in Figures 21-24.

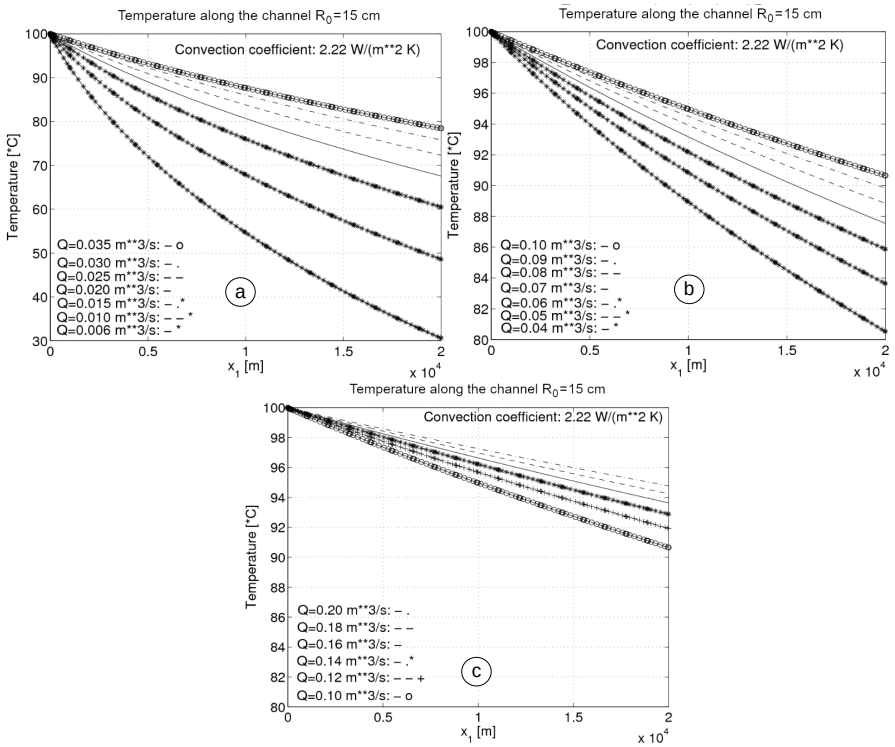

Figure 21. Temperature distribution at the edge of a pipe with turbulent flow for different Q values for diameter $D = 0.3$ m and pipe length $L = 20$ km; $h = 2.22$ W/(m^{2}K) with heat generation taken into account

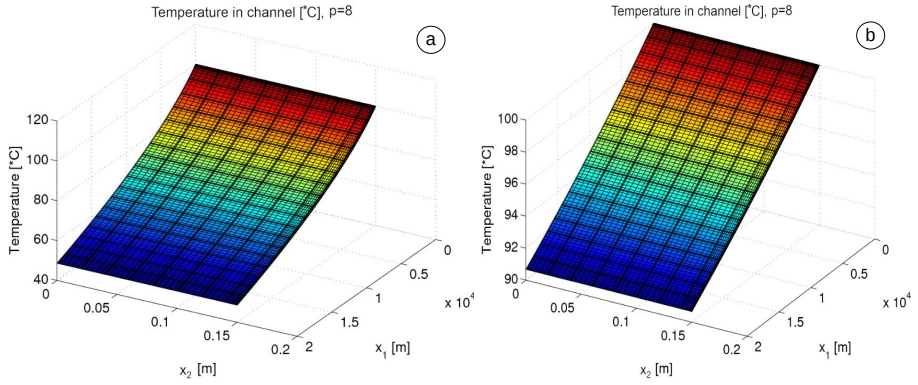

Figure 22. Temperature distribution obtained with heat generation for turbulent flow for parameter $h = 2.22$ W/(m^{2}K), in the case of diameter $D = 0.3$ m; a) $Q = 0.01$ m^3, b) $Q = 0.1$ m^3

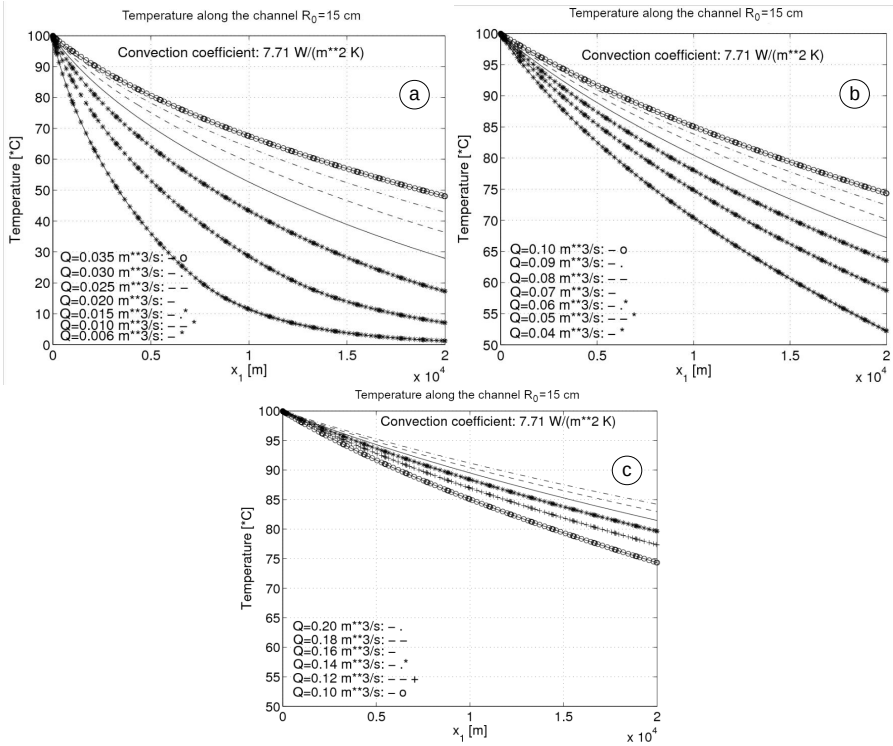

Figure 23. Temperature distribution at the edge of a pipe with turbulent flow for different Q values for diameter $D = 0.3$ m and pipe length $L = 20$ km ; $h = 7.71$ W/(m^{2}K) with heat generation taken into account

4.3. **Comparison.** The computed temperature results obtained for the same flow rate $Q = 0.1$ m^3/s but for different pipe diameters D are given in Table 2. Comparing the temperatures for different diameters the following can be stated: the greater the diameter, the higher the temperature drop for different values of h.

Table 2.

	D [cm]	$T(x_1 = 10)$ km	$T(x_1 = 20)$ km
$h = 2.22$ W/(m^{2}K)	$D = 20$ [cm]	96.5	93
	$D = 30$ [cm]	95	91
$h = 7.71$ W/(m^{2}K)	$D = 20$ [cm]	89	82
	$D = 30$ [cm]	85	74

The longer the pipe, the lower the temperature of the fluid at the end of the tube, and the slower the flow rate (i.e., Q is small), the greater the loss due to the heat transfer between the pipe and the environment. In this case, the fluid cools down significantly (see Figures 18b, 21a, and 23a). As Q increases, the temperature function $T(x_1, R_0)$ decreases virtually linearly along the length of the pipe. These results are consistent with practical, engineering experience.

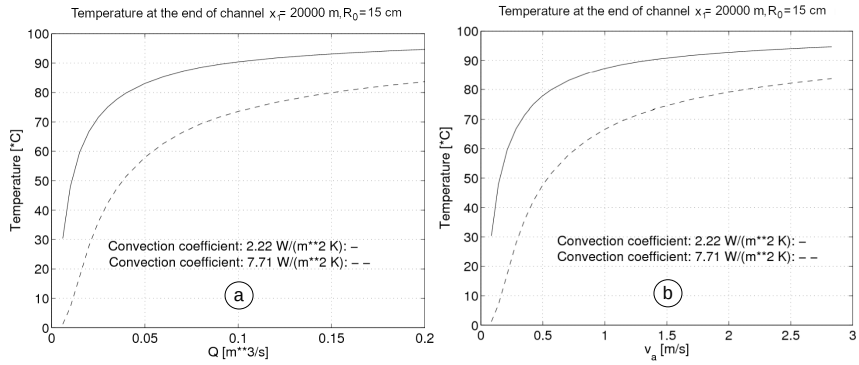

Figure 24. The resulting temperature at $x_1 = 20$ km in the boundary $x_2 = 20$ km for parameters h, $D = 0.3$ m a) depending on Q. b) depending on the average velocity v_a [m/s]

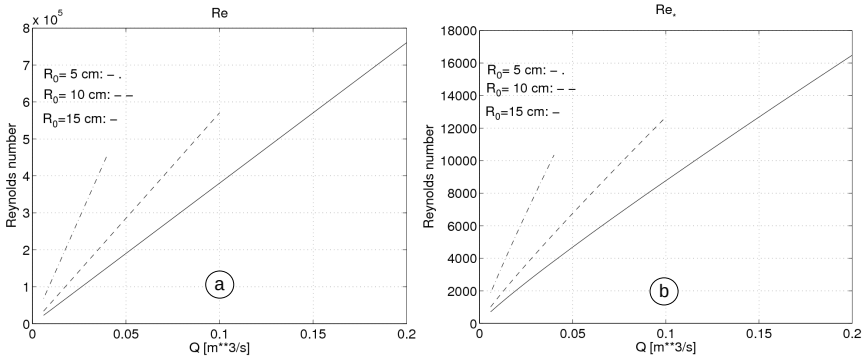

Figure 25. Functions a) for Reynolds number, b) for Re_* depending on the flow rate Q of the current for different pipe diameters

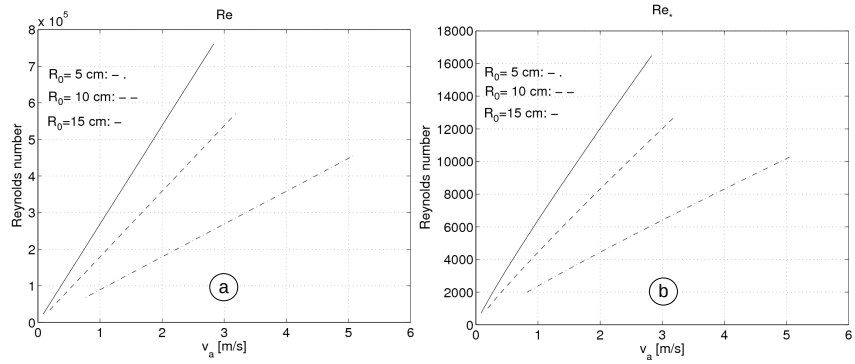

Figure 26. Functions a) for Reynolds number, b) for Re_* depending on the average velocity v_a [m/s] of the current for different pipe diameters

4.4. **Reliability of the FEM computations.** It is important to be aware of the error in the computations presented. A comprehensive analysis of the issue can be found in [14]. A relatively simple way to do this is to check the accuracy of the computed boundary conditions. The accuracy of the solution is expressed by the extent to which the boundary conditions are satisfied. In this aspect, the tests will be performed below. On the surface we will check the fulfillment of the boundary condition.

Let us begin with the heat transfer boundary condition on (see (19b)):

$$-\left.\frac{\partial T}{\partial x_2}\right|_{x_2=R_0} = \frac{h}{\lambda}\left[T(x_1,R_0)-T_K\right]. \tag{37}$$

Taking the derivative in the direction $y = R_0 - x_2$, the following equation is obtained

$$\left.\frac{\partial T}{\partial y}\right|_{y=0} = \frac{h}{\lambda}\left[T(x_1,R_0)-T_K\right]. \tag{38}$$

Let us define the following dimensionless quantities

$$T^* = \frac{T-T_K}{T_{y=0}-T_K}, \qquad y^* = y/(2R_0). \tag{39}$$

Using them, the heat transfer coefficient can be expressed as

$$h = \frac{\lambda}{T_{y=0}-T_K}\left.\frac{\partial T}{\partial y}\right|_{y=0} = \lambda\frac{T_{y=0}-T_K}{T_{y=0}-T_K}\frac{1}{2R_0}\frac{\partial T^*}{\partial y^*} = \left.\frac{\lambda}{2R_0}\frac{\partial T^*}{\partial y^*}\right|_{y^*=0} \tag{40}$$

from which the Nusselt number can be defined [17, 18]

$$\mathrm{Nu} = \frac{h2R_0}{\lambda} = \left.\frac{\partial T^*}{\partial y^*}\right|_{y^*=0}. \tag{41}$$

The derivative $\partial T^*/\partial y^*|_{y^*=0}$ can be calculated from the FEM solution, and on the other hand, its value $h2R_0/\lambda$ is easy to obtain. The difference between these values provides a piece of information about the errors of the FEM computations.

A concrete example is taken for turbulent flow without heat generation (see Temperature distribution in Figure 17a). The derivative is evaluated in the section $x_1 = 20$ km.

Using the difference method, the derivative $\partial T^*/\partial y^*|_{y^*=0} = 0.7$. The formula $h2R_0/\lambda$ can be calculated using the interpolation of λ in Table 1:

$$\lambda(80\,^\circ C) = 0.665\,\mathrm{W/(m^2K)}.$$

Then its value

$$\frac{h2R_0}{\lambda} = \frac{2.22 * 0.2}{0.665} = 0.667.$$

Finally, the error is

$$e_{Nu} = \frac{0.7-0.667}{0.667}100\% \approx 5\%,$$

which confirms that the solution is fairly good. Similar errors are obtained for the other solutions as well.

5. Conclusions

A thermal convection-diffusion problem is investigated based on the turbulence model developed by Professor Czibere [1–3], which is solved for pipelines by the finite element approximation method in this paper. High-precision results can be obtained with the chosen p-version finite elements [12]. The program developed is well suited for flow and thermal design of pipelines. Using the computer program developed, the computations can be performed at great speed using the actual geometrical and material data. The results, i.e., radial and longitudinal distributions of temperature, are displayed graphically, which helps the designer to consider the effects of the selected diameter D of the pipe, the flow rate Q, and the heat transfer constant h in order to analyze the implementation costs of the pipeline.

Acknowledgement. The present research was partly supported by the Hungarian Academy of Sciences and the SROP-4.2.1.B-10/2 / KONV-2010-0001 program. The author would like to thank Professor Tibor Czibere for raising the research topic of the article and also for permission to use a computer program suitable for the computation of turbulent flow in a pipe. His helpful discussion of the introductory part of the paper and the computed results is also acknowledged

Nomenclature

Latin notations

c_P special heat at constant pressure [J/(kgK)]
D diameter of the pipe
$\mathrm{Ec} = \mathrm{v}_*^2/(\mathrm{c_P T_0})$ Eckert number
f friction factor
h convective heat transfer coefficient [W/(m^{2}K)]
$\mathbf{H}$ and $\mathbf{H}*$ similarity tensor and its deviator
$\mathbf{G}$ eddy viscosity tensor
$\mathbf{g}$ acceleration due to gravity [m/s^2]
$k = \frac{1}{2}\overline{(\mathbf{v}' \cdot \mathbf{v}')} = a^2(\kappa l\Omega)^2 = a^2\Theta/\rho$ turbulent kinetic energy [m^2/s^2]
l length scale of turbulence [m]
$l\Omega$ velocity scale of turbulence [m/s]
p pressure [Pa]
Δp pressure drop [Pa]
$\mathrm{Pr} = \eta \mathrm{c_P}/\lambda$ Prandtl number
R_0 inner radius
Re Reynolds number
$\mathrm{Re}_* = v_* R_0/\upsilon$ factor
Q volume flow rate [m^3/s]
t time [s]
T absolute temperature [K]
T_0 reference temperature [K]
T_K temperature of the environment [K]
$\mathbf{v}$ velocity vector with components v_1, v_2, v_3 [m/s]
$\mathbf{v}'$ velocity vector for turbulent fluctuations [m/s]

v_* wall friction velocity [m/s]
v_a average velocity [m/s]
x_1, x_2, x_3 coordinates in the computation coordinate system

Greek notations
α, β, γ parameters in $\mathbf{H}$ similarity tensor
$\varepsilon = \upsilon\,(\mathbf{v}' \circ \nabla) : (\mathbf{v}' \circ \nabla + \nabla \circ \mathbf{v}') = -\upsilon \dfrac{\alpha+2\beta+\gamma}{4\rho\Theta} \left(\dfrac{d\Theta}{dx_2}\right)^2$ turbulent dissipation [$\mathrm{m}^2/\mathrm{s}^2$]
η dynamic viscosity [Pa]
$\Theta = \rho(\kappa l \Omega)^2$ dominant turbulent shear stress [Pa]
$\kappa = 0.407$ Kármán constant
$\kappa_* = 0.47$
λ thermal conductivity [W/(mK)]
$\Lambda = \rho c_P \kappa \kappa_* l^2 \Omega$ turbulent thermal conductivity [W/(mK)]
$\upsilon = \eta/\rho$ kinematic viscosity [$\mathrm{m}^2/\mathrm{s}^2$]
ρ density of the fluid [kg/m^3]
$\varphi_D = \upsilon\,(\mathbf{v} \circ \nabla) : (\mathbf{v} \circ \nabla + \nabla \circ \mathbf{v}) = \upsilon \left(\dfrac{dv_1}{dx_2}\right)^2$ viscous dissipation [$\mathrm{m}^2/\mathrm{s}^3$]
$\phi = \dfrac{R\phi_D}{v_*^3} = \dfrac{1}{\mathrm{Re}_*} \left(\dfrac{dV}{d\xi}\right)^2$ function for modified viscous dissipation [$\mathrm{m}^2/\mathrm{s}^3$]
$\psi = \dfrac{R\varepsilon}{v_*^3} = -\dfrac{\alpha+2\beta+\gamma}{4\,\mathrm{Re}_*\,H} \left(\dfrac{dH}{d\xi}\right)^2$ function for modified turbulent dissipation [$\mathrm{m}^2/\mathrm{s}^3$]
$\Omega = \nabla \times \mathbf{v}$ vortex vector [1/s]
$|\Omega = \nabla \times \mathbf{v}|$ absolute value of the vortex vector [1/s]

Dimensionless quantities
$H(\xi) = \dfrac{\Theta}{\rho v_*^2}$
$V(\xi) = \dfrac{v_1}{v_*}$
$\vartheta = \dfrac{T}{T_0}$
$\xi = \dfrac{x_2}{R}$

References

1. T. Czibere. "Three dimensional stochastic model of turbulence." *Journal of Computational and Applied Mechanics,* **2**(1), (2001), pp. 7–20. URL: `http://www.mech.uni-miskolc.hu/jcam/`.
2. T. Czibere. "Calculating turbulent flows based on a stochastic model." *Journal of Computational and Applied Mechanics,* **7**(2), (2006), pp. 155–188. URL: `http://www.mech.uni-miskolc.hu/jcam/`.

3. T. Czibere. *Transport theory solution of the turbulent flow problem based on the stochastic turbulence model.* in Hungarian. Report. University of Miskolc, Hungary, 2012. 37 pp.
4. N. Reddy and D. K. Gartling. *The Finite Element Method in Heat Transfer and Fluid Dynamics.* CRC Press, 1994. Chap. 8.2. 524 pp.
5. M. Griebel, T. Dornsheifer, and T. Neunhoeffer. *Numerical Simulation in Fluid Dynamics. A Practical Introduction.* Society for Industrial and Applied Mathematics, 1998. Chap. 10. xvi + 208. DOI: 10.1137/1.9780898719703.
6. T. J. Chung. "Applications to Turbulence." *Computational Fluid Dynamics.* Cambridge University Press, 2002, 679–723. DOI: 10.1017/CBO9780511606205.027.
7. Ferziger J. H. and M. Perić. "Turbulent Flows." *Computational Methods for Fluid Dynamics.* Springer, 2002, pp. 265–307. DOI: 10.1007/978-3-642-56026-2_9.
8. O. C. Zienkiewicz, R. L. Taylor, and P. Nithiarasu. "Turbulent Flows." *The Finite Element Method for Fluid Dynamics.* 7th ed. Butterworth-Heinemann, 2013. Chap. 8.
9. F. Moukalled, L. Mangani, and M. Darwish. *The Finite Volume Method in Computational Fluid Dynamics: An Advanced Introduction with OpenFOAM® and Matlab.* Fluid Mechanics and Its Applications 113. Springer, 2016. XXIII, 791. DOI: 10.1007/978-3-319-16874-6.
10. S. Rodriguez. *Applied Computational Fluid Dynamics and Turbulence Modeling: Practical Tools, Tips and Techniques.* Springer, 2019. DOI: 10.1007/978-3-030-28691-0.
11. D. A. Anderson, J. C. Tannehill, R. H. Pletcher, M. Ramakanth, and V. Shankar. *Computational Fluid Mechanics and Heat Transfer.* 4th ed. Computational and Physical Processes in Mechanics and Thermal Sciences. CRC Press, 2021. Chap. 5. DOI: 10.1201/9781351124027.
12. L. Brand. "The Pi theorem of dimensional analysis." *Archive for Rational Mechanics and Analysis,* **1**, (1957), pp. 35–45. DOI: 10.1007/BF00297994.
13. H. L. Langhaar. *Dimensional Analysis and Theory of Models.* John Wiley & Sons, 1951.
14. B. Szabó and I. Babuska. *Introduction to Finite Element Analysis: Formulation, Verification and Validation.* John Wiley & Sons, 2011. DOI: 10.1002/9781119993834.
15. Klaus-Jürgen Bathe. *Finite Element Procedures.* Prentice–Hall, Englewood Cliffs, New Jersey, 1996.
16. Á. G. Pattantyús: *Operation of machines (A gépek üzemtana in Hungarian).* Műszaki Kiadó, Budapest, 1983. Chap. 3.
17. W. M. Rohsenow, J. R. Hartnett, and Y. I. Cho. *Handbook of Heat Transfer.* 3rd ed. McGraw-Hill, New York, 1998. Chap. 1 and 5. URL: https://www.accessengineeringlibrary.com/content/book/9780070535558.
18. F. P. Incropera and D. P. DeWitt. *Fundamentals of Heat and Mass Transfer.* 4th ed. John Wiley & Sons, New York, 1996. Chap. 6.

Journal of Computational and Applied Mechanics, Vol. 16, No. 2, (2021), pp. 159–172
DOI: 10.32973/jcam.2021.009

A COMPARATIVE STUDY OF URANS, DDES AND DES SIMULATIONS OF JETSTREAM 31 AIRCRAFT NEAR THE COMPRESSIBILITY LIMIT

Hrishabh Chaudhary
Centre for Computational Engineering Sciences, Cranfield University,
Cranfield, Bedfordshire, MK43 0AL, United Kingdom
hrishabh.chaudhary@cranfield.ac.uk

Nicolas Ledos
Centre for Computational Engineering Sciences, Cranfield University,
Cranfield, Bedfordshire, MK43 0AL, United Kingdom
nicolas.ledos@cranfield.ac.uk

László Könözsy
Centre for Computational Engineering Sciences, Cranfield University,
Cranfield, Bedfordshire, MK43 0AL, United Kingdom
laszlo.konozsy@cranfield.ac.uk

[Received: October 21, 2021; Accepted: November 19, 2021]

Dedicated to Professor Tibor Czibere on the occasion of his 90th birthday

Abstract. This work presents a comparative study of Unsteady Reynolds–Averaged Navier–Stokes (URANS), Detached Eddy Simulations (DES) and Delayed Detached Eddy Simulations (DDES) turbulence modeling approaches by performing numerical investigation with the ANSYS-FLUENT software package on a full-scale model of the Jetstream 31 aircraft. The lift and drag coefficients obtained from different models are compared with flight test data, wind tunnel data and theoretical estimates. The different turbulence models are also compared with each other on the basis of pressure coefficient distributions and velocity fluctuations along various lines and sections of the aircraft. For the mesh and the conditions presented in this study, the DDES Spalart–Allmaras model gives the best overall results.

Mathematical Subject Classification: 76G25, 76M12, 76F60, 76F55
Keywords: Jetstream 31, URANS, DES, DDES, Transient Computational Fluid Dynamics

1. Introduction

For advanced unsteady turbulence modeling, computational science and high performance computing have now become indispensable. Although Computational Fluid Dynamics (CFD) and Finite Element Analysis (FEA) cannot fully replace the experimental testing, it can undoubtedly expedite and complement the experimental results if done with the proper knowledge. Due to the advancements in the performance of the Graphics Processing Unit (GPU) and Central Processing Unit (CPU) performances, it is now possible to perform the transient simulations on a full-scale model of an aircraft using the turbulence technique of Detached Eddy Simulation (DES) and Delayed Detached Eddy Simulation (DDES) in a relatively short time. In

this study, the results from Unsteady Reynolds-Averaged Navier Stokes (URANS), DES and DDES simulations over Jetstream 31 aircraft are compared with the flight test data and wind tunnel results.

Parker [1] developed a Computer-Aided Design (CAD) model of the Jetstream 31 aircraft by scanning a tenth scaled 3D model, which was used to perform experimental tests in the wind tunnel. In 2008, Leung [2] used this geometry to perform a CFD simulation around the aircraft baggage pod to perform a structural analysis and obtain aerodynamic loads. However, it was not until 2012 that the whole Jetstream 31 aircraft was simulated by Vessot [3] without taking into account the propeller effects. The relative difference was 15-20% between simulation results and flight test data provided by the National Flying Laboratory Centre (NFLC) at Cranfield University, but the study could not predict the maximum lift coefficient CC_{Lmax} correctly. Simultaneously, Hodara [4] developed a User-Defined Function (UDF) for simulating the propeller of a half Dornier-228-101 aircraft model using an actuator disk based on the general momentum theory. Then, in 2013, Le Pajolec [5] took advantage of the previous studies to introduce the propeller effects into the full Jetstream 31 aircraft simulation. Le Pajolec [5] used the blade element momentum theory for the propellers and obtained less accurate results than the previous studies had. The results showed an improvement in the lift coefficient values but lower agreement in the drag coefficient. The following year, Jacques [6] and Lawson et al. [7] studied four configurations of the aircraft: without a propeller, with two engines, and without the left and right propeller. A hybrid mesh convergence was studied, and the lift coefficient C_L and drag coefficient C_D were predicted within a 5-16% of error with respect to the flight test data. In addition, the propeller-wing interference was analyzed by plotting spanwise and chordwise pressure distributions. In 2016, Fayyad [8] studied seven flight conditions including the propeller effects with the general momentum theory. The study analyzed drag, lift, slipstream velocity, velocity jump and propeller efficiency. Moreover, a preliminary study was carried out on Multiple Rotating Frames (MRF) and Sliding Mesh Models (SMM) with two types of meshes. In the same year, Zhu [9] used a feathered propeller designed in CATIA software and simulated in ANSYS-FLUENT R19.1 to compare the results with the general momentum theory. Finally, in 2017, Casadei et al. [10] focused on the analysis of the Jetstream 31 without one engine. Different angles of attack and sideslip were studied using a steady-state RANS and transient DES Realizable $k-\epsilon$ model with an unstructured mesh with 6 million elements. A grid convergence study was performed and the relative difference was between 2-16%. Furthermore, lift, drag and moment coefficients with different control surfaces were compared.

In most previous studies, the CFD of the full Jetstream 31 aircraft was based on steady-state RANS simulations and in one study simulations were performed with DES Realizable $k-\epsilon$. This study performs transient simulations of the Jetstream 31 aircraft using URANS, DES, and DDES modeling approaches on an unstructured grid and compares the performance of each technique with fight data, wind tunnel tests and theoretical estimates.

2. Methodology

2.1. **Governing equations.** In the present work, the numerical investigations on the Jetstream 31 aircraft are performed using ANSYS-FLUENT R19.1. The governing equations as used in ANSYS-FLUENT R19.1 for unsteady, viscous and compressible flow are provided in equations (2.1 to 2.3). In URANS simulations, the standard $k-\epsilon$ [11], Realizable $k-\epsilon$ [12], Renormalization Group (RNG) $k-\epsilon$ [13], and Shear Stress Transport (SST) $k-\omega$ [14] models are used for the turbulence closure. Another turbulence modeling approach used in this study is Detached Eddy Simulation (DES), where the URANS approach is used in the boundary layer and Large-Eddy Simulation (LES) is used after massive separation within a single formulation. An essential requirement for DES is that the grid space should be of LES quality, otherwise, it will produce results mixing URANS and LES components. A problem arises while using DES for meshes with high aspect ratios in the boundary layer, as this generates grid-induced separation due to an activation of the DES limiter in the URANS region. To overcome this, Delayed DES (DDES) approach is used, which preserves the RANS model throughout the boundary layer. The main idea of DDES is to include the molecular and turbulent viscosity information into the switching mechanism to delay this switching in boundary layers. In the present work, the DES with Spalart–Allmaras as proposed by Shur et al. [15] and DES with standard $k-\epsilon$ are also used for the turbulence closure. The mass, momentum and energy conservation equations can be written as follows:

$$\frac{\partial \rho}{\partial t} + \nabla \cdot (\rho \mathbf{u}) = 0, \tag{2.1}$$

$$\frac{\partial (\rho \mathbf{u})}{\partial t} + \nabla \cdot (\rho \mathbf{u} \otimes \mathbf{u}) = \rho \mathbf{g} - \nabla p + \nabla \cdot \underline{\underline{\tau}}, \tag{2.2}$$

$$\frac{\partial E}{\partial t} + \nabla \cdot [(E+p)\mathbf{u}] = -\nabla \cdot \mathbf{q} + \nabla \cdot (\mathbf{u} \cdot \underline{\underline{\tau}}), \tag{2.3}$$

where t is the time, ρ is density of the fluid, $\mathbf{u}$ is the velocity vector, $\mathbf{g}$ is the gravity vector, p is the pressure field, $\underline{\underline{\tau}}$ is viscous stress tensor, E is the total energy and $\vec{q}$ is the heat flux vector, respectively.

2.2. **Geometry.** The CAD model of the Jetstream 31 aircraft was developed by Parker [1], using a 3D non-contact scanning process. It is generated using a scanned version of the Cranfield Jetstream 31 tenth-scaled wind tunnel model. The geometrical differences between the actual aircraft and the model are highlighted in Table 1.

These minor differences in geometry will contribute to the differences in actual flight test data and the CFD results. Therefore, to have a more accurate comparison, the results from the wind tunnel and theoretical prediction of Cooke [16] will be considered. The theoretical predictions are performed using the airfoil section of the Jetstream 31 aircraft, which is similar to NACA 63A412. The drag polar and the lift curve slope results of flight test data, wind tunnel and theoretical predictions are provided in Table 2, where the angle of attack is in degrees.

Table 1. Geometrical differences between actual aircraft and CAD model

Aircraft section	**CAD model**	**Aircraft**
Aircraft length	14.31 m	14.36 m
Wing span	15.83 m	15.85 m
Wing tip chord	0.830 m	0.790 m
Wing surface	25.60 m^2	25.08 m^2
Aspect ratio	9.79	10.0
Tail span	6.61 m	6.60 m
Tail tip chord	0.653 m	0.686 m
Fin tip chord	0.844 m	0.889 m

Table 2. Lift curve slope and drag polar from various techniques

	Lift Curve Slope	**Drag Polar**
Flight test data	$C_L = 0.1031\alpha + 0.3393$	$C_D = 0.0587C_L^2 + 0.0374$
Wind tunnel results	$C_L = 0.0939\alpha + 0.1601$	$C_D = 0.0543C_L^2 + 0.0287$
Theoretical estimates [16]	$C_L = 0.0980\alpha + 0.2622$	$C_D = 0.0927C_L^2 + 0.0305$

Table 3. Extracted section locations on CAD model

Section number	**Dimensionless location**	**Dimensional location**
Section 1	±0.18	±1.695 m
Section 2	±0.29	±2.730 m
Section 3	±0.38	±3.578 m
Section 4	±0.64	±6.025 m
Section 5	±0.80	±7.532 m
Section 6	±0.99	±9.321 m

Furthermore, the different turbulence modeling techniques are compared on the basis of pressure coefficient distributions at the different sections mentioned in Table 3 and represented in Figure 1. The root-mean-square (RMS) fluctuating velocity profiles of different techniques are also compared at different lines represented in Figure 1. *Line 1* provides the velocity fluctuations in the wake of the propeller, *Line 2* gives the velocity profile over the wing surface, *Line 3* provides the velocity fluctuations in the wing-tip vortex region, and *Line 4* provides the results on the horizontal stabilizer.

2.3. **Mesh.** In this work, the mesh used by Lawson et al. [7] and Casadei et al. [10] is used for the numerical investigations. The adopted mesh is an unstructured hybrid mesh that is generated by ICEM-CFD software. The outer domain consists of a cylinder with upstream and downstream surfaces placed at ten fuselage lengths and a radius of 5 fuselage lengths. These dimensions ensure that the boundary conditions so not interfere with the flow in the aircraft proximity as well as to be able to capture

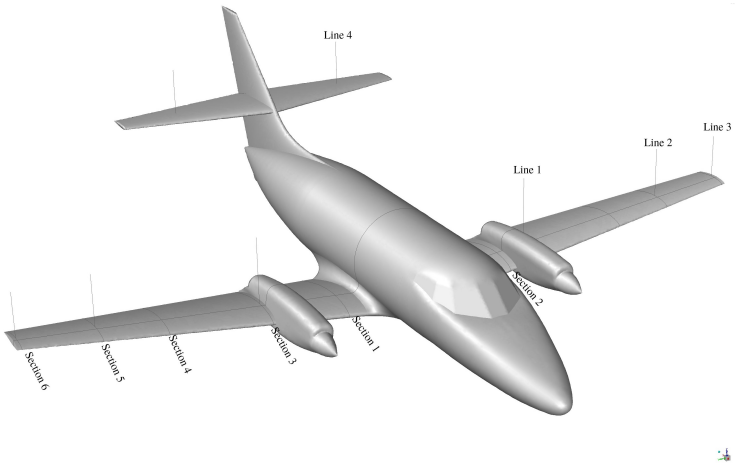

Figure 1. Location of each extracted surface on the Jetstream 31 aircraft

the wake. The front view and side view of the mesh is shown in Figures 2 and 3 respectively. The mesh has a y+ value of approximately 40 as a maximum limit and when extruding the prism layer, the growth ratio and number of layers have been chosen in order to have a total layer thickness equal to approximately 20% of the boundary layer thickness [7, 10]. The grid convergence study of this mesh has already been performed by Lawson et al. [7], and Casadei et al. [10].

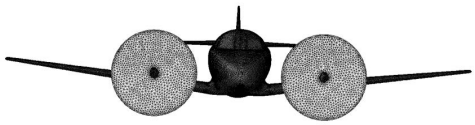

Figure 2. Mesh front view

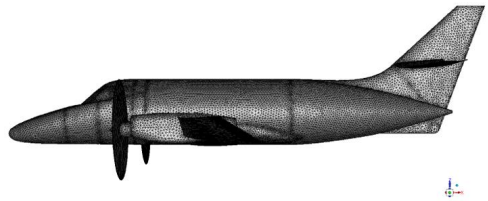

Figure 3. Mesh side view

2.4. **Solver settings.** The transient simulations are performed using an implicit formulation of a density based solver with the Roe-Flux Difference Splitting (Roe-FDS) Riemann solver. The spatial discretization is performed using the second-order Upwind scheme, and the gradients are calculated using the Green–Gauss node-based method. The time step size of $0.01s$ is used, and a factor of 0.25 is used for the higher-order term relaxation of the flow variables. The pseudo-transient and the wrapped face gradient corrections are not used for the simulations. Note that the discretization of the governing equations uses a first-order scheme and additional terms to employ higher than first-order approximations in the ANSYS-FLUENT environment. Therefore, the use of higher-order term relaxation is recommended for

transient flow simulations to accelerate convergence of the numerical solution [17]. Finally, the discretization of the turbulent kinetic energy and the specific dissipation rate is done using the QUICK scheme (Quadratic Upstream Interpolation for Convective Kinematics). The propellers are modeled through the use of User-Defined Functions (UDFs) in C programming language using the General Momentum Theory (GMT) [7, 10].

2.5. **Boundary conditions.** The boundaries of the computational domain are defined with the Robin boundary conditions with pressure farfield conditions. In this study, the air enters the inlet with the density of 0.99356 kg/m^3 at a Mach number of 0.3012 at an angle of 1.9^o. This Mach number is near the compressibility limit and results in a velocity of 99.93 m/s. The angle of attack is modeled by giving the x-component of velocity as 99.87 m/s and the z-component of velocity as 3.42 m/s. The temperature at the inlet is set to be 274.15 K, and the dynamic viscosity is 1.7894×10^{-5} $kg/(ms)$. These parameters result in the Reynolds number of 9.55×10^6. Where required, the turbulence intensity is set to be 2%, and the turbulent length scale is estimated as about one-fifth of the characteristic length scale, which comes out to be $0.344m$. The wall is defined to be made of aluminum as a stationary wall with a no-slip condition using a smooth wing surface in the ANSYS-FLUENT environment [17]. Aluminum has been used, because its properties are the closest to aircraft skin and the wind tunnel test model [7, 10].

3. Results and Discussions

The simulations are performed on Cranfield University's high-performance computer: CRESCENT, with ANSYS-FLUENT R19.1 using 64 CPU cores along with a GPU, which takes advantage of CUDA-enabled GPU using AmgX as its default linear solver. On an average it took up to 48 hours to complete one DES simulation and up to 40 hours for one URANS simulation.

3.1. **Coefficients of lift and drag.** Using the drag polar and lift curve slope from Table 2, the lift coefficient for the flight test data is 0.5352, the wind tunnel is 0.3385, and the theoretical estimate is 0.4484. Similarly, the drag coefficient for the flight test data is 0.0542, the wind tunnel is 0.0349, and the theoretical estimate is 0.0491. The lift coefficient obtained from various unsteady simulations is presented in Table 4 and the drag coefficient is presented in Table 5. The CFD results show significantly large relative differences when compared with the wind tunnel data. This is due to the fact that the model used in wind tunnel simulations did not have the propellers and was scaled to the tenth of the original aircraft. The scaling effect is the cause for high relative differences in C_D while not having propellers is the cause for high relative differences in C_L. These measuring errors are specific to the wind tunnel used and usually depend on its geometrical size. The differences between computational and wind tunnel data which are related to the scaling effects are classified in three parts: geometric model fidelity, pseudo-Reynolds effects and the fact that actual flight Reynolds number is generally difficult to achieve accurately. A detailed discussion of these effects are provided by Pettersson et al. [18].

Table 4. Relative differences in lift coefficient

Model	$\mathbf{C_L}$ **CFD**	$\mathbf{\Delta C_L}$ **w.r.t Flight test data**	$\mathbf{\Delta C_L}$ **w.r.t Wind tunnel**	$\mathbf{\Delta C_L}$ **w.r.t Theoretical**
URANS $k-\epsilon$	0.4338	-18.94%	+28.15%	-3.25%
URANS RNG $k-\epsilon$	0.4142	-22.61%	+22.36%	-7.63%
URANS Realizable $k-\epsilon$	0.4282	-19.98%	+26.49%	-4.51%
URANS SST $k-\omega$	0.4256	-20.47%	+25.73%	-5.08%
DDES Spalart–Allmaras	0.4433	-17.17%	+30.96%	-1.14%
DDES $k-\epsilon$	0.4141	-22.62%	+22.33%	-7.69%
DES $k-\epsilon$	0.4088	-23.62%	+20.76%	-8.83%

Table 5. Relative differences in drag coefficient

Model	$\mathbf{C_D}$ **CFD**	$\mathbf{\Delta C_D}$ **w.r.t Flight test data**	$\mathbf{\Delta C_D}$ **w.r.t Wind tunnel**	$\mathbf{\Delta C_D}$ **w.r.t Theoretical**
URANS $k-\epsilon$	0.0532	-1.84%	+52.44%	+8.35%
URANS RNG $k-\epsilon$	0.0415	-23.46%	+18.91%	-15.47%
URANS Realizable $k-\epsilon$	0.0475	-12.36%	+36.11%	-3.25%
URANS SST $k-\omega$	0.0418	-22.87%	+19.77%	-14.86%
DDES Spalart–Allmaras	0.0445	-17.89%	+27.51%	-9.37%
DDES $k-\epsilon$	0.0411	-24.17%	+17.76%	-16.29%
DES $k-\epsilon$	0.0409	-24.54%	+17.19%	-16.70%

The CFD results still show significant differences compared to flight test data, although now much less than the wind tunnel data. These relative differences can be attributed to the geometrical difference between the CAD model and the original aircraft. Moreover, in CFD analysis, the intake, cooling system and the exhaust of the propulsion system are not modelled. In the CFD analysis, the surface is a clean surface without any rivets or joints, which is not the case in the actual flight. Due to these factors, there are differences in the C_L and C_D values of CFD and flight test data. The relative differences in CFD results are minor when compared with the theoretical estimates of Cooke [16], with URANS Realizable $k-\epsilon$ model and DDES Spalart–Allmaras model showing the best predictions of C_L and C_D. The better performance of these models was expected for these coefficients, as these models are good in predicting flow conditions far from the boundary layer and thus had better lift and drag predictions. The results of DDES $k-\epsilon$ and DES $k-\epsilon$ could be improved with grid refinement in the region far from the boundary layer. In terms of mesh refinement in the region far from the boundary layer in the DES and DDES simulations, LES mode is activated in the region far from the boundary layer, where results can be improved by refining the grid spacing. Note that the grid refinement can improve the results in the RANS/LES transition region in general. In the cases of DDES $k-\epsilon$ and DES $k-\epsilon$ modelling approaches, the grid refinement may improve the performance of these models in the region far from the wall, because their model constants are tuned for capturing fluid flow physics in the near wall region. On the other hand,

the DDES Spalart–Allmaras model is an engineering turbulence model, which was specifically developed for aerospace applications. Its model constants are calibrated with the Spalart–Shur correction to achieve the best performance in the region far from the boundary layer. This can be the reason why the grid refinement is not necessary when the DDES Spalart–Allmaras turbulence modelling approach is used in the region far from the wall.

3.2. **Flow analysis.** Figure 4 represents the pathlines colored with Mach number contours for the simulation carried using the DDES Spalart–Allmaras model. Furthermore, Figure 5 represents the Q-criterion of the simulation at the final time step, which is very helpful in identifying regions of high vorticity. The numerical simulation is able to clearly capture the wing-tip vortices and the vortices created in the wake of the propeller. It is also evident that a nearly elliptical lift distribution exists over the wing. Moreover, at the current angle of attack, the flow over horizontal and vertical stabilizers is unhindered by the wake of the wing, thereby highlighting that complete aerodynamic control can be achieved by the elevator and rudder.

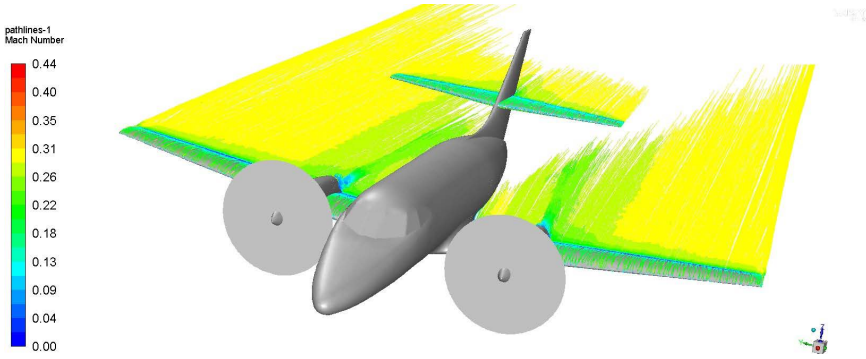

Figure 4. Pathlines coloured with Mach numbers for DDES Spalart–Allmaras model

3.3. **Pressure coefficient distribution.** Figures 6 to 11 represents the pressure coefficient distributions obtained from different turbulence models for the different sections. It is evident from the plots that the peak in $-C_P$ values decreases from wing-root to wing-tip. The difference in pressure between the lower and upper surfaces decreases from wing-root to wing-tip as well. These observations highlight that the lift distribution on the wing is nearly elliptical. All the turbulence models show similar values of the pressure coefficient with an exception near the trailing edge of the wing in *Sections 3* to *5*. It is important to note that an appropriate selection of the turbulence model and the mesh density plays a key role together, especially for hybrid turbulence modeling, because there are no general recipes about how to select them. A possible way is to make a reasonable assessment on both of them and perform grid refinement and parametric studies for the investigated physical problem. Casadei et al. [10] performed a systematic grid convergence study for the Jetstream

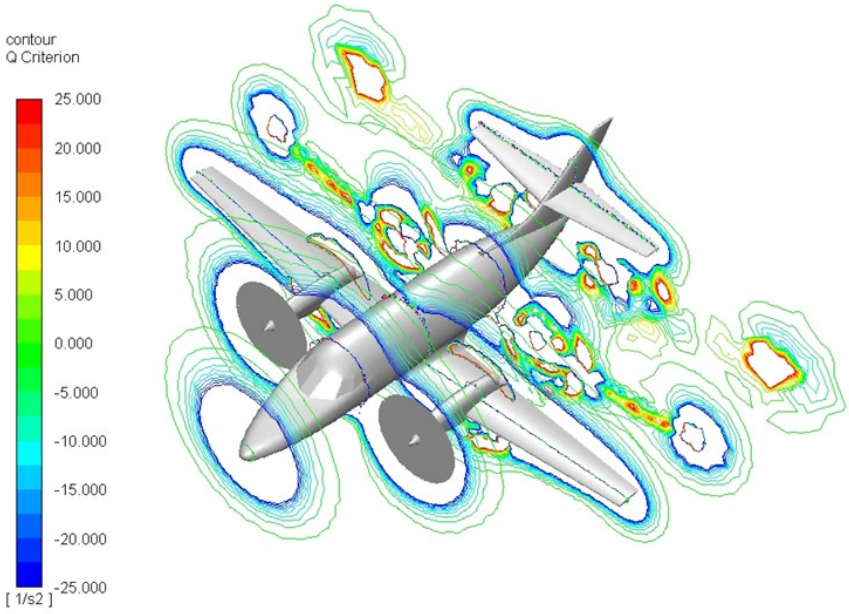

Figure 5. Q-criterion results for DDES Spalart–Allmaras model

31 aircraft which is used in this work and we performed additional simulations.

Since the URANS Realizable $k-\epsilon$ model and DDES Spalart–Allmaras gave the best C_L and C_D predictions, these will be used as a baseline for calculating the *L2 norm* of the difference. The *L2 norm* of the difference between URANS Realizable $k-\epsilon$ and DDES Spalart–Allmaras at *Section 1* is 3.23% and at *Section 6* is 1.82%. The *L2 norm* of the difference between URANS Realizable $k-\epsilon$ and DES $k-\epsilon$ at *Section 1* is 3.37% and at *Section 6* is 3.52%. The *L2 norm* of the difference between URANS Realizable $k-\epsilon$ and DDES $k-\epsilon$ at *Section 1* is 2.75% and at *Section 6* is 3.31%. Similarly, the *L2 norm* of the difference between DDES Spalart–Allmaras and URANS Realizable $k-\epsilon$ at *Section 1* is 1.91%. Evidently, there is not much difference between the C_P distributions of different turbulence models in *Section 1* and *Section 6*. However, the differences are more apparent near the trailing edge of the wing in *Section 2* to *Section 5*. As *Section 2* and *Section 3* lie in the wake of the propeller, some oscillations in the C_P values are clearly visible.

3.4. **Root-Mean-Square (RMS) velocity distribution.** The method of computing the Reynolds stress tensor for calculating the turbulent (eddy) viscosity is different for the different turbulence models, thus yielding different velocity fluctuations. Since the time average of these fluctuations is zero, an effective way to examine these is by

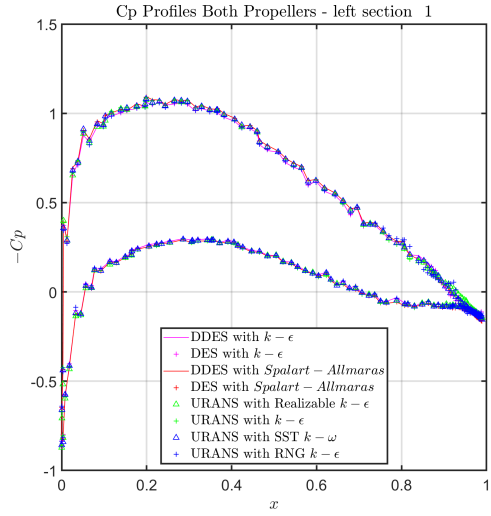

Figure 6. Comparison of pressure coefficients for *Section 1*

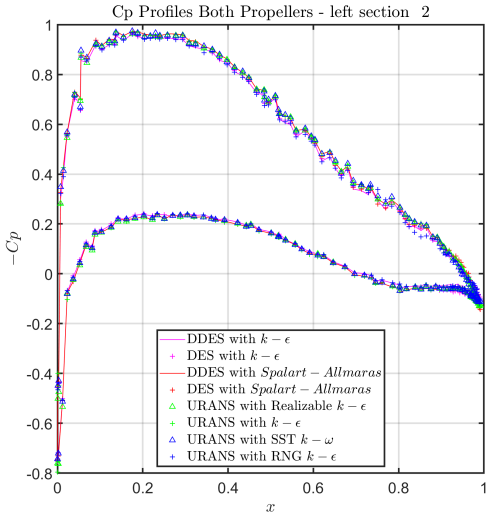

Figure 7. Comparison of pressure coefficients for *Section 2*

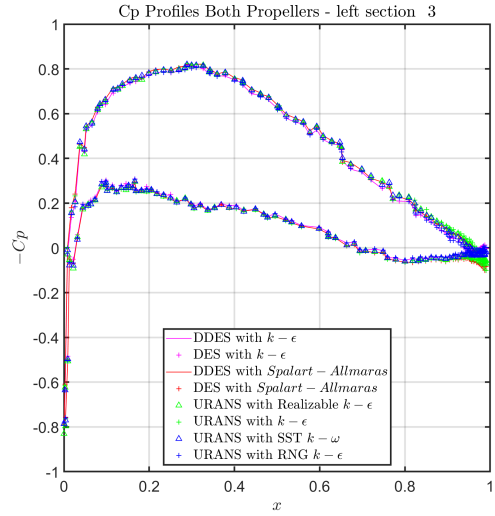

Figure 8. Comparison of pressure coefficients for *Section 3*

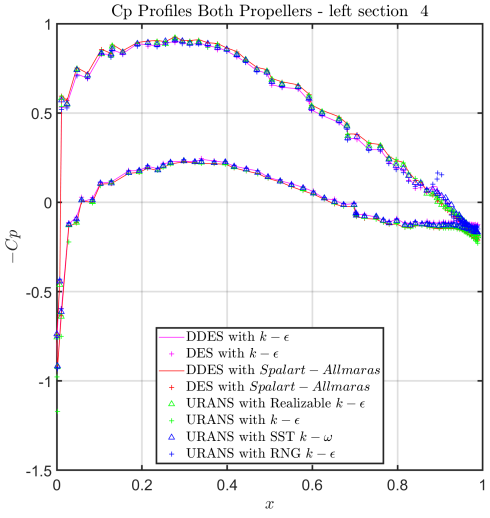

Figure 9. Comparison of pressure coefficients for *Section 4*

calculating the RMS of fluctuating velocities for the different turbulence models.

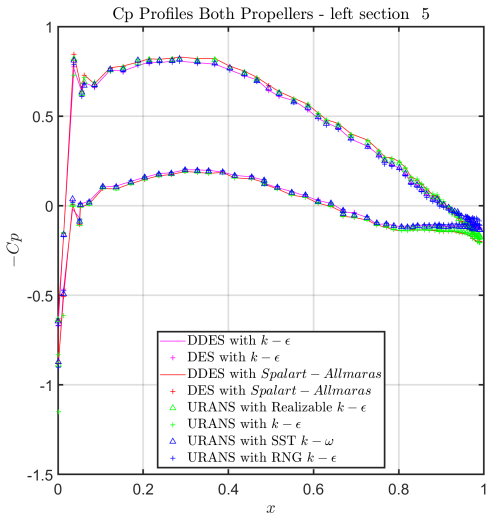

Figure 10. Comparison of pressure coefficients for *Section 5*

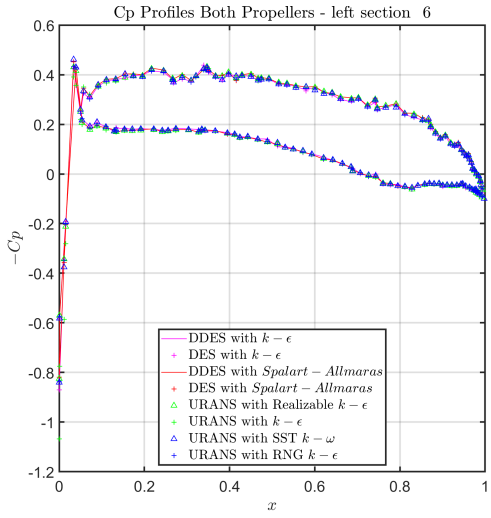

Figure 11. Comparison of pressure coefficients for *Section 6*

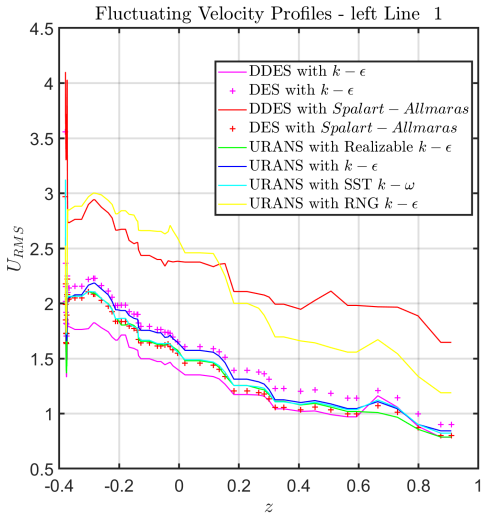

Figure 12. Comparison of RMS fluctuating velocity profile at *Line 1*

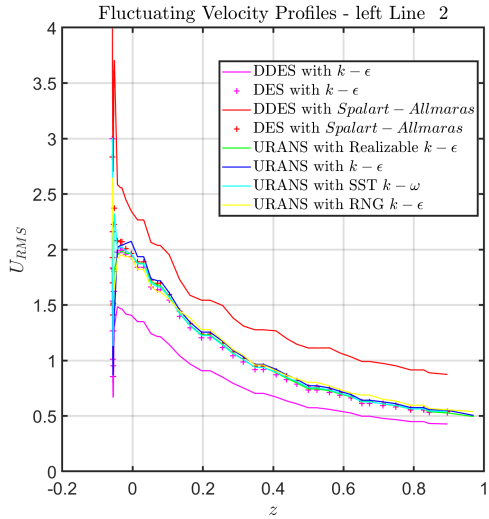

Figure 13. Comparison of RMS fluctuating velocity profile at *Line 2*

Figure 12 compares the fluctuating velocity profiles in the wake of the propeller (*Line 1*). As expected, each model captures the fluctuations differently. The URANS RNG $k-\epsilon$ model has the capability to capture rapidly strained flows and outperforms

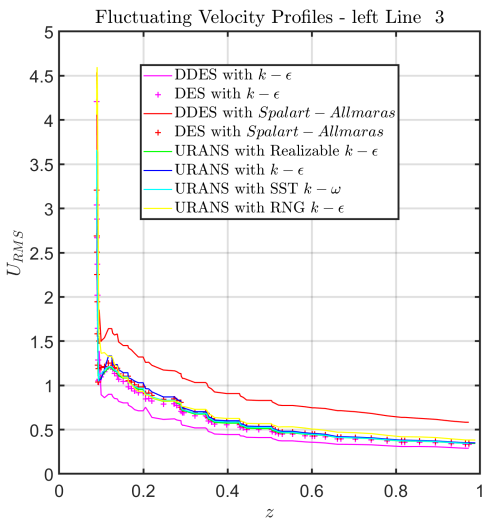

Figure 14. Comparison of RMS fluctuating velocity profile at *Line 3*

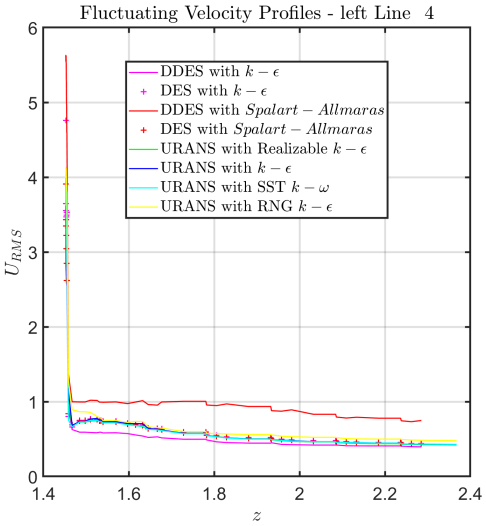

Figure 15. Comparison of RMS fluctuating velocity profile at *Line 4*

other models in the region as this region is greatly influenced by vortex formation. The DDES Spallart Allmaras model also captures high fluctuations, while the other models also fairly capture fluctuations with a similar pattern. The *L1* norm of the difference of the fluctuations between DDES Spallart Allmaras model and URANS RNG $k-\epsilon$ model is 14.06%. Figure 13 compares the fluctuating velocity profiles in the centre of the wing (*Line 2*). Due to the almost uniform flow, the DDES Spallart Allmaras model and URANS $k-\epsilon$ model are able to capture higher fluctuations than other models. Figure 14 compares the fluctuating velocity profiles at wing-tips (*Line 3*). Again, the DDES Spallart Allmaras model is able to capture higher fluctuations, while the URANS Realizable $k-\epsilon$ model gives the smaller value of the fluctuations. Figure 15 compares the fluctuating velocity profiles at the horizontal stabilizer of the Jetstream 31 aircraft (*Line 4*). The flow in this region is partially affected by the wake of the propeller and is unaffected by the wake of the wing. As a result, all the models capture the fluctuations in the same range.

4. Conclusions

This paper presented transient simulations of a full-scale Jetstream 31 aircraft using URANS, DES and DDES turbulence modeling approaches. It was found that the lift and drag coefficients obtained from CFD are much closer to the theoretical estimates of Cooke [16] than the results of the flight test or wind tunnel data. The difference between CFD and wind tunnel results is attributed to the scaling effects and absence of a propeller in the wind tunnel model. On the other hand, the difference between CFD results and flight test data are attributed to the minor geometrical difference between

the CAD model and original aircraft, and the absence of modeling of various elements of the propulsion system. Therefore, in order to reduce the error between CFD results and flight test data, the simulation setup should include effects like surface roughness, intake and exhaust of propulsion system and so on. The inclusion of these models will increase computational time, but this will be offset by advancements in computing. These results highlight that although there are some differences between CFD results and flight test data, the detailed flow characteristics obtained from CFD certainly help in optimizing the design and reducing the overall development cost of any new design project.

For the mesh and the conditions presented in this study, the DDES Spalart–Allmaras model gives the best overall results with the highest accuracy of lift coefficient, the relatively good performance in the drag coefficient, and consistently capturing the fluctuations in the velocity. The results from the DDES $k-\epsilon$ model and DES $k-\epsilon$ model were not that satisfactory. However, the results from these models will surely be improved by refining the mesh in the region far from the boundary layer. Finally, all turbulence approaches used in this study provided almost the same pressure coefficient distribution with a slight exception near the trailing edge of the wing.

Acknowledgements. This research work was financially supported by the Centre for Computational Engineering Sciences at Cranfield University under project code EEB6001R. We would like to express a special thanks to Professor Nicholas Lawson, former Head of the National Flying Laboratory Centre (NFLC) at Cranfield University, for providing the flight test data. Furthermore, we would like to acknowledge the IT support for using the High Performance Computing (HPC) facilities at Cranfield University, UK.

References

1. R. Parker. "Investigation and development of a 3D non-contact scanning process for CFD model generation." Ph. D. Dissertation. Cranfield University, 2006.
2. C.W.E. Leung. "CFD Modelling of the fluid flow around a BAE Systems Jetstream 31 Equipment Pod." M. Sc. Dissertation. Cranfield University, 2008.
3. C. Vessot. "CFD Aerodynamic Model of the Jetstream 31." M. Sc. Dissertation. Cranfield University, 2012.
4. J. Hodara. "Computational 3D modelling of propeller effects on the boundary layer of a Dornier Fo-228." M. Sc. Dissertation. Cranfield University, 2012.
5. M.L. Pajolec. "Investigation of propeller theories on BAE Jetstream 31 CFD model." M. Sc. Dissertation. Cranfield University, 2013.
6. H. Jacques. "Simulation of propeller effects on the Jetstream 31 Aircraft." M. Sc. Dissertation. Cranfield University, 2014.
7. N.J. Lawson, H. Jacques, J.E. Gautrey, A.K. Cooke, J.C. Holt, and K.P. Garry. "Jetstream 31 national flying laboratory: Lift and drag measurement and modelling." *Aerospace Science and Technology,* **60**, (2017), pp. 84–95. DOI: 10.1016/j.ast.2016.11.001.
8. K.A.A. Fayyad. "CFD Analysis of propeller effects on Jetstream 31." M. Sc. Dissertation. Cranfield University, 2016.

9. Y. Zhu. "Simulation of feathered propeller on the Jetstream 31 Aircraft." M. Sc. Dissertation. Cranfield University, 2016.
10. L. Casadei, L. Könözsy, and N. J. Lawson. "Unsteady Detached-Eddy Simulation (DES) of the Jetstream 31 aircraft in One Engine Inoperative (OEI) condition with propeller modelling." *Aerospace Science and Technology,* **91**, (2019), pp. 287–300. DOI: 10.1016/j.ast.2019.05.034.
11. B. E. Launder and D. B. Spalding. "The numerical computation of turbulent flows." *Journal of Scientific Computing,* **3**, (1974), pp. 269–289. DOI: 10.1016/0045-7825(74)90029-2.
12. T.H. Shih, W.W. Liou, A. Shabbir, Z. Yang, and J. Zhu. "Two-equation eddy-viscosity turbulence models for engineering applications." *Computer and Fluids* **24**(3), (1995), pp. 227–238. DOI: 10.1016/0045-7930(94)00032-T.
13. V. Yakhot and S.A. Orszag. "Renormalization group analysis of turbulence." *Journal of Scientific Computing* **1**(1), (1986), pp. 1–51. DOI: 10.1007/BF01061452.
14. F. R. Menter. "Two-equation eddy-viscosity turbulence models for engineering applications." *AIAA Journal,* **32**(8), (1994), pp. 1598–1605. DOI: 10.2514/3.12149.
15. M.L. Shur, M.K. Strelets, A.K. Travin, and P.R. Spalart. "Turbulence Modeling in Rotating and Curved Channels: Assessing the Spalart-Shur Correction." *AIAA Journal* **38**(5), (2000), pp. 784–792. DOI: 10.2514/2.1058.
16. A. K. Cooke. "Simulation model of the NFLC Jetstream 31." Report. Cranfield University, 2006.
17. Ansys. "Fluent 19.1 user's guide." Help system. ANSYS, Inc., 2019.
18. K. Pettersson and A. Rizzi. "Aerodynamic scaling to free flight conditions: Past and present." *Progress in Aerospace Sciences,* **44**(4), (2008), pp. 295–313. DOI: 10.1016/j.paerosci.2008.03.002.

Notes for Contributors
to the Journal of Computational and Applied Mechanics

Aims and scope. The aim of the journal is to publish research papers on theoretical and applied mechanics. Special emphasis is given to articles on computational mechanics, continuum mechanics (mechanics of solid bodies, fluid mechanics, heat and mass transfer) and dynamics. Review papers on a research field and materials effective for teaching can also be accepted and are published as review papers or classroom notes. Papers devoted to mathematical problems relevant to mechanics will also be considered.
Frequency of the journal. Two issues a year (approximately 80 pages per issue).

Submission of Manuscripts. Submission of a manuscript implies that the paper has not been published, nor is being considered for publication elsewhere. Papers should be written in standard grammatical English. The manuscript is to be submitted in electronic, preferably in pdf, format. The text is to be 130 mm wide and 190 mm long and the main text should be typeset in 10pt CMR fonts. Though the length of a paper is not prescribed, authors are encouraged to write concisely. However, short communications or discussions on papers published in the journal must not be longer than 2 pages. Each manuscript should be provided with an English Abstract of about 50–70 words, reporting concisely on the objective and results of the paper. The Abstract is followed by the Mathematical Subject Classification – in case the author (or authors) give the classification codes – then the keywords (no more than five). References should be grouped at the end of the paper in numerical order of appearance. Author's name(s) and initials, paper titles, journal name, volume, issue, year and page numbers should be given for all journals referenced.
The journal prefers the submission of manuscripts in LaTeX. Authors should select the $\mathcal{AMS}$-LaTeX article class and are not recommended to define their own LaTeX commands. Visit our home page for further details concerning how to edit your paper.
Manuscripts should be sent to either to the Editorial Office of JCAM:

jcam@uni-miskolc.hu

or directly to an editor: László Baranyi

laszlo.baranyi@uni-miskolc.hu (fluid mechanics and heat transfer)

or BalázsTóth

balazs.toth@uni-miskolc.hu (solid mechanics).

The eventual supply of an accepted for publication paper in its final camera-ready form will ensure more rapid publication. Format requirements are provided by the home page of the journal from which sample LaTeX files can be downloaded:

`http://www.mech.uni-miskolc.hu/jcam/`

These sample files can also be obtained directly (via e-mail) from Balázs Tóth.

One issue of the journal will be provided free of charge and mailed to the correspondent author. Since JCAM is an open access journal each paper can be downloaded freely from the homepage of the journal.

The Journal of Computational and Applied Mechanics is abstracted in Zentralblatt für Mathematik and in the Russian Referativnij Zhurnal.

Secretariat of the Vice-Rector for Research and International Relations, University of Miskolc
Responsible for publication: Prof. Dr. Zita Horváth, rector
Published by the Miskolc University Press under the leadership of Attila Szendi
Responsible for duplication: Works manager Erzsébet Pásztor
Number of copies printed: 75
Put to the Press on December 6, 2021
Number of permission: MERT.2021-243.ME.
ISSN 2732–0189 (Online)
ISSN 1586–2070 (Print)

A Short History of the Publications of the University of Miskolc

The University of Miskolc (Hungary) is an important center of research in Central Europe. Its parent university was founded by the Empress Maria Teresia in Selmecbánya (today Banska Štiavnica, Slovakia) in 1735. After the first World War the legal predecessor of the University of Miskolc moved to Sopron (Hungary) where, in 1929, it started the series of university publications with the title *Publications of the Mining and Metallurgical Division of the Hungarian Academy of Mining and Forestry Engineering* (Volumes I.-VI.). From 1934 to 1947 the Institution had the name Faculty of Mining, Metallurgical and Forestry Engineering of the József Nádor University of Technology and Economic Sciences at Sopron. Accordingly, the publications were given the title *Publications of the Mining and Metallurgical Engineering Division* (Volumes VII.-XVI.). For the last volume before 1950 – due to a further change in the name of the Institution – *Technical University, Faculties of Mining, Metallurgical and Forestry Engineering, Publications of the Mining and Metallurgical Divisions* was the title.

For some years after 1950 the Publications were temporarily suspended.

After the foundation of the Mechanical Engineering Faculty in Miskolc in 1949 and the movement of the Sopron Mining and Metallurgical Faculties to Miskolc, the Publications restarted with the general title *Publications of the Technical University of Heavy Industry* in 1955. Four new series - Series A (Mining), Series B (Metallurgy), Series C (Machinery) and Series D (Natural Sciences) - were founded in 1976. These came out both in foreign languages (English, German and Russian) and in Hungarian. In 1990, right after the foundation of some new faculties, the university was renamed to University of Miskolc. At the same time the structure of the Publications was reorganized so that it could follow the faculty structure. Accordingly three new series were established: Series E (Legal Sciences), Series F (Economic Sciences) and Series G (Humanities and Social Sciences). The latest series, i.e., the series H (European Integration Studies) was founded in 2001. The eight series are formed by some periodicals and such publications which come out with various frequencies.

Papers on computational and applied mechanics were published in the

Publications of the University of Miskolc, Series D, Natural Sciences.

This series was given the name Natural Sciences, Mathematics in 1995. The name change reflects the fact that most of the papers published in the journal are of mathematical nature though papers on mechanics also come out.

The series

Publications of the University of Miskolc, Series C, Fundamental Engineering Sciences

founded in 1995 also published papers on mechanical issues. The present journal, which is published with the support of the Faculty of Mechanical Engineering and Informatics as a member of the Series C (Machinery), is the legal successor of the above journal.

Journal of Computational and Applied Mechanics

Volume 16, Number 2 (2021)

Contents

Contributed Papers